



## Close-range, ground-based hyperspectral imaging for mining applications at various scales: Review and case studies

Diana Krupnik\*, Shuhab Khan

Department of Earth and Atmospheric Sciences, University of Houston, USA



### ARTICLE INFO

**Keywords:**

Ground-based hyperspectral imaging  
Imaging spectroscopy  
Mineral mapping  
Mineral exploration  
Gold deposits  
Copper porphyry  
Bituminous limestone

### ABSTRACT

Detailed mapping of mineral phases at centimeter scale can be useful for geological investigation, including resource exploration. This work reviews case histories of ground-based close-range hyperspectral imaging for mining applications. Studies of various economic deposits are discussed, as well as techniques used for data correction, integration with other datasets, and validation of spectral mapping results using geochemical techniques. Machine learning algorithms suggested for automation of the mining workflow are reviewed, as well as systems for environmental monitoring such as gas leak detection. Three new case studies that use a ground-based hyperspectral scanning system with sensors collecting data in the Visible Near-Infrared and Short-Wave Infrared portions of the electromagnetic spectrum in active and abandoned mines are presented. Vertical exposures in a Carlin Style sediment-hosted gold deposit, an active Cu-Au-Mo mine, and an active asphalt quarry are studied to produce images that delineate the extent of alteration minerals at centimeter scale to demonstrate an efficient method of outcrop characterization, which increases understanding of petrogenesis for mining applications. In the Carlin-style gold deposit, clay, iron oxide, carbonate, and jarosite minerals were mapped. In the copper porphyry deposit, different phases of alteration are delineated, some of which correspond to greater occurrence of ore deposits. A limestone quarry was also imaged, which contains bitumen deposits used for road paving aggregate. Review of current literature suggests use of this technology for automation of mining activities, thus reducing physical risk for workers in evaluating vertical mine faces.

### List of abbreviations

CL	Cathodoluminescence
CR	Continuum removal
EL	Empirical line
EMPA	Electron microprobe analyses
GP	Gaussian processes
HSI	Hyperspectral imaging
ICP-AES	Inductively-coupled plasma-atomic emission spectroscopy
ICP-MS	Inductively coupled plasma mass spectrometry
ICP-OES	Inductively coupled plasma optical emission spectroscopy
LiDAR	Light detection and ranging
LWIR	Long-wave infrared
MNF	Minimum noise fraction
MTGP	Multi-task Gaussian processes
MTMF	Mixture tuned matched filtering
NIR	Near-infrared
OAD	Observation angle dependent
PCA	Principal Component Analysis
PTFE	Polytetrafluoroethylene
REE	Rare earth element
SAM	Spectral angle mapper
SE	Squared exponential

SFF	Spectral feature fitting
SFF	Spectral feature fitting
SM	Structure from motion
SIFT	Scale invariant feature transform
SVM	Support vector machine
SWIR	Short-wave infrared
TIR	Thermal infrared
TOC	Total organic carbon
VNIR	Visible near-infrared
XRD	X-ray diffraction

### 1. Introduction

Methods of terrestrial imaging spectroscopy, both field-based and laboratory-based, have been used for various geoscience applications, including analysis of hydrocarbon reservoir analogues (Okyay et al., 2016; Snyder et al., 2016; Sun et al., 2018a; Sun et al., 2017), mineral exploration (Bedini, 2011; Dalm et al., 2017; Sun et al., 2019; Sun et al., 2015; van der Meer et al., 2018), analysis of sedimentology and diagenesis (Alonso de Linaje and Khan, 2017; Alonso De Linaje et al., 2018; Greenberger et al., 2016; Manß et al., 2017; Murphy et al., 2016; Okyay

\* Corresponding author.

E-mail address: [dkrupnik@uh.edu](mailto:dkrupnik@uh.edu) (D. Krupnik).

and Khan, 2016), soil science (Askari et al., 2013; O'Rourke and Holden, 2012; Steffens et al., 2014), and gas detection (Zheng et al., 2014). Additionally, it has been used for medical applications (Calin et al., 2013; Li et al., 2013; Lu and Fei, 2014), food quality measurements (Achata et al., 2019; Dubois et al., 2005; Li et al., 2018; Ma et al., 2019; Mishra et al., 2019; Shi et al., 2019), and many others (Chaudhary et al., 2018; Edelman et al., 2012; Ferreira et al., 2017; Gevaux et al., 2018; Payne et al., 2005). Traditional methods of hyperspectral imaging operate from an airborne or satellite platform and are effective for large-scale regional mapping in plan view. However, these methods are not effective for studying vertical outcrops. Large-scale, long-range hyperspectral mapping was conducted using helicopter- and ship-based platforms at relatively close range compared to traditional techniques (Rosa et al., 2017; Salehi et al., 2018). Ground-based hyperspectral imaging of outcrops can bridge this gap, providing mineralogical maps at centimeter to millimeter scale.

As part of a traditional mineral exploration workflow, drill cores are collected, and geochemical analyses are carried out for discrete samples, sometimes with large sampling intervals (Atapour and Aftabi, 2007). Examples include atomic absorption spectrometry, inductively coupled plasma mass spectrometry (ICP-MS), neutron activation analysis, and others (Hall and Bonham-Carter, 1988). Non-imaging reflectance spectroscopy has been carried out for mining applications (Arne et al., 2016; Crowley et al., 2003; Schodlok et al., 2016; van Ruitenbeek et al., 2005; Wang et al., 2017b) and soil studies (Calderón et al., 2011; Eisele et al., 2015; Sun et al., 2018b; Wang et al., 2017). Although these methods are precise in their capability to identify concentrations of ore, they can be augmented by continuous mineral maps that would provide information where point data are missing.

Imaging spectroscopy, also referred to as hyperspectral sensing, has grown rapidly over the last three decades (Goetz, 2009; Gupta, 2018). This entails acquisition of images in hundreds of continuous spectral bands, allowing for the construction of a spectral curve for each image pixel (Fig. 1). Spectral absorptions of materials make it possible to identify them based on their spectral response, which is typically a result of various atomic-molecular processes. Absorption features within visible and near-infrared (VNIR) wavelengths ( $\sim 400\text{--}1000\text{ nm}$ ) can be a result of electronic processes, crystal field effects, charge transfer, and conduction bands. Iron oxides and hydroxides such as hematite and goethite, respectively, have distinct absorption features in the VNIR wavelengths (Singer, 1981). Due to crystal field transition, goethite has asymmetrical absorptions at 480 and 670 nm. Hematite has an absorption at about 550 nm due to charge transfer, and a weaker crystal absorption near 670 nm (Crowley et al., 2003).

In short-wave infrared (SWIR) wavelengths (1,000–2,500 nm), these are caused by vibrational processes of certain molecular bonds. When a molecule shows a dipole moment, it is said to be SWIR-active (vibrations occur at a specific frequency that allows its identification). Examples include water ( $\sim 1,400$  and  $1,900\text{ nm}$ ), combinations of metal-OH bend plus OH stretch (2,200 to 2,300 nm), and other OH bearing minerals (2,700–2,800 nm); carbonate overtones (2,300–2,350 and 2,500–2,550 nm with weaker bands near 2,120–2,160 nm, 1,970–2,000 nm, and 1,850–1,870 nm), and others as shown in Fig. 2 and Table 1 (Clark, 1999).

This work seeks to review case histories and publication trends (Fig. 3) in close-range hyperspectral imaging (HSI), specifically where it is applied to the field of geoscience for mineral exploration. Close-range HSI is significant, due to the high spatial resolution and low signal to noise ratio that can be achieved. Also, three original case studies are presented, which display the use of ground-based HSI of vertical outcrops in mines and quarries within different geological settings and economic deposit types, including a historically-developed Carlin-style gold deposit, an actively-mined copper-molybdenum-gold porphyry deposit, and an active asphalt quarry (Fig. 4).

## 2. Review of close-range imaging spectroscopy for earth science

This section reviews published case histories that apply HSI to geoscience studies, specifically in mine and quarry settings. Mines and quarries are optimal for outdoor scanning, because the relatively fresh rock faces produced by recent excavations are not strongly affected by surface weathering processes. Investigations that were conducted in field and laboratory settings, and combinations of field and laboratory imaging studies are discussed. Various applications are presented, including several types of economic deposits, soil studies, and gas detection. Publications that include terrestrial HSI for geoscience applications have increased significantly since 2001 (Fig. 3). Although the list of publications is not exhaustive, examples are included from most research groups that own or have access to hyperspectral sensors.

### 2.1. HSI correction and integration with topographic data

Correction of ground-based hyperspectral imagery typically involves transferring raw data to reflectance. Raw digital numbers are first converted to radiance by either using calibration coefficients provided by the manufacturer (Kurz et al., 2011; Sima et al., 2014), using radiometric calibration by experimental characterization of gain and offset (Chamberland et al., 2005), or using dark subtraction (Kruse et al., 2012; Murphy et al., 2012). Atmospheric effects are removed using empirical line (EL) calibration (Smith and Milton, 1999), and in a new application by dividing each pixel spectrum by an atmospheric correction spectrum, which is derived directly from the scene by finding the maximum absorption depth of water vapor, located at 1126 nm (Lorenz et al., 2018b; Rosa et al., 2017).

Early studies that employed integration of hyperspectral data with digital topography, specifically terrestrial LiDAR-derived 3D models, were focused on correction of geometric distortions for accurate geologic measurements, such as delineation of surface area of different facies (Buckley et al., 2012; Kurz et al., 2008; Kurz et al., 2009; Kurz et al., 2011). Also, geological interpretation is enhanced with the availability of 3D data (Krupnik et al., 2016; Snyder et al., 2016; Sun et al., 2017). Integration with 3D data is done using various algorithms, but each requires identification of control points, either automatically using the scale invariant feature transform (SIFT) (Monteiro et al., 2013), or by selecting points manually (Kurz et al., 2013). A less costly alternative to LiDAR-derived DEMs is presented by Salehi et al. (2018), where RGB imagery collected using a handheld camera were used to extract topographic data using Structure from Motion (SfM); these data were registered to HSI-derived classification products and single band minimum wavelength images.

To address the limitation of suboptimal illumination conditions during data acquisition, Boesche et al. (2015) used multi-temporal averaging, i.e. calculating a weighted mean of multiple images using a normalized weighting factor according to spectral homogeneity. Reference panels with known reflectance were used for determining spectral homogeneity, which was computed by calculating the standard deviations of pixel spectra at the panel locations. Corrected imagery was used to map neodymium enrichment in carbonatite rocks.

Shadow restoration was done by applying algorithms using both passive (hyperspectral) and active (LiDAR) reflectance spectra. Indirect shadow restoration utilizes a scale factor that is computed from an approximate difference between a common material under shadow and direct sunlight. Direct shadow restoration used a scale factor computed from a ratio of active (LiDAR) to passive (hyperspectral) reflectance at the active wavelength (1550 nm in this example) (Hartzell et al., 2017). Topographic correction was applied by Lorenz et al. (2018b) by computing sun incidence angles and point normals from photogrammetric data acquired using SfM. Hyperspectral imagery collected at 2 open pit mines was registered to SfM-generated point clouds to produce geometrically accurate, spatially referenced “hyperclouds” that were used to generate detailed mineralogical maps. The same atmospheric and

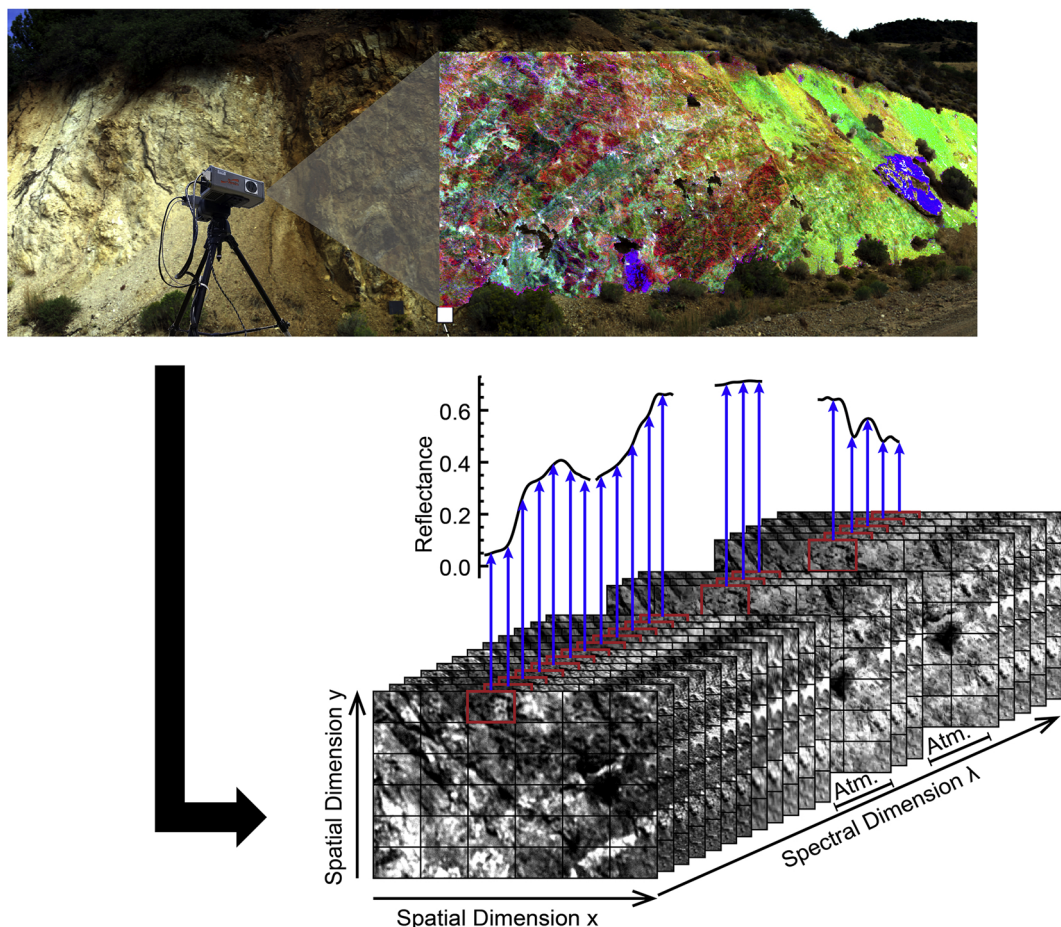


**Fig. 1.** Illustration of hyperspectral image cube from a ground-based scan. Atmospheric absorption bands are denoted as ‘Atm’ and span 1300–1500 and 1750–2000 nm ranges. The spectral dimension ranges from 400–2400 nm.

topographic correction techniques were applied by [Jackisch et al. \(2018\)](#) to monitor a lignite mining district for acid mine drainage using HSI aboard UAS ([Table 2](#)).

## 2.2. Improvements in safety

[McHugh et al. \(2001\)](#) conducted an outdoor HSI in the VNIR spectral range (450–1000 nm) to study outcrops, hand samples, and drill core, to test the feasibility of HSI for assessment of mine safety conditions. The goal of this study was to investigate rock types that contribute to slope failures in open mine settings, in which clay - rich rocks play a role, thus highlighting the need for a sensor with capability to image within SWIR wavelengths, where absorption features for clay identification are most prominent. [Fraser et al. \(2006\)](#) used a hyperspectral camera that operates in both VNIR and SWIR wavelengths to map ore-grade minerals in a base metal mine in New South Wales, Australia. Spectral imagery was spatially corrected using photogrammetric data. Different endmember compositions of Chlorite (Mg- and Fe- substitutions) and phengitic muscovite minerals were mapped at core and outcrop scale using Mixture Tuned Matched Filtering (MTMF) classification. Point spectroscopy was used to validate outcrop mapping results.

## 2.3. Analysis of economic materials

Examples of hyperspectral imaging to enhance economic material extraction, either by increasing safety of geologic investigations, or by improving efficiency are described. In most cases, validation techniques were used, although they are not the focus of this section. Various types

of deposits have been studied at different spatial scales and spectral ranges ([Table 3](#)).

### 2.3.1. Clay minerals

[Murphy et al. \(2015\)](#) studied clay minerals using SWIR imagery in an iron ore mine that is located in Western Australia. Automatic registration to LiDAR data demonstrates an efficient way to geometrically correct hyperspectral imagery for accurate calculation of mineral abundances. Mineral abundances were inferred from locations of absorption minima and depths of absorption features in an automated feature extraction approach.

[Alonso de Linaje and Khan \(2017\)](#) imaged cretaceous sandstones and claystones in a quarry in northern Spain. High spatial resolution field and sample data made it possible to distinguish well-ordered (kaolin or china clay) and poorly ordered kaolinite (ball clay). Distinguishing between these endmember clay types has implications for mining operations, such as imaging to detect the desired clay composition for extraction.

### 2.3.2. Silver and copper deposits

[Kruse et al. \(2012\)](#) used airborne, ground-based, and laboratory HSI in a silver mine near Reno, Nevada. Distributions and relative abundances of SWIR-active minerals: illite-muscovite, jarosite, and kaolinite were mapped in plan view, outcrop, and drill cores. Higher abundance of jarosite was correlated with areas where high-grade silver ore was mined. Samples from copper porphyry deposits were also analyzed using HSI: [Kokaly et al. \(2017\)](#) studied the Cu-Au-Mo porphyry deposits at Orange Hill and Bond Creek, Alaska. Longer wavelength, phengitic white mica was spatially associated with clinochlore, suggesting

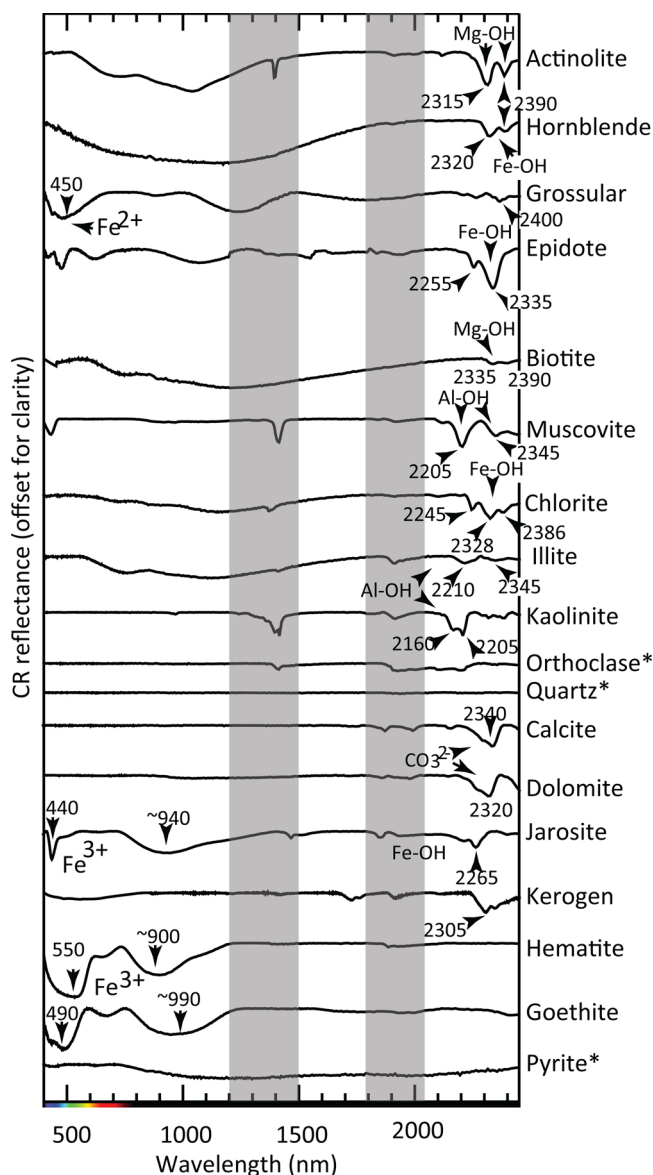


**Fig. 2.** Continuum removed (CR) reflectance spectra of observed minerals in the study areas. Vibration in metal -OH bonds and the planar CO<sub>3</sub><sup>2-</sup> ions cause absorption features of most minerals in SWIR, whereas electronic processes cause absorption in VNIR. Portions of the spectrum where energy is absorbed by atmospheric gases are denoted by gray rectangles. \*No distinguishing features in VNIR or SWIR wavelengths. Data from Clark et al. (2007) and Clark et al., 1990.

hydrothermal fluid alteration as a source of economic deposits. Longer wavelength, phengitic white mica was spatially associated with clinochlore, suggesting hydrothermal fluid alteration as a source of economic deposits.

Dalm et al. (2017) studied samples using SWIR imaging to map chlorite composition, white mica crystallinity and composition, tourmaline, nontronite, kaolinite, and opaque minerals. Principle Component Analysis (PCA) was conducted to analyze relationships between spectral features of minerals and ore grade. More than half of the samples that had sub-economic ore grade could be differentiated using PCA. Graham et al. (2018) conducted imaging spectroscopy of rock samples collected from porphyry copper deposits in remote areas of Alaska, in conjunction with aerial hyperspectral surveys. A relationship was observed between clinochlore and longer wavelength white mica (associated with lower Al and higher Si and Mg content) occurrence and porphyry mineralization at sample and regional scale.

### 2.3.3. Hydrothermal alteration

Greenberger et al. (2015a) used field and laboratory imaging spectroscopy, as well as Raman spectra, x-ray diffraction (XRD), inductively-coupled plasma-atomic emission spectroscopy (ICP-AES), and other elemental analyses to study lacustrine pillow basalts as an analogue for volcanic-lacustrine interactions on Mars. The combination of these techniques could be useful for studying hydrothermally altered terrains. Hyperspectral imagery provided continuous compositional data, allowing for conceptual model development in hydrothermal systems. Greenberger et al. (2015b) applied multi-scale imaging spectroscopy for several examples including laboratory imaging of serpentine-bearing rock, hydrothermally altered pillow basalt, and a carbonaceous chondritic meteorite. Imaging at outcrop scale for stratigraphic analysis of a sedimentary sequence was also conducted.

### 2.3.4. Hydrocarbons

Speta et al. (2013) and Speta et al. (2015) imaged oil-saturated sands in the laboratory setting. Wavelet analysis, which applies wavelet transforms to reflectance spectra, and broadband modelling, which estimates bitumen content directly from resampled hyperspectral reflectance data (Rivard et al., 2010), were compared. These models were applied to spectral features in the SWIR region (1700 and 2300 nm) to estimate bitumen content. Bitumen concentration was measured using Dean Stark analysis, finding a correlation between measured bitumen and predictions derived from spectral imagery. Mehmani et al. (2017) used broadband wavelet modelling to estimate kerogen content in shale core samples, incorporating only several bands that are diagnostic of hydrocarbons. The use of fewer bands for reliable kerogen prediction would make it possible to apply cheaper NIR band-pass filters to sample only the wavelengths of interest for a feasible and inexpensive solution to kerogen quantification. Rivard et al. (2018) also used wavelet transformation to predict total organic carbon (TOC) using SWIR data. Within the wavelet domain, high thermal maturity shale could be distinguished from low maturity.

Detection of hydrocarbons in soils is of interest, due to the potential for spill detection and for the purpose of detecting seeps for exploration (Asadzadeh and de Souza Filho, 2017). Hydrocarbon concentration in various mineral substrates was investigated by Scafutto et al. (2016), with the aim of using these results for mapping hydrocarbon contamination from an airborne and satellite-based platform (Scafutto et al., 2017). Results of both of these studies demonstrate the possibility of detecting hydrocarbon concentrations that are as low as 4 % (by weight) in hyperspectral data collected in the laboratory and from an airborne platform.

### 2.3.5. Other applications and techniques

Although it was not related to mining or mineral extraction, it could be noted that the early studies that applied laboratory-based HSI to geoscience studies used sensors that collected data in the VNIR wavelengths, such as Lee et al. (2005), who used scanning electron microscopy in conjunction with cathodoluminescence with longer dwell times to produce hyperspectral maps of calcite cements collected from Permian rocks found in northeast England. Recently, hyperspectral cathodoluminescence (CL) was used to analyze REE enriched apatite within a carbonatite complex, finding relative enrichment of REEs in areas that have higher CL intensity (Slezak et al., 2018).

Denk et al. (2015) used SWIR HSI and LiDAR scanning to study an iron and steel dump site. Spectral feature fitting (SFF) and spectral angle mapper (SAM) were used to classify iron-bearing materials in the dump site; however, the need for imaging in VNIR wavelengths was apparent, as a continuous spectrum across these spectral regions would better constrain iron-bearing minerals due to their diagnostic absorption features in the VNIR domain.

Tappert et al. (2015) imaged drill cores collected near a diamond mine in the Northwest Territories, Canada using SWIR and LWIR scanners to map the extent of kimberlite dilution. The high spatial

resolution of this method made it possible to map micro- and macro-dilution, which would not be possible using only visual core logging methods.

Recently, thermal infrared (TIR) sensors were used in an outdoor setting. Lorenz et al. (2018a) used a LWIR imaging system to scan a gravel quarry where hydrothermal sulfide mineralization is hosted in granitic rocks. LWIR imaging allows for the advantage of mapping quartz and plagioclase minerals while also discriminating alteration phases such as chlorite, muscovite, and calcite. Kirsch et al. (2018) combined VNIR, SWIR, and LWIR imaging with a SfM-generated point cloud to map sulfide and granitic rock exposure in a quarry in Saxony. Original and alteration minerals were mapped as a result of spectral continuity, which allowed Quartz-bearing host rocks to be distinguished from altered zones. Boutanga-Tombet et al. (2018) presents the use of LWIR HSI in a limestone cement quarry, where various carbonate minerals such as calcite, dolomite, siderite, magnesite, aragonite, ankerite, rhodochrosite, strontianite, cerrucite, witherite, and malachite were identified. Feng et al. (2018) combined airborne HSI data in the SWIR and TIR ranges using continuous wavelet analysis, to

distinguish materials that have spectral features only within a specific wavelength range; this facilitated mapping ultramafic rocks, which typically have low spectral contrast. Laakso et al. (2019) investigated HSI of various REE-containing minerals, and found that there were no distinct features that can be used to distinguish REEs from one another.

Hyperspectral sea floor mapping was conducted recently. Sture et al. (2017) imaged submerged massive sulfides near Loki's Castle, which is a black smoker hydrothermal complex in the Mid-Atlantic Ridge between Greenland and Norway, demonstrating the potential of identifying mineral reserves underwater, possibly without the need for physical sampling. Dumke et al. (2018) imaged manganese nodules in the Peru Basin, demonstrating the utility of underwater HSI for deep sea exploration, and applications of this type of imaging to environmental monitoring.

#### 2.4. Validation of mineralogy in economic deposits

Validation is significant to HSI studies, as it is critical to establish a correlation between spectral properties and mineral or material

**Table 1**

Common silicate (A) and non-silicate (B) minerals and materials of interest in studies that focus on imaging spectroscopy for geologic applications after Kosanke et al. (2017).

A	Mineral Structure/type	Mineral Group	Example	VNIR Response	VNIR feature location(s) (nm)	SWIR Response	SWIR feature location (s) (nm)	LWIR Response	LWIR feature location(s) (nm)
Silicates	Ino-silicates	Amphibole	Actinolite	Non-Diagnostic	N/A	Good	2315, 2390	Moderate	2700
		Pyroxene	Diopside	Good	655	Moderate	1055, 2310	Good	2900, 4000, 5070, 10060
	Cyclo-silicates	Tourmaline	Elbaite	Non-Diagnostic	N/A	Good	2175, 2205, 2255, 2305	Moderate	2820
		Garnet	Grossular	Moderate	weak ~440	Moderate	2200 and 2400	Good	2750, 5870, 9200, 11200, 11700
	Neso-silicates	Olivine	Forsterite	Non-Diagnostic	N/A	Good	1000-1010	Good	11000, 12000, 23000
		Epidote	Epidote	Non-Diagnostic	N/A	Good	2255, 2335	Moderate	9800, 10850, 16000
	Phyllo-silicates	Mica	Muscovite	Non-Diagnostic	N/A	Good	2200, 2350	Moderate	6000, 8300, 9300,
			Phengite	Non-Diagnostic	N/A	Good	2220, 2350	Moderate	6000, 8300, 9300,
		Chlorite	Fe-chlorite	Non-Diagnostic	N/A	Good	2260, 2360	Moderate	12000, 17000
			Mg-Chlorite	Non-Diagnostic	N/A	Good	2245, 2325	Moderate	12000, 17000
	Clay minerals	Illite	Non-Diagnostic	N/A	Good	2200-2220, 2350	Moderate	2750, 6100, 7900	
		Kaolinite	Non-Diagnostic	N/A	Good	2160, 2205	Moderate	2750, 5500, 8000, 9000, 9800	
		Talc	Non-Diagnostic	N/A	Good	2284, 2310, 2384	Moderate	2700, 8000, 9500	
Tecto-silicates	Feldspar	Orthoclase	Non-Diagnostic	N/A	Non-Diagnostic	N/A	Good	7850, 12650	
		Albite	Non-Diagnostic	N/A	Non-Diagnostic	N/A	Good	7850, 12460	
	Silica	Quartz	Non-Diagnostic	N/A	Non-Diagnostic	N/A	Good	8400, 9200	

(continued on next page)

**Table 1** (continued)

B	Mineral Group	Example	VNIR Response	VNIR feature location(s) (nm)	SWIR Response	SWIR feature location (s) (nm)	LWIR Response	LWIR feature location(s) (nm)
Non-Silicates	Carbonates	Calcite	Non-Diagnostic	N/A	Good	2282, 2340	Good	2540, 11600, 14000
		Dolomite	Non-Diagnostic	N/A	Good	2315-2320	Good	2515, 11400, 13600
	Hydroxides	Gibbsite	Non-Diagnostic	N/A	Good	2270	Moderate	11000
	Sulfates	Alunite	Moderate	weak ~500	Good	2165, 2316	Moderate	2870, 9500, 12400
		Jarosite	Moderate	weak ~440	Good	2268	Moderate?	2900, 4900, 5000, 12500
		Gypsum	Non-Diagnostic	N/A	Good	2170, 2210, 2260	Good	4500, 6000, 6110
	Borates	Borax	Non-Diagnostic	N/A	Moderate	2140	Non-Diagnostic	N/A
	Halides	Halite	Non-Diagnostic	N/A	Non-Diagnostic	N/A	Moderate?	3000, 6000, 6950
	Phosphates	Apatite	Moderate	~745	Non-Diagnostic	N/A	Good	2830, 3400, 4000, 5000, 6800, 8500, 10400
	Oxides	Hematite	Good	650, 900	Non-Diagnostic	N/A	Non-Diagnostic	N/A
		Chromite	Non-Diagnostic	N/A	Non-Diagnostic	N/A	Non-Diagnostic	N/A
		Neodimium oxide	Good	580, 740, 800, 870	Moderate	2335	Moderate	2770, 4800, 5200, 5800, 7400, 15000
		Europium oxide	Good	470	Good	2060	Moderate	~6600, 7200, 11800, 14200, 19000, 22000
		Samarium oxide	Good	410	Good	1085, 1240	Moderate	3000, 8400, 8900, 9350
	Sulfides	Pyrite	Non-Diagnostic	N/A	Non-Diagnostic	N/A	Moderate	~3000, 6000
		Chalcopyrite	Non-Diagnostic	N/A	Non-Diagnostic	N/A	?	?
		Bornite	Moderate	weak ~600	Non-Diagnostic	N/A	?	?
		Molybdenite	Moderate	584 and 654	Non-Diagnostic	N/A	Moderate	~3000
	Hydrocarbons	Bitumen	Non-Diagnostic	N/A	Moderate	2300, 2357	Moderate	3400

Only features in the VNIR and SWIR wavelengths are shown, due to the use of these sensors in the majority of ground-based HSI publications. Also, absorptions that are within the range of atmospheric absorption bands (approximate locations in the SWIR domain: 1300-1500, 1750-2000, 2450-2800 nm) (Horvath, 1993) are omitted due to uncertainty of detection in an outdoor setting. Data from (Boesche et al., 2015; Brossard et al., 2016; Clark, 1999; Clark et al., 1990; Clark et al., 2007; Cloutis et al., 2006; Feng et al., 2006; Gallie et al., 2002; Hunt and Salisbury, 1970; Izawa et al., 2018; Kokaly et al., 2017; Kosanke et al., 2017; Lyder et al., 2010; Mustard, 1992; Qiu et al., 2017; Sheibley and Fowler, 1966; Speta et al., 2013; White, 1967; Zaini et al., 2012; Zaini et al., 2014).

abundance that would be mapped. Numerous mineral deposits have distinct spectral features, or their host and/or alteration products can be used as a proxy for such deposits. The studies presented lay the groundwork for mineral exploration by confirming the accuracy with which close-range HSI-based mapping can be conducted (Table 4).

#### 2.4.1. Sulfide minerals

Bolin and Moon (2003) and Swanson (2005) tested the feasibility of using HSI in VNIR wavelengths for quantifying sulfide minerals in the Stillwater Complex, scanning hand specimens in an indoor setting. Bolin and Moon (2003) found a correlation between visual point counts of sulfides and their Minimum Noise Fraction Transformation (MNF)

characteristics in the presence of other mafic and ultramafic minerals: feldspars, pyroxenes, and olivines. Although sulfide minerals do not have distinctive features in VNIR or SWIR wavelengths, the contrast in color and brightness made it possible to distinguish them in this case. On average, there was agreement between independent point counts of sulfides and Spectral Angle Mapper (SAM) classification of the abundance of sulfides, with spectral mapping techniques underestimating sulfide abundance from 2.5–0.5 % in five samples. This underestimation is attributed to metal ion substitution, such as Ni or Co for Fe in the crystal lattice (Bolin and Moon, 2003). Fox et al. (2016) used TIR data to study a drill core in a volcanic hosted massive sulfide district and a porphyry Cu-Au deposit. Carbonate minerals were of interest in

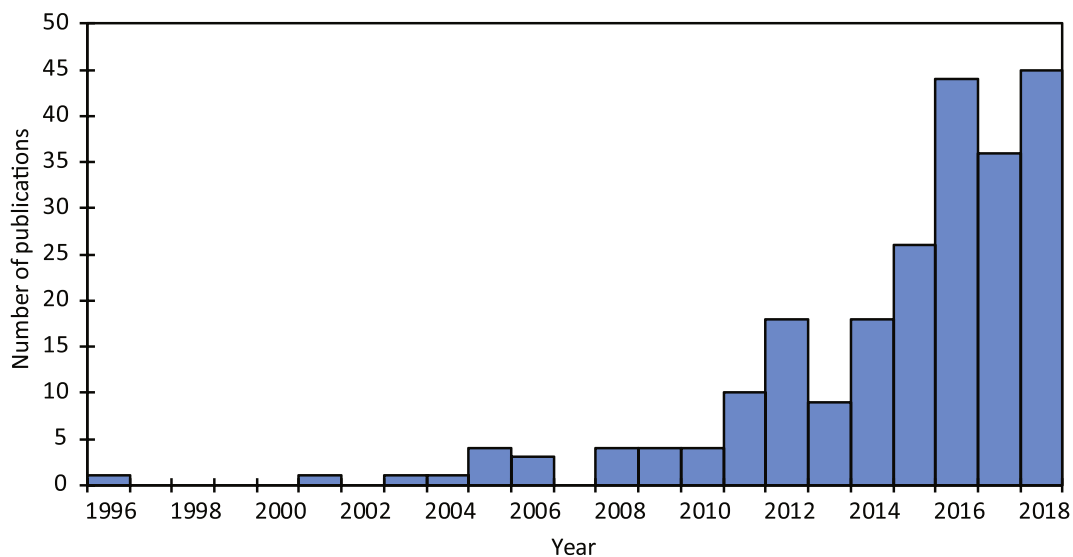


Fig. 3. Peer-reviewed publications that utilize terrestrial (ground-based) or laboratory HSI for geoscience applications. The search was done in early 2019.

this study due to their acid neutralization capacity. XRD and electron microprobe analyses (EMPA) were used to confirm spectral mapping results.

#### 2.4.2. Iron bearing minerals

Murphy and Monteiro (2013) studied an iron ore deposit within a banded Iron Formation in Western Australia, using HSI in the VNIR wavelengths (430–970 nm). Abundance of iron minerals (hematite and goethite) was calculated using 1st, 2nd, and 4th derivative reflectance, which was correlated to abundances derived from XRD analysis using linear regression. It was determined that for this setting, 4th derivative reflectance had the strongest correlation (lowest  $R^2$  values) with measured mineral abundance. Ramanaidou et al. (2015) demonstrates the study of iron ore using HSI and Raman spectroscopy. HSI was conducted in VNIR SWIR, and TIR wavelengths, and Raman spectroscopy in mid and far infrared wavelengths.

Silversides and Murphy (2016) scanned drill cores using an HSI system, also validating results using point spectroscopy. Marker shale beds in a banded iron formation are identified by a higher signal of kaolinite and  $\text{Al}_2\text{O}_3$ . Shale abundance delineated by HSI was compared

to shale response in natural gamma-ray log. The weight percent of kaolinite and  $\text{Al}_2\text{O}_3$  were determined from XRD and X-ray fluorescence (XRF), data, respectively, and correlated to the intensity of the 2202 nm spectral feature. This study also notes similarities between gamma ray log measurements and spectroscopic measurements that are within the clay absorption range, despite differences in magnitude of gamma ray and spectroscopic intensities. This suggests that spectroscopic measurements at outcrop scale can be related to downhole logs for improved models of ore deposits.

Gossans form as a result of surface oxidation of sulfide-bearing rocks, are typically composed of iron oxide minerals, and can be a proxy for ore deposits (Taylor, 2011). Laakso et al. (2016) combined laboratory and airborne HSI to map gossans in an area with abundant lichen cover. The findings of this work demonstrate the possibility of discerning thickness of gossans, and also that lichen encrustation on thin gossans causes a shift in the iron absorption feature located between approximately 880 and 1060 nm toward shorter wavelengths.

#### 2.4.3. Rare earth elements

REEs are necessary for production of batteries, LCD displays,

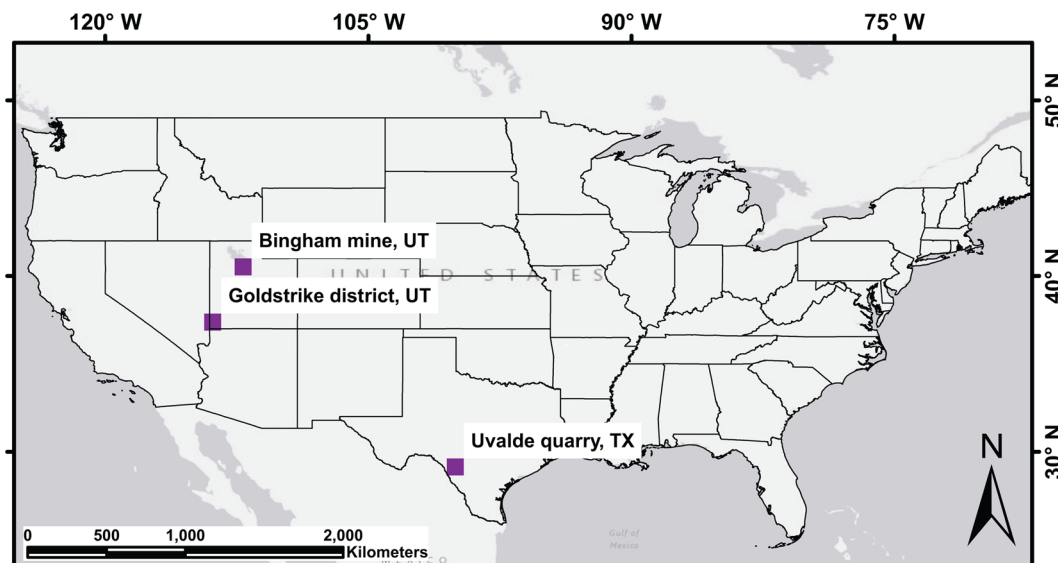


Fig. 4. Locations of case studies that are presented.

**Table 2**  
Publications demonstrating innovative methods and/or applications of data correction and integration with topographic data.

Summary	Spectral range of HSI (nm)	Challenge addressed/investigated	Material/deposit studied	Field, lab, or combined HSI	Reference
Classified hyperspectral imagery is projected onto a photorealistic LiDAR-based 3D model	1300–2500	Registration with topographic data	Limestone and dolomite	Field	Kurz et al. (2008)
Integration of hyperspectral and LiDAR data for delineating lithology, creating vectors of geologic horizons					Kurz et al. (2011)
Another example of hyperspectral and LiDAR data fusion – 2 case studies presented; limestone and sandstone			Limestone, sandstone		Buckley et al. (2012)
Detailed workflow for hyperspectral and LiDAR data integration is outlined	1300–2500				Kurz et al. (2013)
Semi-automated technique for hyperspectral and LiDAR data registration using the scale invariant feature transform (SIFT) to extract points.	1300–2500 mm		Sandstone, shale, carbonates Limestones and clays		Sima et al. (2014)
Combined hyperspectral and LiDAR data with manually-selected homologous points, used geometrically corrected hyperspectral data to quantify the abundance of sand and shale	890–2500 nm	Integration with topographic data for geological interpretation / precise measurement	Shale and sandstone		Snyder et al. (2016)
Combined hyperspectral and LiDAR data for fracture characterization to quantify the density of fractures extracted from LiDAR	2147–2391 nm		Limestone and chert	Combined	Sun et al. (2017)
Speckle sharpening, multi-temporal averaging to increase SNR in sub-optimal illumination conditions	350–2500 nm	Illumination compensation	Carbonatite hosting REE	Field	Boesche et al. (2015)
Shadow restoration using a scale factor calculated from a ratio of active (LiDAR) reflectance to passive (HSI) at the same wavelength (1550 nm)	970–2500 nm		Limestone quarry		Hartzell et al. (2017)
Radionometric and atmospheric correction was applied to hyperspectral data, and registration with topographic data derived from SfM allows for topographic and geometric correction of hyperspectral imagery.	380–2500 nm	Atmospheric and topographic correction	Pb-Zn deposit in marble, and a Volcano-genic Massive Sulfide deposit		Lorenz et al. (2018b)
Integration of vessel – based hyperspectral imagery with SfM-generated topography data for imaging large areas – cliffs along the western coast of Greenland.	380–2500 nm	Integration of HSI data with SfM-generated topography	Volcanogenic massive sulfide deposit		(Rosa et al., 2017; Salehi et al., 2018)
A workflow is developed for applying radiometric, geometric, and topographic corrections to HSI data collected aboard UAS	504–900 nm	Toolbox for processing drone-borne HSI	Volcanogenic massive sulfide deposit, lignite mine		Lorenz et al. (2017)

**Table 3** Examples where close-range HSI is used to map alteration and analyze various economic materials.

Summary	Spectral range of HSI (nm)	Material/deposit studied	Field, lab, or combined HSI	Reference
Mineral mapping in an open pit mine to improve safety in geologic investigation of physically inaccessible areas.	450–1000	Rare-earth elements, specifically lanthanides	Combined	McHugh et al. (2001)
Mineral mapping in two mines, variations in chlorite, the possibility of direct estimates of nickel and iron ore is suggested. Safety is increased by the possibility of mapping harmful substances such as asbestos.	400–2500	Copper, nickel laterite, and iron ore	Combined	Fraser et al. (2006)
Hyperspectral and LiDAR data were used to quantify clay minerals in an open-pit mine.	900–2500	Phyllosilicates: kaolinite, illite, nontronite, and talc	Field	Murphy et al. (2015)
Mapping by-products of iron and steel industry using materials of known composition as classification endmembers.	1500–2500	Iron ore, slag, sludge, and scrap metal	Field	Denk et al. (2015)
Mapping kaolinite and illite using traditional classification techniques and kaolinite crystallinity index, which exploits the doublet at ~2160 nm	896–2503	Clay minerals: kaolinite and illite	Combined	Alonso de Linaje and Khan (2017)
Multi-scale mapping of a silver deposit reveals horizons of increased kaolinite and jarosite that correspond to higher silver concentrations.	400–2450	Silver deposit	Field	Kruse et al. (2012)
Principal component analysis applied to spectral maps of samples from a porphyry copper deposit to distinguish samples with sub-economic copper grade.	1000–2500	Copper Porphyry	Field	Dalm et al. (2017)
Airborne and laboratory HSI reveal an association between longer wavelength micas and clinochlore with Cu-Mo-Au anomalies	949–2508	Pillow basalt (hydrothermal alteration)	Combined	Kokaly et al. (2017); Graham et al. (2018)
Mapping hydrothermal alteration of pillow basalt, inferring temperatures of hydrothermal fluids using mineralogy and reconstruction of diagenetic events.	420–2500	Hydrocarbons	Lab	Greenberger et al. (2015a); Greenberger et al. (2015b); Speta et al. (2013); Speta et al. (2015)
Specular characteristics of oil sands are measured, and total bitumen content is inferred using wavelet analysis.	1000–2500			Scattutto et al. (2016)
Scanning soils with various mineral abundances, impregnated with known concentrations of hydrocarbons	970–2500			Mehmami et al. (2017)
Broadband modelling of kerogen content in an immature shale	1000–2500			Rivard et al. (2018)
Wavelet transformation to predict total organic content, SiO <sub>2</sub> , Al <sub>2</sub> O <sub>3</sub> , Al/Si, K <sub>2</sub> O, and CaO in shale.	970–2510 and 7400–12100			
Macro- and microdilution in hypabyssal kimberlite was mapped in a diamond mine.	1900–2360 and 8100–11100	Kimberlite	Lab	Tappert et al. (2015)
Mapping hydrothermal alteration using linear spectral unmixing; quartz, calcite, and albite were used as endmembers.	7700–111800	Sulfide mineralization in granitic host	Field	Lorenz et al. (2018a)
Ground based and UAV – mounted HSI used to study hydrothermally altered granitic rock, UAV-mounted HSI allows for large-scale imaging.	380–2500 and 7700–111800	Sulfides, granitic rocks	Field	Kirsch et al. (2018)
Temperature emissivity separation was conducted on a carbonate mine face, and spectral unmixing was used for mineralogical mapping.	7700–111800	Limestone	Field	Boutangat-Tombet et al. (2018)
Underwater HSI using artificial illumination, using an autonomous underwater vehicle.	380–800	Sulfides	Field (underwater survey)	Sture et al. (2017)
Deep water HSI of manganese nodules in to assess the potential of mapping mineral deposits in deep sea mining areas.	400–750	Manganese	Survey	Dumke et al. (2018)

**Table 4**  
Papers reviewed that focus on validation of ground-based hyperspectral mapping results.

Summary	Spectral range of HSI (nm)	Method used for validation	Material / deposit studied	Field, lab, or combined HSI	Reference
Mapping sulfides in the absence of diagnostic features, comparison of classification to point count abundances	444–796	Independent point count	Sulfides	Lab	Bolin and Moon (2003)
Separating iron ore from shale using derivative analysis, correlation of XRD results to point spectroscopy from representative samples.	430–970	XRD and point spectrometry	Iron ore	Field	Murphy and Monteiro et al. (2013)
Comparison of HSI with Raman point spectroscopy for iron mining.	380–2500	Raman point spectroscopy		Combined	Ramanaldou et al. (2015)
Comparison of drill core HSI with point spectroscopy and gamma ray log, suggesting a method for improved ore deposit modelling.	400–2500	Point spectroscopy, gamma ray log, XRD, and XRF		Lab	Silversides and Murphy et al. (2016)
Mapping REE in drill core, comparison to previous geochemical work.	396–2530	XRD, geochemical assay	REE	Lab	Turner et al. (2014)
Algorithm development for REE spectral mapping	350–2500	ICP-AES, XRF, EMPA		Field	Boesche et al. (2015)
Mapping alteration minerals associated with a uranium deposit. Correlation established between petrography-derived mineral abundance and spectral mapping.	1300–2500	Thin sections	Uranium-bearing pegmatites, gneisses, and sandstones	Lab	Mathieu et al. (2017)
Mapping carnallite in drill core	1000–2500	XRF, thin sections, lab spectroscopy	Carnallite	Lab	Qiu et al. (2017)
Hyperspectral mapping at various scales: lab, outcrop, and regional (using an airborne platform). Magnesium and iron contents of white mica and chlorite were associated to absorption location, confirmed by XRF and EMPA.	Lab: 448–2500, Field: 949–2508	XRF, EMPA	Porphyry Cu-Au-Mo	Combined	Kokaly et al. (2017); Graham et al. (2018)
Mapping mineralogy in drill cores from a porphyry Cu-Au deposit, focus on vein thickness and azimuth.	380–2500	SEM-MLA	Porphyry Cu-Au	Lab	Tusa et al., 2019
Imaging rock chips with various gold concentrations, comparison to QEMSCAN mineral maps.	400–2500	QEMSCAN	Gold-bearing sulfides	Lab	Khan et al. (2018)
Outcrop-scale mapping various carbonate lithologies in a limestone quarry.	1300–2500	ICP-OES	Carbonates	Field	Kurz et al. (2012)
Mapping clays and carbonates in a roadcut, using absorption depths characteristic of clays and carbonates as a proxy for their abundance, validated by comparison of XRF results to laboratory HSI.	896–2500	XRF	Clays and carbonates	Combined	Sun et al. (2018a)

catalytic converters, and other technology. For this reason, rapid and efficient exploration is of interest. Neodymium, hosted in monazite, was mapped in the Fen complex, a hydrothermally altered carbonatite formation (Boesche et al., 2015; Boesche et al., 2016; Boesche et al., 2014; Neave et al., 2016). Distinct spectral features of Neodymium, as well as other REE are located within the VNIR and SWIR ranges and are relatively narrow (White, 1967), requiring high spectral resolution.

Turner et al. (2014) conducted VNIR and SWIR imaging of drill cores that contain rare earth ore minerals including bastnaesite, monazite, xenotime and eudialyte. Ore grade estimations were computed based on spectral absorption features and results were validated using geochemical assays and XRD as ground truth.

Boesche et al. (2015) developed an algorithm for mapping REE based on their spectral signatures. This involves applying a convolution to enhance spectral contrast within the wavelengths that are related to absorptions that are characteristic of REE. Hyperspectral mapping results were validated using laboratory geochemical techniques: ICP-AES, XRF, and EMPA. Artificial mixtures were prepared to measure spectral response to known abundances of neodymium oxide and calcium carbonate, with neodymium abundances ranging from 0.1–5 %. The depth of a spectral absorption characteristic of neodymium, located at 803 nm, increased with higher neodymium content within the mixture. Laakso et al. (2018) imaged phosphorous and REE-bearing drill core samples, using the Mineral Liberation Analyzer (MLA) and EMPA for ground truth.

#### 2.4.4. Copper, molybdenum, and gold deposits

When analyzing the white mica absorption feature in the Orange Hill Cu-Mo-Au deposit in Alaska, Kokaly et al. (2017) found a correlation between increasing Al content in white mica and decreasing wavelength of the minimum absorption location of the Al-OH feature between 2200 and 2220 nm. Al content was measured using EMPA and XRF. In a follow-up publication, Graham et al. (2018) reports an association of chlinochlore and phengitic white mica with high Cu, Mo, and Au concentrations.

Tusa et al. (2019) validated hyperspectral mapping using a Scanning Electron Microscope (SEM) equipped with the MLA software. Fully constrained linear spectral unmixing was used for the classification of veins. Based on the classification, vein thickness and azimuth were determined. Vein thickness and azimuth were validated using SEM MLA mapping results.

Khan et al. (2018) applied laboratory-based imaging spectroscopy to investigate gold mineralization in the Astore area in Northern Pakistan, an area where mineralization is associated with hydrothermally deposited base metals. Samples were imaged in the laboratory setting using VNIR and SWIR sensors and were classified using Spectral Angle Mapper (SAM) and Support Vector Machine (SVM) techniques. Classification results were compared to Quantitative Evaluation of Minerals by Scanning Electron Microscopy (QEMSCAN). Although both classification techniques produced similar mineral mapping results, SAM classification had greater similarity to QEMSCAN mineral maps than SVM.

#### 2.4.5. Clays and carbonates

Kurz et al. (2012) applied SWIR HSI combined with LiDAR scanning to study mineralogy and diagenetic features exposed in a limestone quarry in northwest Spain. Various dolomite phases, calcite, organic-rich limestone, paleokarst, and karst infill were detected, and mineralogy was confirmed using geochemical analysis – Inductively Coupled Plasma Optical Emission Spectroscopy (ICP-OES). Integration with LiDAR data produced geometrically accurate mineralogical maps that have accurate dimensions and could be used for rock volume quantification.

Sun et al., 2018a integrated outdoor and laboratory imaging for geological study, which in combination with geochemical analysis investigated the depositional history of the Eagle Ford Formation (Del

Rio, Texas, U.S.): a cyclically-deposited shale, bentonite, limestone, and marl deposit. Carbonate and clay minerals were quantified in both outcrop and hand specimens using absorption characteristics - depth and location of the minima of these absorptions. In hand specimens, a correlation was observed between depths of the Al-OH spectral absorption feature in clays (2200–2210 nm) and the CO<sub>3</sub> absorption in limestone (2320–2340 nm) with the abundances of Al<sub>2</sub>O<sub>3</sub> and CaO, respectively. This presents the potential of mapping abundance of these mineral groups using characteristics of their respective spectral features in SWIR wavelengths.

#### 2.4.6. Other deposits

Mathieu et al. (2017) analyzed drill cores in an unconformity-related uranium deposit using hyperspectral scanning in the SWIR domain. Depths of diagnostic absorption bands were used as a proxy for mineral abundance, allowing for automated mineral mapping. Thin section analysis was used as ground truth for spectral data. Qiu et al. (2017) integrated hyperspectral data to map the abundance of carnallite in drill core. Carnallite is mined for its potassium content, which is significant in the use of fertilizer in the field of agriculture. Using XRF as ground truth, a correlation between the absorption intensity at 1200 nm and potassium content was established. Rogass et al. (2017) tested a processing workflow for laboratory-based HSI using mineral powders of epidote, hornblende, chlorite, dolomite, illite, goethite, pyrophyllite, and calcite. The workflow consists of radiometric and geometric corrections, reflectance retrieval, and illumination correction. Results were compared to data collected by point spectroscopy using two different sensors. Mineral spectral curves were similar, but some differences between the two point spectrometers were observed, likely due to their sensing principles and associated signal impacts.

### 2.5. Environmental applications

Close-range HSI for environmental applications has been demonstrated in several examples (Table 5). Specifically, soil studies have been conducted, with the aim to predict the abundance of pollutants such as heavy metals, organic carbon, and carbon and nitrogen isotopic composition.

#### 2.5.1. Soil studies

Soils were imaged in the laboratory setting in various studies. Chemical analysis of soils is significant, because of the effects on their ability to store moisture, absorb environmental pollutants, and sequester CO<sub>2</sub> to organic matter. Several contributions discuss the use of ground-based HSI soil studies, mostly in the laboratory setting. Buddenbaum and Steffens (2012) used VNIR imagery to analyze soil profiles and map small-scale heterogeneities in composition, specifically iron and manganese inclusions, oxidation, and organic matter. It was determined that partial least squares regression (trained by chemically analyzed endmembers) provided accurate spectral mapping results, with or without various spectral pre-processing techniques. Kang et al. (2018) studied soil contamination by heavy metals such as Cu and Pb. Predictive modelling of several bands was conducted using Log of the inverse of reflectance values, as well as principal component analysis. The results of this study are promising for potential to use HSI in an airborne platform to identify soil contamination.

Soil organic carbon has been studied using various techniques, and quantifying carbon abundance in soil can be significant to determining the amount of CO<sub>2</sub> that is sequestered. HSI has the potential to provide rapid analysis of many samples, which would be useful. For this reason, many contributions seek to determine soil organic carbon content (Askari et al., 2013; Buddenbaum and Steffens, 2012b; Hobley et al., 2018; O'Rourke and Holden, 2012; Sorenson et al., 2018; Steffens et al., 2014; Tahmasbian et al., 2018).

O'Rourke and Holden (2012) analyzed organic carbon, total carbon, and inorganic carbon using VNIR imaging, finding that these can be

mapped with confidence in this spectral range, using dry combustion analysis results for validation. Steffens et al. (2014) studied a Histosol profile to quantify soil organic matter. Dry combustion and  $^{13}\text{C}$  NMR spectroscopy were used for validation. Spectral slopes within intervals of 638–450 nm and 800–680 nm were used as proxies for soil composition. Hobley et al. (2018) applied machine learning techniques to HSI of soil cores to quantify organic carbon. Random forest and SVM algorithms were compared, and random forest was found to be more suitable for soil organic carbon prediction due to its ability to capture more variance. Tahmasbian et al. (2018) predicted total carbon, total nitrogen,  $\delta^{13}\text{C}$ , and  $\delta^{15}\text{N}$  in soil samples using VNIR imagery by partial least squares regression, with geochemical results obtained from an isotope ratio mass spectrometer as ground truth. Correlation between soil total carbon and  $\delta^{13}\text{C}$  is hypothesized to be the mechanism by which  $\delta^{13}\text{C}$  prediction was possible, but no correlation was found between  $\delta^{15}\text{N}$ , total carbon, or total nitrogen. This work demonstrates the possibility of determining soil chemistry in the absence of prominent spectral features; this was done with the use of internal spectral correlations with other properties that do possess spectral features. Burud et al. (2016) applied partial least squares regression by comparing imaged soil samples to chemically analyzed  $\delta^{13}\text{C}$  (using a cavity ring down spectrometer coupled to a combustion module), to predict biochar content of soil samples and map the distribution of biochar.

### 2.5.2. Acid mine drainage monitoring

Oxidation of pyrite and other sulfides in mine waste can cause water percolating through the rocks to become acidic, creating environmental concerns and contaminating water resources. In these environments, secondary minerals, such as jarosite, goethite, schwertmannite, and others are found in concentric patterns around waste rock piles. The formation of these minerals is controlled by pH; for example, jarosite forms in more acidic conditions than goethite, schwertmannite, and ferrihydrite. These minerals are a proxy for acidic conditions and can be detected in VNIR and SWIR wavelengths (Swayze et al., 2000). The presence of schwertmannite and jarosite in acidic conditions was observed in experimental (Bigham et al., 1996) and natural (Valente and Gomes, 2009) settings. These have been studied using spaceborne hyperspectral (Mielke et al., 2014) and multispectral (Kopačková et al., 2012) sensors.

The potential of certain rock types to produce acid mine drainage was investigated using close-range HSI in the laboratory (Cracknell et al., 2018) and on a larger scale using UAV-based HSI (Jackisch et al., 2018). Jackisch et al. (2018) applied drone-mounted HSI to monitoring a lignite mining district for acid mine drainage. Acid-generating iron minerals -goethite and jarosite were mapped using SAM classification. Mineralogy was verified using XRD and XRF, and pH was measured to validate pH predictions that were based on hyperspectral data. Prediction of pH from drone-borne spectral data was estimated by comparing ground-based measurements with mineral abundances. This type of work seeks to close the observational gap between airborne and ground-based imaging and provides an efficient means of monitoring physically inaccessible terranes.

### 2.5.3. Gas detection

Gas detection is of interest for monitoring environmental pollutants such as methane gas leaks along pipelines as well as other sources of harmful gases. It is suggested that an array of ground-based imagers could be an accurate way to monitor pipelines, but the cost of these sensors is a limiting factor (Sivathanu, 2005). Plumes of methane have been detected using the Hyperspectral Thermal Emission Spectrometer (Hulley et al., 2016).

Chamberland et al. (2005) described a LWIR sensor that is capable of gas detection and present a field test where the movement of a cloud of  $\text{SF}_6$  is tracked. This sensor has onboard processing capabilities, making it a quick and efficient means of gas detection and monitoring.  $\text{SF}_6$  is a potent industrial greenhouse gas that is used as insulation for

**Table 5**  
Examples of environmental applications of close-range HSI.

Summary	Spectral range of HSI (nm)	Material studied	Field, lab, or combined HSI	Reference
Partial least squares regression to utilize all spectral bands for estimation of various elements in soil with high accuracy.	400–1000 400–1720	Soil organic carbon	Lab	Buddenbaum and Steffens (2012b) O'Rourke and Holden, 2012,
Quantifying soil organic carbon, total carbon, and inorganic carbon were determined using lab HSI and confirmed using dry combustion.	410–990			
Mapping spectral variability in a soil profile using slopes of certain spectral intervals.	400–990			
Application of random forest and SVM algorithms to hyperspectral imagery of soil core samples	400–990			Steffens et al. (2014)
Mapping organic carbon and total nitrogen in soils using continuous wavelet transform and a second order Gaussian transform.	400–2500			Hobley et al. (2018)
Prediction of $\delta^{13}\text{C}$ and $\delta^{15}\text{N}$ in soil samples using VNIR data.	400–1000 1000–2500	Biochar		Tahmasbian et al. (2018)
Partial least squares regression modelling of carbon concentration in biochar, SAM used for mapping biochar distribution.	504–900	Lignite mining district	Field	Burud et al. (2016) Jackisch et al. (2018)
Mapping acid-generating minerals goethite and jarosite, pH prediction from hyperspectral data, validated by ground-based measurements (XRD, XRF, pH).	7407–12500 7500–12000	$\text{SF}_6$ , $\text{CO}_2$ , propane and butane mixture, and freon 134	Field	Chamberland et al. (2005) Kastek et al. (2012)
Tracking $\text{SF}_6$ cloud movement		Methane and $\text{SF}_6$		
Partial least squares regression detection and characterization algorithm is discussed	6944–10810 7700–11800 2564–16670	$\text{SO}_2$ $\text{NH}_3$ gas		Smeekens and Goulier (2018) de Donato et al. (2018)
Described instrument and algorithm for remote gas detection, field tests.				
Imaging volcanic gas emission				
$\text{NH}_3$ detection using an imaging FTIR spectrometer, 3-D modelling of gas plume.				

transmission and distribution of electrical energy (Rabie and Franck, 2018). Kastek et al. (2012) used an Infrared Fourier transform spectrometer (IFTS) to detect and locate CO<sub>2</sub>, a propane-butane mixture, and Freon 134 gases at distances of 20 and 60 meters. Sabbah et al. (2012) describe an instrument and an algorithm for gas imaging that improves detection limits by enhancing signal to noise ratio. Methane was detected in foggy conditions and at a distance of 250 meters. SF<sub>6</sub> was also detected at a distance of 800 meters. The concentration of SF<sub>6</sub> was tracked over time.

Smekens and Gouhier (2018) used a TIR imager to track SO<sub>2</sub> emitted at craters on Stromboli Island, Italy. Spectral indices were developed that reliably identified SO<sub>2</sub> even in high humidity, fog, ash, etc. Data are collected from various viewing angles over three days for one location, and two days for another. Brightness temperature difference was used to apply qualitative SO<sub>2</sub> indicators, based on the spectral shape of SO<sub>2</sub>. Time series analysis displayed varying concentrations of SO<sub>2</sub> that were comparable to field observations. This work has implications for SO<sub>2</sub> monitoring in other locations, and from industrial sources.

de Donato et al. (2018) measured NH<sub>3</sub> using a Fourier Transform Infrared imaging spectrometer. Stereoscopic measurements, i.e. multi-angle observations, were used for 3D reconstruction of the gas plume. The spatial boundary of the gas plume was mapped, and the volume of the plume was computed. Remote 3-D reconstruction of a gas plume has significant implications for monitoring capability.

## 2.6. Automation

The potential of mining being guided by autonomous lithologic mapping using a hyperspectral sensor has been investigated both in the economic (Nageshwaraniyer et al., 2018) and technical (Job et al., 2017; Schneider et al., 2012; Schneider et al., 2011b) respects. Gaussian processes (GP) with squared exponential (SE) and observation angle dependent (OAD) covariance functions were found to outperform SAM classification in separating ore from shale in an open pit mine under variable illumination conditions, using an independent spectral library, thus omitting user input. More accurate classification was derived using GP-OAD v.s. SAM and GP-SE when it comes to classifying areas under shadow; GP-OAD and SAM yielded more accurate classification when training data are collected under different conditions than the image (noise, illumination) (Schneider et al., 2011a). These findings were confirmed in a follow-up study that also used GP-OAD on a fused product of VNIR and SWIR HSI to delineate ore and shale zones. This study suggests the potential for using an autonomous ground vehicle, on which hyperspectral sensors would be mounted to guide mining operations (Schneider et al., 2012). With the use of artificial illumination, Kurz et al. (2017) studied a subsurface construction site using HSI, suggesting the potential and feasibility of using this technique for underground mining. Nageshwaraniyer et al. (2018) demonstrated economic optimization of a copper mine using a multispectral sensor, which collects five bands in the VNIR range.

Uezato et al. (2014) presented a spectral unmixing technique within a multi-task Gaussian process (MTGP) framework. This approach accounts for spectral variability within each endmember class by allowing the number of endmember types in each pixel to vary. This method was tested using synthetic hyperspectral data that were generated from 20 spectral curves of known substances. Also, it was tested using real HSI data collected in the laboratory setting (Murphy et al., 2014b).

Automated classification using the MTGP - based machine learning algorithm was found to outperform SAM classification (Chlingaryan et al., 2015). Unlike some machine learning techniques that require training data from within the hyperspectral data cube (Aguilar et al., 2000; Zhang et al., 2018), the MTGP technique can use input endmember spectra from other measurement techniques such as a laboratory spectroradiometer, allowing for validation of mineralogy and geochemistry using techniques such as XRD, ICP-MS, and others.

Overall, in comparison to SAM, MTGP was able to distinguish spectrally similar classes with greater accuracy (Chlingaryan et al., 2015).

Windrim et al. (2018) applied convolutional neural networks to ground-based HSI from the iron ore mine that was studied previously in (Murphy et al., 2014a). It is noted that this approach can be time consuming due to the requirement of a large volume of training data. Using training data from the computer vision community for pre-training (i.e. pre-training a base network), then fine tuning the training dataset on the target image, is referred to as transfer learning and can be an efficient way to apply convolutional neural networks. The possibility of using publicly available data for pre-training can increase the accuracy of classification of new images. In another approach, Contreras Acosta et al. (2019) used Mineral Liberation Analyzer (MLA) data to train a random forest classifier, allowing for the expansion and up-scaling of mineralogical mapping (Table 6).

## 3. Original case studies

Three case studies of ground-based HSI in economic deposits in the U.S. are presented: a Carlin-style gold deposit near Saint George, Utah, a Cu-Mo-Au deposit near Salt Lake City, Utah, and a bituminous limestone quarry near Uvalde, Texas (locations shown in Fig. 4).

### 3.1. Materials and methods

Similar data collection and processing procedures were applied to three case studies where HSI was conducted in mine and quarry settings. Differences in classification approaches are discussed in the following sections.

#### 3.1.1. Study locations, geologic context

**3.1.1.1. Goldstrike mining district.** This work was conducted in the Goldstrike district, which is located approximately 50 kilometers (35 miles) northwest of St. George in southeastern Utah, near the eastern edge of the Basin and Range Province. This region has been explored for gold since the 1870s. The first gold deposits were believed to have been found in coarsely crystalline calcite veins in the Hamburg mine (location shown in Fig. 5) (Willden, 2006).

The oldest units exposed in the district, dolomites and limestones of Devonian and Mississippian age, were likely deposited as the open shelf environment transitioned to a distal foreland basin during the Devonian-Mississippian Antler orogeny in central Nevada (Rowe et al., 2018; Speed and Sleep, 1982). Pennsylvanian to Permian shallow water and supratidal carbonates were deposited in an inner platform setting with periodic input of siliciclastic material from the continental margin to the east (Rowe et al., 2018). Mesozoic units in the district are mostly siliciclastic and are related to Cretaceous basin development related to the Sevier orogeny. Continuing tectonism into Eocene time is suggested by the presence of sandstone and conglomerate deposits of Eocene to Oligocene age, including the Claron formation (Adair, 1986). Sedimentary rocks are overlain by Oligocene and Miocene volcanic rocks of intermediate to felsic composition, such as andesite flows and tuffs. These units extend into eastern Nevada, and are likely due to a “flare-up” of igneous intrusion during this time (Axen et al., 1993; Coney et al., 1978). Fig. 6 shows the stratigraphy of the area.

Paleozoic marine carbonate and clastic strata, overlain by Jurassic sandstones, and were folded and thrusted by southeast-directed Sevier-style deformation during the late Cretaceous (Adair, 1986). A north-east-trending anticlinal structure deforms the Paleozoic sequence. In some locations, near-vertical bedding occurs, likely as a result of fault-propagation folding (Willden, 2006). Following the Sevier orogeny, rocks younger than Permian age were eroded away in this area, resulting in an unconformity. During Miocene time, east-northeast and west-northwest trending extensional and strike-slip faults formed after deposition of the volcanic tuffs. During this time, the Goldstrike Graben was formed; an event that likely had some control on the pattern of

**Table 6**  
Example publications that discuss machine learning techniques for ground-based HSI classification and the application to mining automation.

Summary	Spectral range of HSI (nm)	Technique	Material studied	Field, lab, or combined HSI	Reference
Comparison of GP-SE, GP-OAD, and SAM classification techniques A system for mining automation guided by hyperspectral sensing. Interconnected multi-task framework is developed for classification.	400–2500 400–2500 1000–2500	GP-SE and GP-OAD GP-OAD MTGP	Iron-bearing shale Iron ore Banded iron formation and shale	Field Field Lab	Schneider et al. (2011b) Schneider et al. (2012) Chilengaryan et al. (2015)
Algorithm developed for determining the number of endmember types in each pixel, evaluated the technique using real and simulated hyperspectral data.	400–2500	MTGP	Hematite, Goethite, and Kaolinite	Lab	Uezato et al. (2014)
Using publicly available data for pre-training convolutional neural network classifiers.	989–2448	Convolutional neural networks	Banded iron formation and shale	Field	Windrim et al. (2018)
Using SEMI-based Mineral Liberation Analysis to train a random forest classifier	380–2500	Random Forest	Unspecified	Lab	Contreras Acosta et al. (2019); Contreras et al. (2018)

disseminated gold mineralization. The Goldstrike graben is bounded by the Hamburg fault on the south and the Hassayampa fault on the north (Fig. 5B). Eight known ore deposits are found along or near these faults, so it is postulated that they have significant control on mineralization in the district (Willden, 2006).

Hydrothermal alteration occurs throughout the district, and likely started with decalcification and jasperoid (silica) replacement; brecciation of jasperoids and additional influx of silica, arsenical pyrite, illite, and gold; late-stage quartz veining; late-stage sulfate deposition; and late-stage calcite veining (Effner, 1992). Sampling by Pilot Gold indicates that gold mineralization coincides with multi-phase jasperoid breccias with jarosite-limonite-hematite gouge (Gustin and Smith, 2016). Jasperoids are identified in all Carlin-type systems and are strongly silicified marine sediments that typically provide evidence of hydrothermal activity. In these systems, it is theorized that gold was introduced by hydrothermal fluids that percolated through a thick section of marine carbonates during Tertiary time (Nelson, 1990). As in other well-known Carlin-type systems, mineralization typically coincides with fault zones.

Although the Goldstrike district is not located the Carlin trend in Nevada, its characteristics are of a sediment-hosted gold deposit. In the Goldstrike district, controls on mineralization are stratigraphic: gold is hosted in favorable units including basal Claron and silty units of the Callville Formation; structural: mineralization typically occurs in high-angle fault zones, fault intersections, collapse breccia, and anticlinal fold hinges; in geochemical association with elevated arsenic, mercury, antimony, and thallium; and alteration: most deposits are associated with decalcification, silicification (jasperoid), clays, arsenical pyrite and arsenopyrite and their oxidized products (Gustin and Smith, 2016). In Carlin-trend deposits, it is postulated that ore fluids percolated into Fe-bearing carbonate rocks, sulfidizing and dissolving them, and precipitating pyrite, to which Au adsorbed (Muntean et al., 2011). The present study suggests a relationship between gold mineralization and an abundance of clay and iron oxide minerals. Additional geochemical analysis would need to be conducted to confirm this finding, as the current distribution of geochemical assay points is sparse in each outcrop scan.

Greenan (1992) used an infrared field spectrometer and X-Ray diffraction to conduct a study of 96 rock chip samples from the Padre Pit, an area that is located on the Goldstrike property. Silicification, iron oxidation, clay alteration, and minor propylitic alteration (indicated by the presence of minor amounts of chlorite) were identified. Illite and interlayered illite-montmorillonite were found, which indicates a temperature of formation between 150–220°C (Eslinger and Savin, 1973; Velde, 1965; Vidal et al., 2007). The presence of gold was correlated with elevated concentrations of arsenic, antimony, and mercury (Greenan, 1992).

**3.1.1.2. Bingham mining district, Utah.** Nearly three quarters of the world's Cu, half of the Mo, and one fifth of the Au, most of the Re, and minor amounts of other metals (Ag, Pd, Te, Se, Bi, Zn, and Pb) are supplied by porphyry Cu systems (Sillitoe, 2010). Porphyry ore systems are defined as large volumes of hydrothermally altered rock that are centered on a porphyry stock intrusion, and where sulfide and oxide ore minerals are precipitated from metal-rich aqueous solution at elevated temperatures (Seedorff et al., 2005; Sillitoe, 2010). Roughly concentric zonal patterns have been observed in association with porphyry deposits, and these were used as a proxy for their identification (Lowell and Guilbert, 1970). Copper porphyry mineralization is associated with certain original and alteration mineral assemblages. Identification of these minerals at outcrop scale can provide information about the different stages of alteration, which are associated with lateral and vertical zonation of a typical Copper-Gold-Molybdenum (Cu-Au-Mo) deposit. In previous studies, a workflow was applied in the laboratory setting to map minerals associated with a copper porphyry deposit (Dalm et al., 2017; Dalm

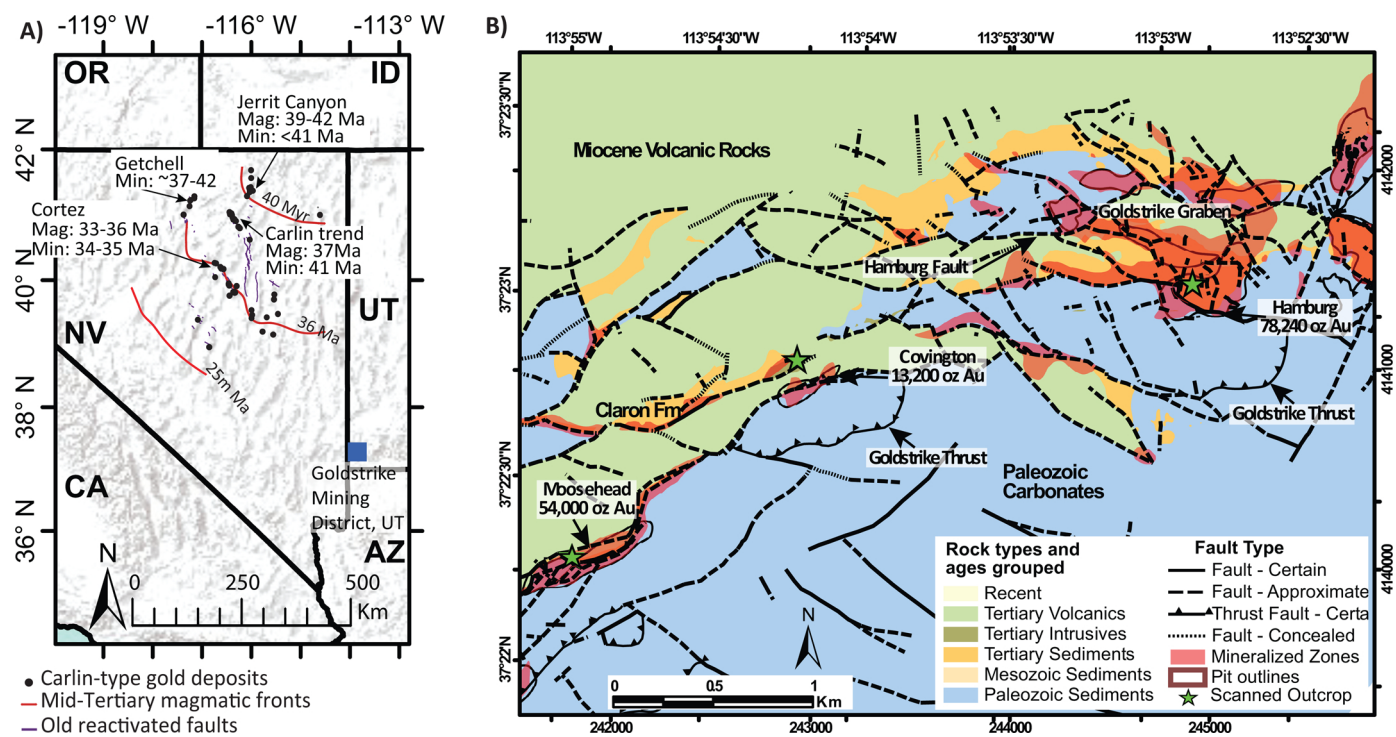


**Fig. 5.** A) Location of the Goldstrike mine in relation to Carlin-type gold deposits, including estimated ages of mineralization, modified from Muntean et al. (2011). B) Generalized geologic map of the Goldstrike area with historical production of each pit from 1988–1996 annotated (Gustin and Smith, 2016).

et al., 2014). This work seeks to apply mineral mapping at outcrop scale.

The porphyry deposit at Bingham Mine is located in the central Oquirrh Mountains, 32 km southwest of Salt Lake City, Utah and is a significant source of copper, molybdenum, gold, silver, and other ore; copper reserves are estimated to be 1400 million tons (Lanier et al., 1978; Price, 2013). At the base of the section, non-ore-bearing sedimentary rocks consist of arenaceous limestone and calcareous sandstone of the Middle Pennsylvanian Butterfield Peaks Formation and feldspathic orthoquartzite and calcareous quartzite. The overlying Upper Pennsylvanian Bingham Mine formation contains ore host limestone beds that are locally fossiliferous, silty, cherty, and argillaceous. The top of the Bingham Mine Formation contains quartzites. Igneous rocks consist of composite, hydrothermally altered and mineralized pluton, mostly quartz monzonite porphyry of Tertiary age (Lanier et al., 1978). Large, northwest-striking anticlines and synclines occur in this area. Faults, fractures, and joints are abundant and trend in the northeast direction; these have been associated with Basin and Range extension. Faults have been shown to have control on igneous intrusion and economic mineralization (Atkinson and Einaudi, 1978). This area was previously mapped by multispectral imagery: Landsat Earth Resources Technology Satellite (ERTS-1), Skylab, and RB-57 with relatively coarse spatial and spectral resolution (Anderson and Smith, 1975; Jensen and Laylander, 1975). It was also mapped using AVIRIS at 17 meter per pixel resolution (McDougal et al., 1999; Rockwell et al., 2005). Secondary mineralization is significant in formation of economic deposits, and differentiation of usually uneconomic primary mineralization from products of alteration is important for understanding mechanisms behind formation of economically viable deposits (McMillan and Panteleyev, 1980).

High vertical relief exposure of sedimentary, igneous, and metamorphic rocks and a complicated structural setting make this location of interest for a detailed ground based remote sensing study. Two areas were scanned within the mine pit (Fig. 7), and hand specimens were collected from each location and analyzed using point spectroscopy (Fig. 16) and HSI (Fig. 17).

**3.1.1.3. Asphaltic limestone quarry near Uvalde, TX.** This area is located to the east of the Maverick Basin (Fig. 8), a structurally complex, hydrocarbon-rich basin that lies within the Rio Grande Embayment, which is a broad synclinal area that separates central Texas from the Laramide fold systems in Mexico (Ewing, 2004; Wilson et al., 2011). The Balcones fault zone is the main structural feature in the area and formed during late Oligocene to early Miocene time as a result of rapid accumulation of tertiary sediments and subsidence along the Gulf Coast (Barker et al., 1994; Ewing, 2004).

The Anacacho limestone, a late-Cretaceous high-energy carbonate deposit, is typically found along the flanks of volcanic mounds (Brownlow, 1992). It consists of coarse-grained fossiliferous carbonate strata interbedded with thin beds of volcanic ash (bentonite) (Waechter et al., 1977). Asphalt fills pore spaces and is mined for production of road-paving aggregate. Limestones with high and low asphalt concentrations are mined in unison, to achieve an optimal asphalt concentration for road paving materials. The emplacement of asphalt is inferred to be a result of migration of immature hydrocarbons through faults and fractures, with impermeable volcanic ash beds acting as a seal (Wilson et al., 2011). Cretaceous-aged dikes, sills, laccoliths, and shallow intrusions are abundant in the area, mostly of mafic composition, including olivine, nephelinite, basanite, alkali basalt, and phonolite (Ewing, 2004; Spencer, 1969). Most igneous rocks are altered to smectite clays and zeolites (Brownlow, 1992).

### 3.1.2. Data collection

Hyperspectral images were acquired using sensors from Spectral Imaging Ltd. (Specim), Finland. Two sensors were used, one of which operates in the VNIR and the other in the SWIR regions of the electromagnetic spectrum. The VNIR sensor collects data within a spectral range of 400–1000 nm with a possibility of 840 spectral bands and a spatial dimension of 1600 pixels. Spatial resolution is a function of distance from the surface being imaged, as well as focal length and pixel pitch of the sensors that are used. Cameras were mounted to a rotating stage that is held by a tripod (Fig. 9). The cameras operate in a push-broom fashion, with the rotation axis parallel to their optical axis.

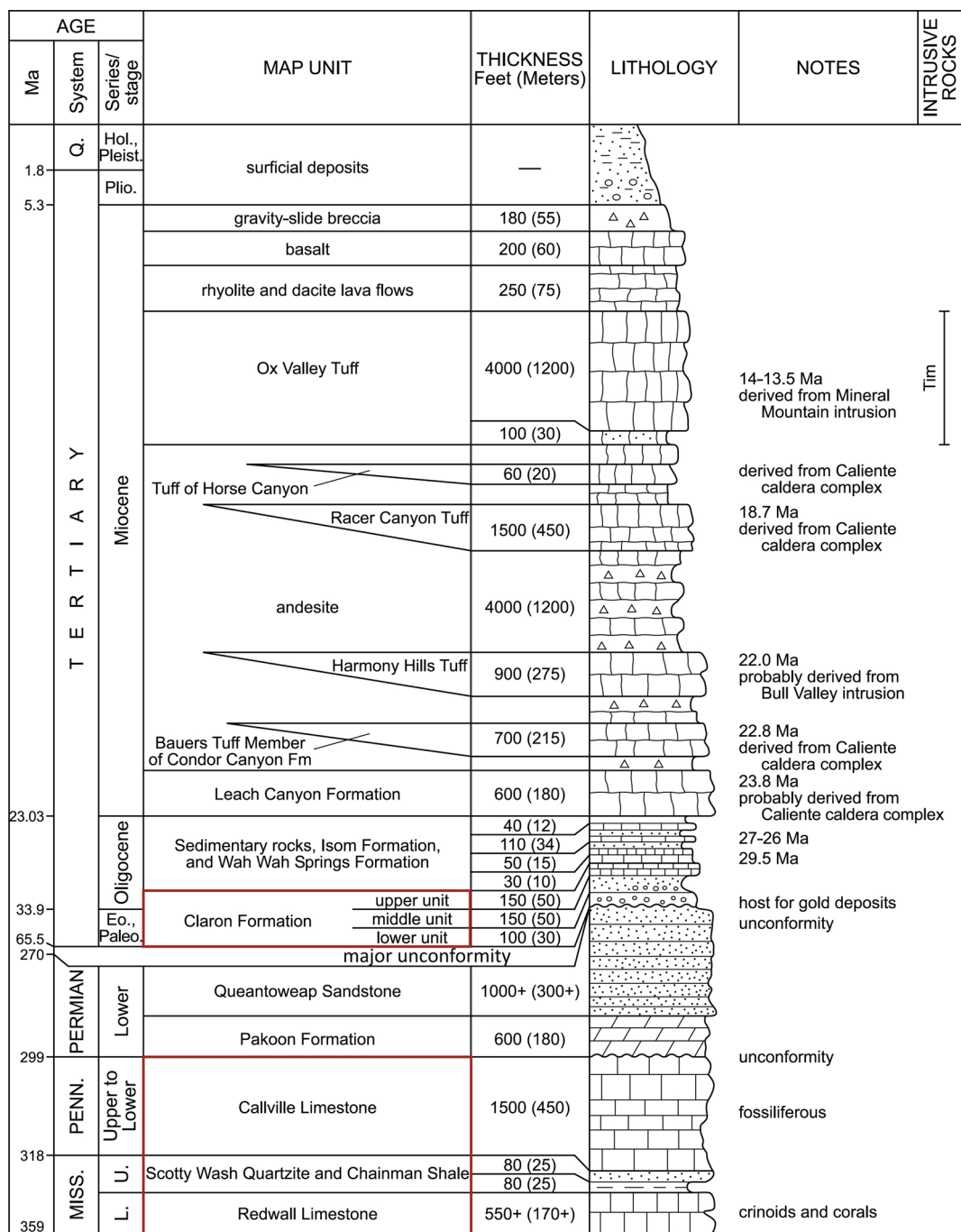


**Fig. 6.** Stratigraphic column of the Goldstrike area modified from Rowley et al. (2007). Units that are exposed in scanned sections are outlined.

Outcrop data were collected following the procedure outlined in Okyay et al. (2016). During data collection, a white reference panel made from polytetrafluoroethylene (PTFE) similar to Spectralon® and a dark (~3%) calibration panel (both with measured reflectance spectra) were placed in front of the outcrop for calibration purposes. Exposure (integration time) was adjusted so that pixels with highest albedo are not oversaturated. Following data collection, dark reference images were collected with the same integration time as the scan for dark current subtraction.

Laboratory HSI of specimens was conducted, with hyperspectral sensors mounted to a wall and samples placed on a scanning stage that moves at a constant linear speed, following the methodology described in (Krupnik et al., 2016). Point spectroscopy was collected in the lab,

using a FieldSpec Pro spectroradiometer from Analytical Spectral Devices, Inc. (ASD).

### 3.1.3. Pre-processing

In the field, dark current frames were collected with lens caps covering the sensors. An average dark current frame was calculated and subtracted from frames of each image. To convert to relative reflectance, EL calibration was performed (Smith and Milton, 1999). Image pixels from dark and white reference panels with known reflectance (measured using an ASD spectrometer) were used for fitting a regression line through these two targets, which have large spectral contrast. Spectral bands that are affected by atmospheric absorption were excluded from further analysis. To correct for brightness gradients

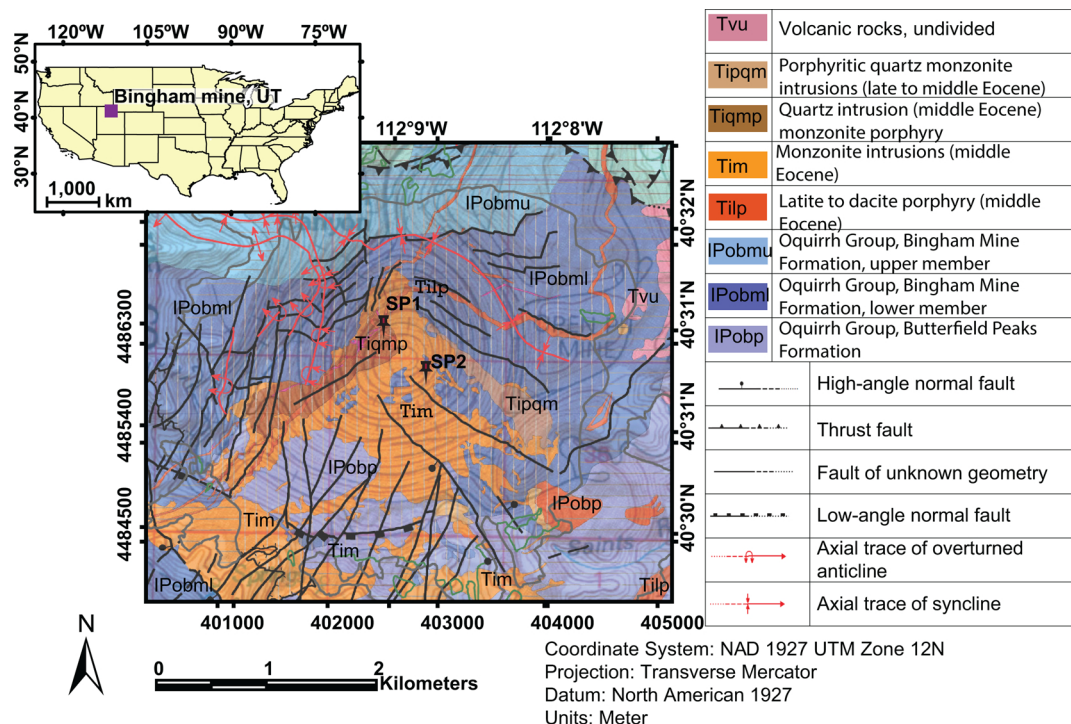


Fig. 7. Scan locations in the Bingham mine, superimposed on a geologic map, modified after Clark et al. (2015).

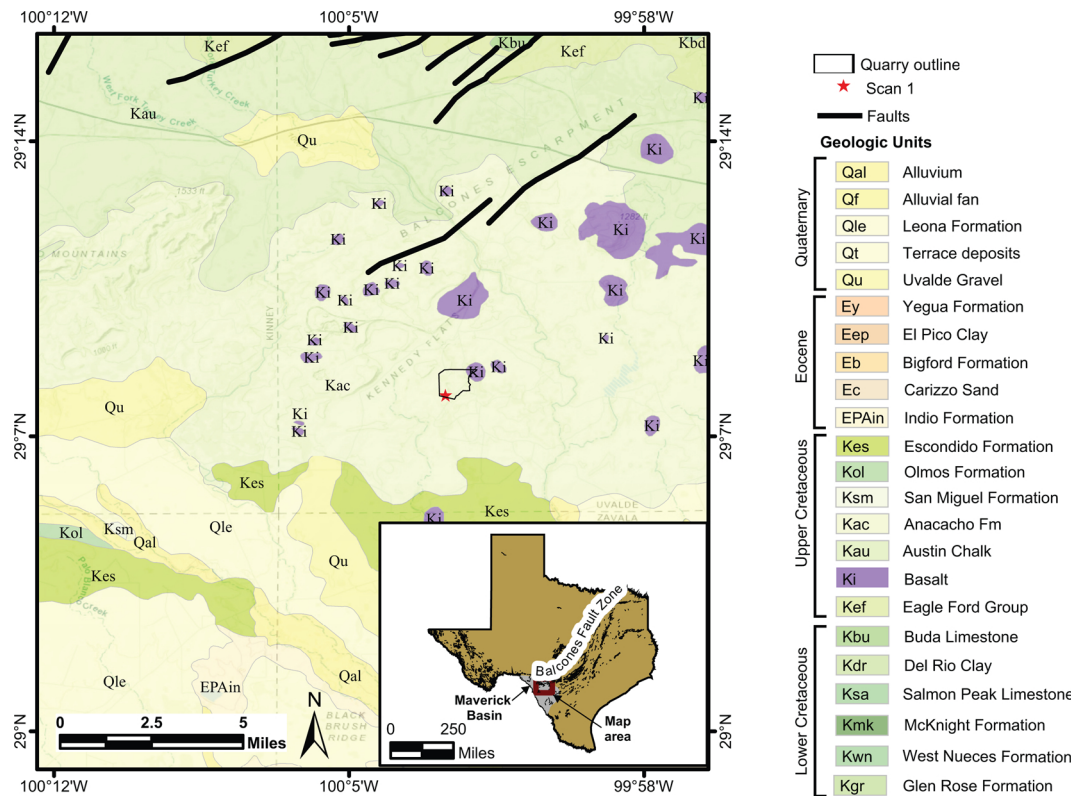


Fig. 8. Geologic map showing quarry outlines and scanned areas after Barnes et al. (1992); Wilson et al. (2011). The Anacacho limestone (Kac) is the focus of this study.

in the image, cross-track illumination correction (Schiefer et al., 2006) was applied using a first-order polynomial. To remove striping and noise that typically occurs in SWIR imagery, a forward MNF transformation was applied, data were subset to only spatially coherent bands, and a Fourier Transform was used to isolate and filter stripes in the

frequency domain (Pande-Chhetri and Abd-Elrahman, 2013). Lastly, an inverse MNF transform was applied (Green et al., 1988). Spectral smoothing was done using second order polynomial Savitsky-Golay filtering with a width of four bands (Bromba and Ziegler, 1981; Savitzky and Golay, 1964). To achieve spectral continuity throughout

the VNIR and SWIR domains, images were registered using tie points that were selected manually; RMS errors of registration ranged from 0.61 to 0.95 pixels. Afterward, pixels that correspond to sky, vegetation, oversaturated pixels, and shadows were masked.

### 3.1.4. Classification/spectral mapping

Iron oxides and hydroxides such as hematite and goethite, respectively, have distinct absorption features in the VNIR wavelengths. Due to crystal field transition, goethite has asymmetrical absorptions at 480 and 670 nm (Crowley et al., 2003). Hematite has an absorption at about 550 nm due to charge transfer, and a weaker crystal absorption near 670 nm (Crowley et al., 2003). Clays and carbonates have distinct absorption features in the SWIR domain due to vibrational processes in the Al-O-H bonds and the planar  $\text{CO}_3^{2-}$  ions (Clark, 1999). Absorption feature characteristics were derived from the data in three spectral regions: 435–610 nm, 2121–2260 nm, and 2196–2397 nm for observing iron oxides, clays, and carbonates, respectively. These spectral regions were isolated and continuum removal was applied to compare absorption features from a common baseline (Clark and King, 1987). Depths of spectral absorptions and locations of deepest absorptions were computed using an extension for ENVI 5.1, which derives the locations and depths of spectral absorptions based on a continuum-removed input, using trend analysis to detect saddle points (local maxima), and a user-defined number of minima, or absorptions between these saddle points (Kopačková and Koucká, 2014; Kopačková and Koucká, 2017).

Due to inaccessibility to the outcrops (as a result of issues with permission in active operations, height of the rock walls and safety concerns, etc.), sampling was limited to float near the base of rock walls, so relatively pure endmembers were extracted from image pixels using pixel purity index on spatially coherent MNF bands. They were then selected using n-D Visualizer, a tool within ENVI that is used to identify and locate and cluster the pixels with the most spectrally extreme response. Endmember regions were compared to laboratory spectra collected using the ASD spectroradiometer, as well as spectral library curves published by USGS (Clark et al., 2007).

To classify the data, two methods were used. SVM (Wu et al., 2004) is a supervised classification method that was built on statistical learning theory. It separates classes using a decision surface, called a hyperplane, between user-defined classes. Multi-range Spectral Feature Fitting (SFF) compares a user-defined absorption feature from each image pixel to that of a known spectrum, using a least-squares fit (Clark et al., 1990a). Ranges were defined at shoulders of absorption features, and continuum removal (CR) (Clark and King, 1987) was applied to endmember and image spectra before SFF classification.



**Fig. 9.** Field photograph showing the camera setup at the Goldstrike mining district, UT. VNIR and SWIR sensors are mounted on a rotating stage for data collection.

## 3.2. Results and discussion

### 3.2.1. Goldstrike mining district

In addition to SFF and SVM classification, absorption feature characteristics were derived from the data in three spectral regions: 435–610 nm, 2121–2260 nm, and 2196–2397 nm for observing iron oxides, clays, and carbonates, respectively. These spectral regions were isolated and continuum removal was applied to compare absorption features from a common baseline (Clark and King, 1987). Spectral curves of endmember samples are shown in Fig. 10.

Outcrops at three locations were examined within the Goldstrike district: the Hamburg open pit mine (Fig. 11), a road cut near the Covington mine where a Tertiary igneous intrusion is exposed (Fig. 12), and an outcrop in the Moosehead mine (Fig. 13). True color images for each scan and spectral maps and classifications follow.

**3.2.1.1. Hamburg open-pit mine.** The scan taken in the Hamburg open pit mine, positioned at  $37^{\circ}23'4.52''\text{N}$  and  $113^{\circ}52'49.46''\text{W}$  (Fig. 11) captures the Hamburg fault scarp. This fault has reverse geometry but normal offset, resulting from multiple phases of deformation. Paleozoic units (Callville limestone, Scotty Wash Quartzite, Chainman Shale, and Redwall Limestone) are thrust against the Eocene Claron Formation (Fig. 11A). A whitish clay (rhyolite intrusive) is seen in proximity to the fault. Minimum Al-OH absorption of Chainman Shale and Scotty Wash Quartzite is located at a longer wavelength (2209–2221 nm) than younger rocks (Callville Limestone), with Claron Formation showing this absorption at shortest wavelengths in the sequence (2190–2200 nm). A transect across Paleozoic units shows this decrease in the absorption location (Fig. 11C). In the Callville Formation, clays appear more abundant with increased proximity to the fault zone. Claron red beds are bleached near the fault, as evidenced by reduced absorptions related to iron oxides.

In the Hamburg mine, iron oxides and clays are abundant along the Hamburg fault line and along permeable contacts between bedding planes (Fig. 11B). This also is indicative of pathways for hydrothermal fluids that deposited alteration minerals. A shift in the Al-OH absorption feature to shorter wavelengths in the Claron and Callville Formations, versus longer wavelengths in exposures of the Chainman Shale and Scotty Wash Quartzite (Fig. 11C) was observed. Spatial variation in the Al-OH band wavelength (2190–2220) of micaceous phase clays (muscovite, illite) could be of interest, because relationships between these endmembers and occurrence of gold deposits have been studied in hydrothermally altered systems (Kokaly et al., 2016; Wang et al., 2017; Yang et al., 2011). White mica that has an absorption at longer wavelengths could suggest substitution of iron or magnesium for aluminum (Clark, 1999; Duke, 1994). To confirm that this phenomenon is the cause of variability of this absorption feature in the Goldstrike district, sample geochemistry would have to be confirmed. Conversely, a shift to longer wavelengths could be a result of mixture with other minerals, such as chlorite. No apparent variability in clay composition (spectral absorption location) is present in scans that contain units that are younger than Callville (Pennsylvanian).

**3.2.1.2. Road cut near Covington open pit mine.** In the roadcut scan near the Covington pit, the scan position was located at approximately  $37^{\circ}22'49.40''\text{N}$  and  $113^{\circ}54'12.25''\text{W}$ . Tertiary intrusive rocks are exposed, with some caliche formation, as well as minor calcite veining was also observed. A small amount of jarosite is in the northwestern portion of the scan (Fig. 12). Calcite veins (few centimeter thickness) occur in the center of the scanned area. The highest gold concentrations are associated with iron oxidation and clay alteration of a gabbro dike in the northwest portion of the scan.

In the Covington road cut, a tertiary igneous intrusion was imaged. Caliche concretions near the top of the outcrop result in a strong calcite signal at the top of the section (Fig. 12 C and D). Caliches typically form in an arid environment when alternating precipitation patterns lead to

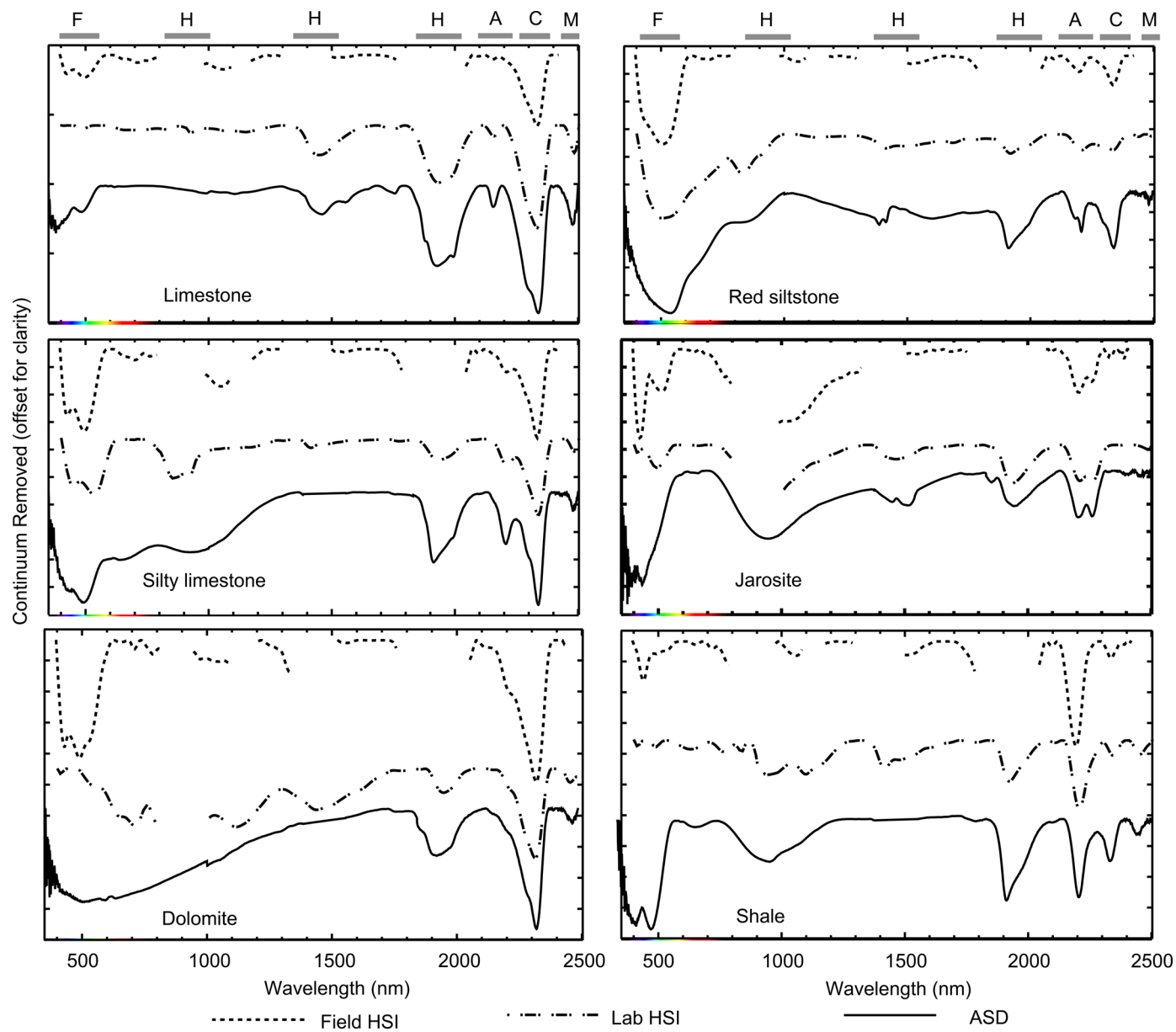
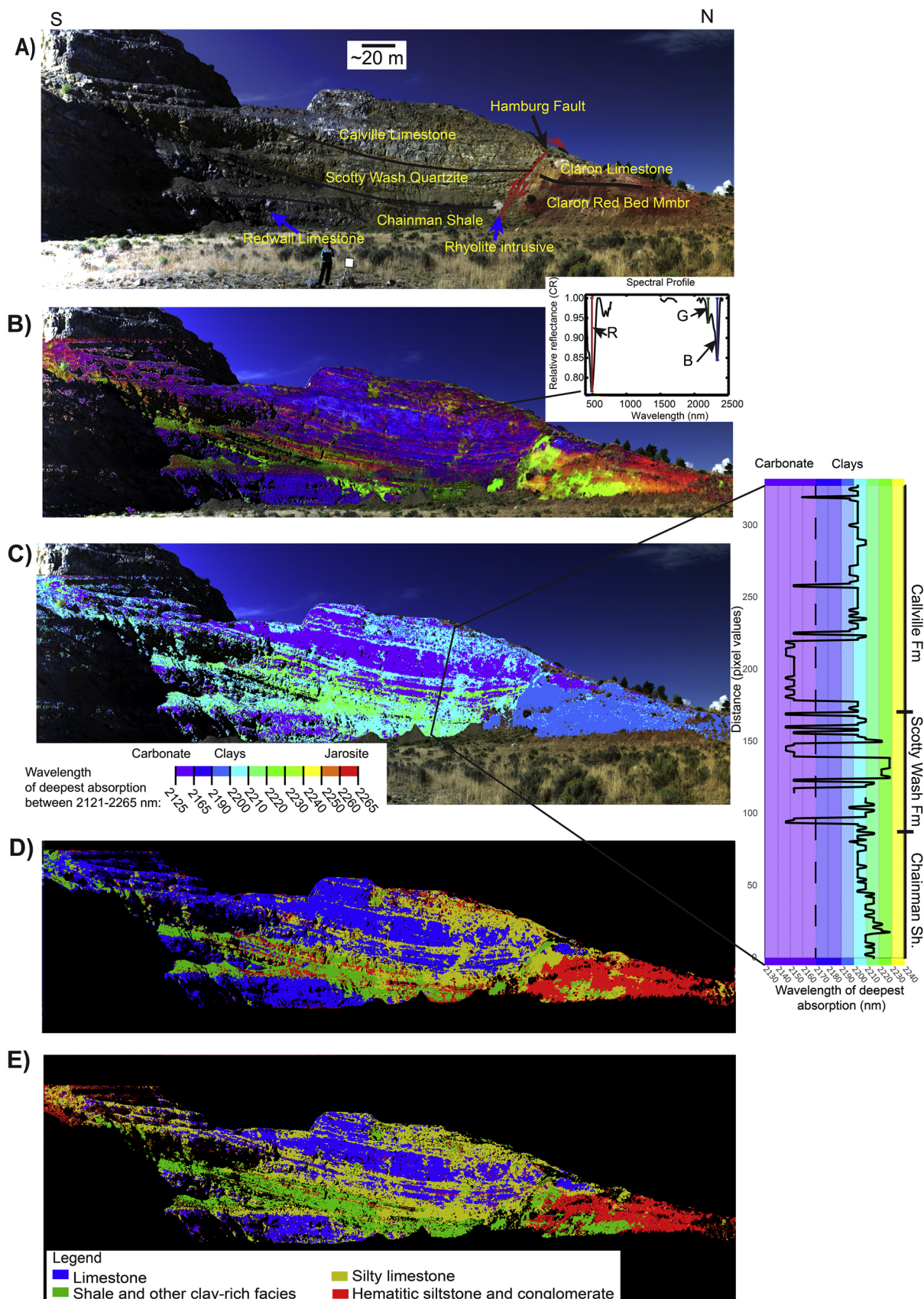


**Fig. 10.** Spectral signatures of endmembers used to classify imagery in the Hamburg mine, roadcut near Covington open pit, and Moosehead mine. Field HSI is derived from outcrop data, lab HSI from samples scanned indoors, and ASD spectra. F = iron oxide features, H =  $\text{H}_2\text{O}$  absorption, A = Al-OH feature, C =  $\text{CO}_3^{2-}$  feature, and M = Mg-OH feature.

soil saturation and desiccation. Solution occurs as meteoric waters saturated with calcium carbonate travel downward during a wet period, and precipitation occurs as capillary rise of these alkaline waters during a dry period (Bretz and Horberg, 1949). Calcite veins radiate downward from the caliches (Fig. 12 C), suggesting deposition of calcite by meteoric waters percolating through void spaces, which may have formed because of desiccation. A surface expression of Jarosite is more abundant in the Covington outcrop than others included in this study. In acidic, sulfate-rich environments, jarosite is formed by oxidation of sulfides such as pyrite (Baron and Palmer, 1996).

**3.2.1.3. Moosehead open-pit mine.** In the Moosehead mine, a scan was positioned at  $37^{\circ}22'14.44''\text{N}$  and  $113^{\circ}55'2.10''\text{W}$ . Callville Limestone is in a fault-bounded contact with Eocene volcanics (west of where the image was collected). Nearly vertical-to-overturned bedding of the Callville Limestone is inferred to be a result of fault-propagation folding (Willden, 2006). The Callville Limestone shows massive-to-thin beds

interbedded with more permeable, gold-bearing siltstones, which are decalcified and replaced by clays (illite). These near-vertical horizons are a likely conduit for fluids that were enriched in Au and other metals. Within the Callville Formation, two phases of silicification are observed: grey silicified rocks were shattered and are barren, whereas the reddish siltstone layers have higher concentrations of gold (not seen in the image). Dolomitization exists along the edges of limestone beds. Deformation toward the southwestern portion of the scan coincides with argillization and minor dolomitization. Iron oxide minerals coat southwest-dipping fractured areas. Offset can be seen along siltstone beds that are rich in iron oxide (shown by arrows in Fig. 13 B). A similar sense of offset can be seen in limestone beds (Fig. 13 C) that are dolomitized near their center, with decreasing dolomitization toward their edges. Although siltstone is dominant in beds that are between the limestones, the deepest absorption occurs in the carbonate spectral region (2320–2340), likely because of mixtures of clays and carbonates, or carbonate dust coating the outcrop surface. For this reason, the band



(caption on next page)

**Fig. 11.** Hamburg pit (looking west). Exposure of Hamburg fault, which has normal offset but reverse geometry. The northern block has downward motion, and reverse geometry is likely due to rotation of the Hamburg fault because of its location in the hanging wall of the Hassayampa fault. A) True color image with annotation showing the Paleozoic units in contact with the Claron formation. An arrow is shown to symbolize rotation of the Hassayampa fault, causing reverse geometry. B) Outcrop map showing the depths of the absorptions corresponding to iron-oxide, (435–610 nm), Al-OH (2121–2260 nm), and carbonate (2196–2397 nm) in RGB. Spectral map of rock exposure is overlaid on a true color image. C) Spectral map showing the location of the deepest absorption in the range of 2121–2270 nm. A transect across the stratigraphic section is shown with wavelengths of the deepest spectral absorption. Classified images using D) SVM and E) SFF. The legend applies to both D and E.

depth image (Fig. 13 B) is more informative due to the enhanced visibility of carbonate and clay mixtures in this color combination (yellowish-green).

In the Moosehead mine scans, nearly vertical beds of Callville limestone are affected by multiple phases of alteration and deformation that is visible at multiple scales. Southwest-dipping fractures cut beds of limestone and iron oxide (Fig. 13 B), and dolomitized limestones (Fig. 13 C). The southwest-oriented Covington Hill fault runs through the Moosehead open pit mine roughly parallel to the scanned outcrop exposure (Fig. 13). Displacement along these fractures can be seen (Fig. 13B) and is consistent with upward displacement of the Callville Limestone by the Covington Hill fault.

**3.2.1.4. Hand specimens.** Imaged samples from each area provide ground truth for remote sensing data and a more in-depth view of alteration patterns (Fig. 14). Samples from the Hassayampa fault zone are composed of mostly clays with absorptions ranging between 2200–2210 nm and iron oxides. Samples from the Hamburg mine are mostly from lower levels of the outcrop due to lack of accessibility to higher levels of the vertical rock face. Silicified rocks that were collected near the fault zone contain clays and jarosite, and the lower Claron conglomerate, which contains clay and limestone clasts in a matrix composed of iron oxide, clays, and carbonates. Samples C1 and C3 from the Covington roadcut are intrusive (gabbro), so its original composition is difficult to constrain in VNIR and SWIR wavelengths, although alteration minerals can be distinguished (clays and iron oxides). Sample C2 is a carbonate, likely a result of caliche formation. Samples from the Moosehead mine are mostly carbonates with significant clay and iron oxide alteration, most notably samples M2 and M5. M2 is a silicified limestone with an abundance of iron oxide. Silicification causes weak (low depth) absorptions in the carbonate and clay wavelengths in the SWIR domain, whereas the surrounding area contains a mixture of clays, carbonates, and iron oxides, with the iron oxide absorption having the greatest depth. Sample M5 is a limestone that shows bands of concentrated iron oxides. Limestone with concentric iron oxide bands (Fig. 14) also referred to as Liesegang rings, which are formed by rhythmic segregation of iron oxide minerals.

### 3.2.2. Bingham copper porphyry deposit

In a typical porphyry copper system, the main ore zone is related to the boundary between potassic and phyllitic hydrothermal alteration (Seedorff et al., 2005). Delineation of hydrothermal alteration zones can be a guide to ore, with the assumption of minimal telescoping i.e. overprinting of older alteration zones by younger ones (Sillitoe, 2010). Several types of alteration were observed and associated minerals were mapped based on their spectral features (Figs. 15–19). Altered quartzites, quartz monzonite, and latite intrusions are present in the study area. Propylitic and potassic alteration are the earliest in this deposit, whereas phyllitic and intermediate argillic alteration are superimposed on the former alteration types.

Intermediate argillic alteration is known to form during the transition from deeper level potassic alteration to shallow epithermal and hot spring environments. Potassium metasomatism, possibly accompanied by leaching of calcium and sodium in rocks containing original aluminosilicate minerals may be the source of potassic alteration, which would introduce orthoclase, biotite, and quartz. Development of new calcium and magnesium minerals by rearrangement of original rock-

forming components characterizes propylitic alteration, which results in chlorite, epidote, and calcite minerals from alteration of mafic minerals such as plagioclase. Leaching of sodium, calcium, and magnesium from alumino-silicate-bearing rocks produces phyllitic or sericitic alteration, with original feldspar as the source of potassium. Comprehensive replacement of rock-forming silicates by sericite or muscovite-like minerals, and quartz may occur in phyllitic alteration, typically resulting in destruction of original textures. Introduction of new clay minerals in silicate rocks by acidic hydrothermal fluids is referred to as argillic alteration (Beane and Titley, 1981).

### 3.2.3. Asphaltic limestone quarry near Uvalde, TX

An outcrop of the upper Cretaceous Anacacho Limestone was scanned in the Black Spur Mine located approximately 21 miles southwest of Uvalde, Texas. The Anacacho limestone was scanned at 29° 7.975'N; 100° 2.711'W. Endmembers for classification were limestone, bentonite, and bitumen (Fig. 20). Scans of the Anacacho formation revealed spatial patterns of bitumen and bentonite in relation to limestone host rock (Fig. 21). Asphalt accumulations appear discontinuous, are parallel to bedding in some locations, and have some spatial association with volcanic ash beds.

## 3.3. Findings of case studies

Three case studies are presented, which applied close-range imaging spectroscopy for outcrop characterization in mine and quarry settings. A Carlin-style gold deposit showed variability of carbonates, clays, iron oxides, and jarosite and their relationship with gold concentrations obtained by geochemical assays. A porphyry copper-gold-molybdenum deposit was studied to delineate various hydrothermal alteration zones based on mineral assemblages. Two limestone quarries were studied to assess the spatial distributions of various building materials, with one example in an actively developed asphaltic limestone exposure, and another example in an abandoned limestone quarry.

Ground-based HSI was conducted along three fault zones and one igneous intrusion in the Goldstrike mining district: the Hamburg mine, where Paleozoic units are in a fault bounded contact with the Tertiary Claron formation, a tertiary igneous intrusion along a road cut near the Covington mine, and a deformed Paleozoic unit (Callville Limestone) in the Moosehead mine. Other than the roadcut near the Covington mine, each scan was taken at a fault zone, allowing for multiple phases of deformation and alteration to be observed. Spectral mapping was conducted by spectral feature fitting and mapping the minimum wavelength locations and depths of diagnostic absorption features of iron oxides in VNIR wavelengths, and carbonates and clays in SWIR wavelengths. Spectral feature mapping allowed for visualization of mineral mixtures so that details in mineral variation could be observed, such as offset along fractures in the Moosehead mine. Mapping the position of the absorption located around 2190–2220 nm (Al-OH) was useful for the Hamburg mine, as observations of variability in this feature may suggest variations in Al abundance, or possibly a mixture with other minerals such as Chlorite. In the road cut near the Covington mine, mapping absorption features allowed for delineation of caliche deposits and associated calcite veins, and iron oxidation of an igneous intrusion (gabbro). In the Moosehead mine, mapping the location of the minimum absorption in SWIR wavelengths was suitable for delineating dolomitization, and mapping abundances of iron oxides, clays, and

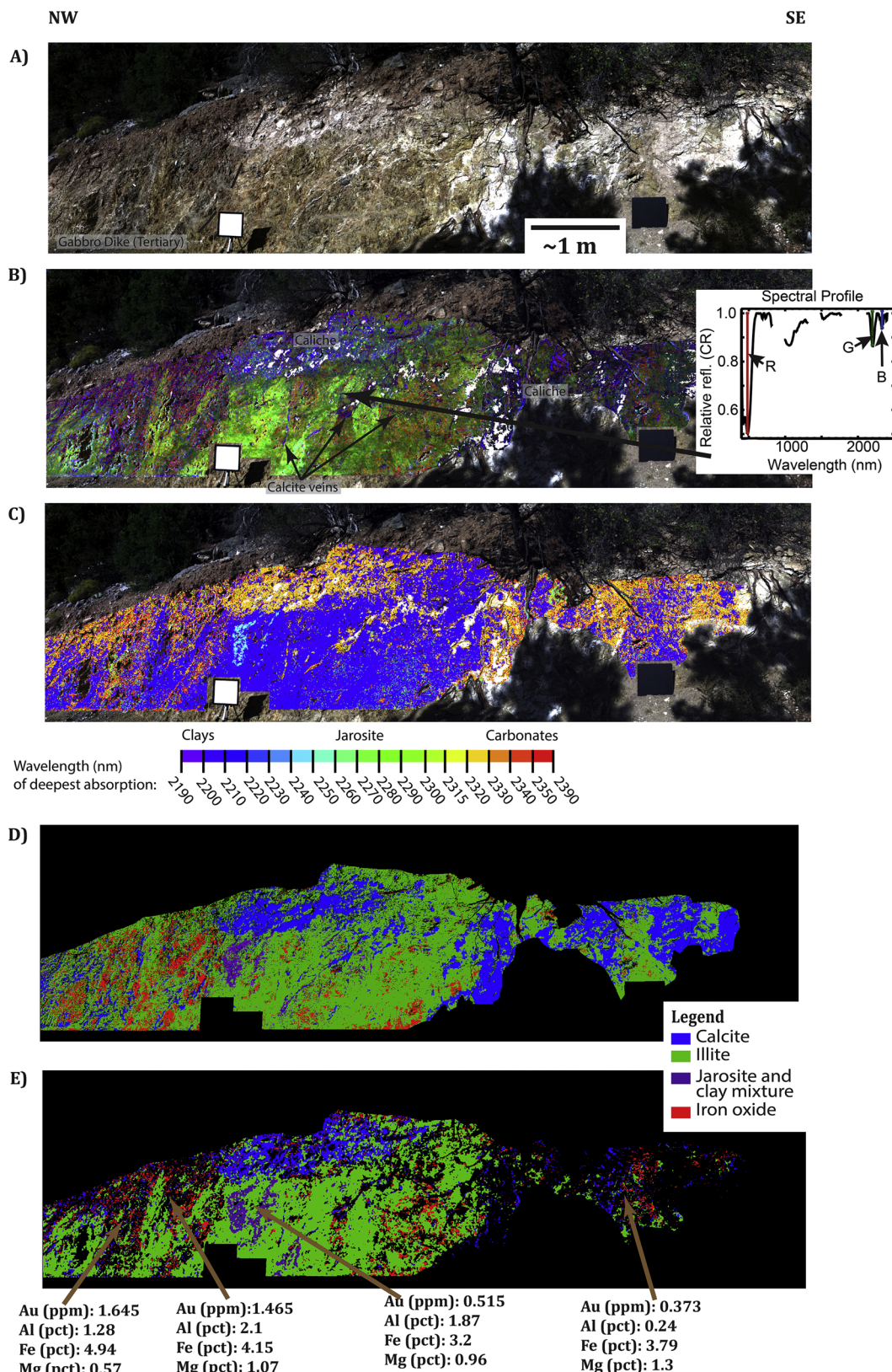


**Fig. 12.** Road cut scan near the Covington open pit mine. A) True color image B) Spectral map showing the position of the minimum wavelength at deepest absorption (2100–2350 nm), stretched for depth. The spectral map overlay on a true color image. C) Location of deepest absorption located between 2121 and 2397 nm. D) SVM and E) SFF classification showing clay and carbonate mixtures, calcite, and jarosite endmembers. Geochemical data are shown with approximate location of the samples taken. Data courtesy of Liberty Gold.

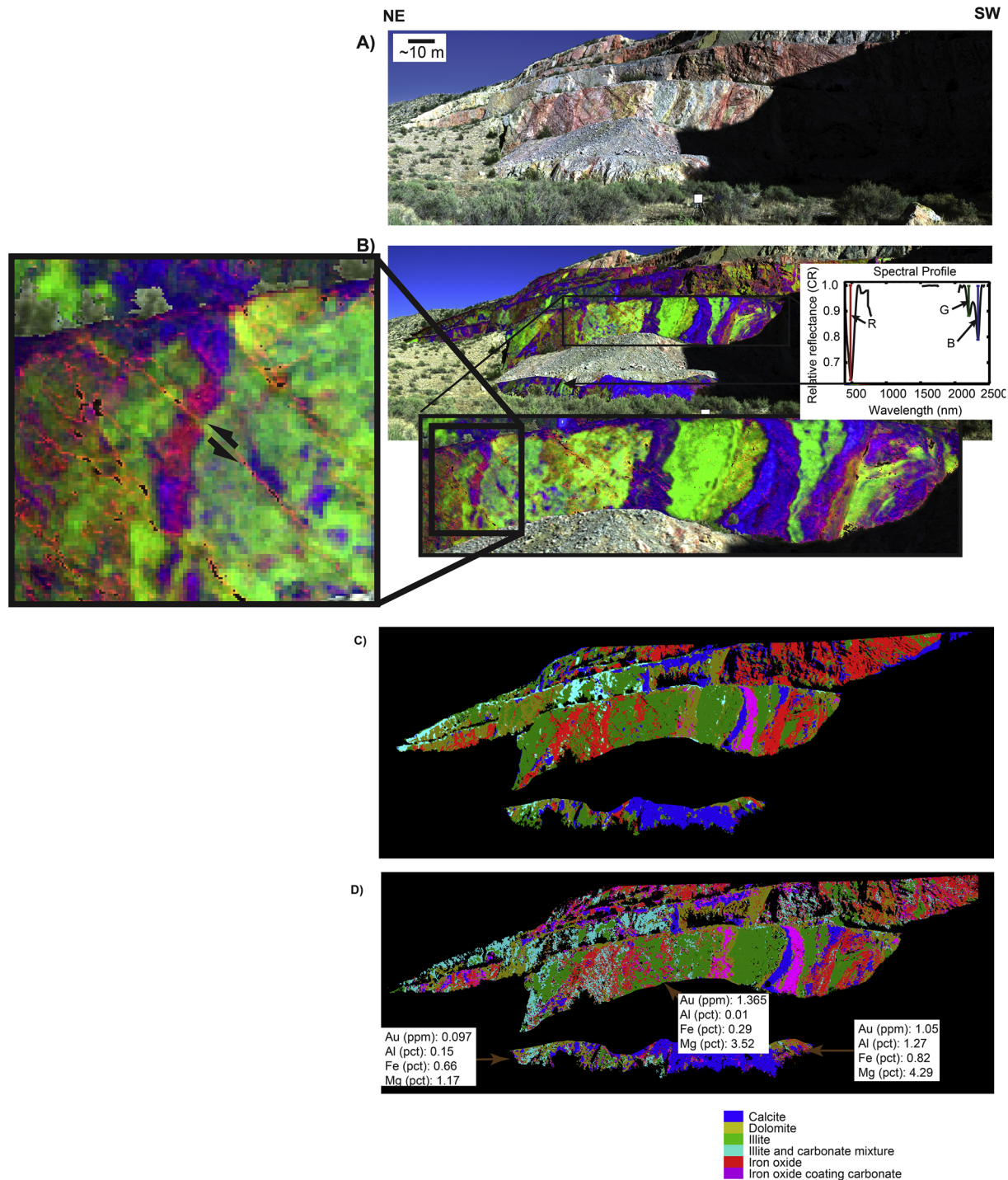


**Fig. 13.** Moosehead pit looking southeast. A) True color image with annotation showing the Paleozoic rocks in contact with the Paleocene Clarion formation. B) Outcrop map showing the depths of an iron-oxide absorption (435–610 nm), the Al-OH absorption (2121–2260 nm), and the Carbonate absorption (2196–2397 nm) in RGB. Classified rock exposure overlay on a true color image. Inset maps show a zoomed-in view of spectral mapping. C) SVM and D) SFF classification results. Geochemical data are shown with approximate location of the samples taken. Data courtesy of Liberty Gold.

carbonates throughout the VNIR and SWIR spectrum allowed for observation of deformed and offset bedding planes along fracture traces.

In the porphyry Cu-Au-Mo deposit, the delineation of hydrothermal alteration zones shows potential for use in early stage exploration. With

prior knowledge of the deposit type, mineral assemblages used to map zones of potassic and phyllitic alteration could be a proxy for locating the ore zone, which is postulated to be located at the boundary between these areas (Lowell and Guilbert, 1970), although most systems are

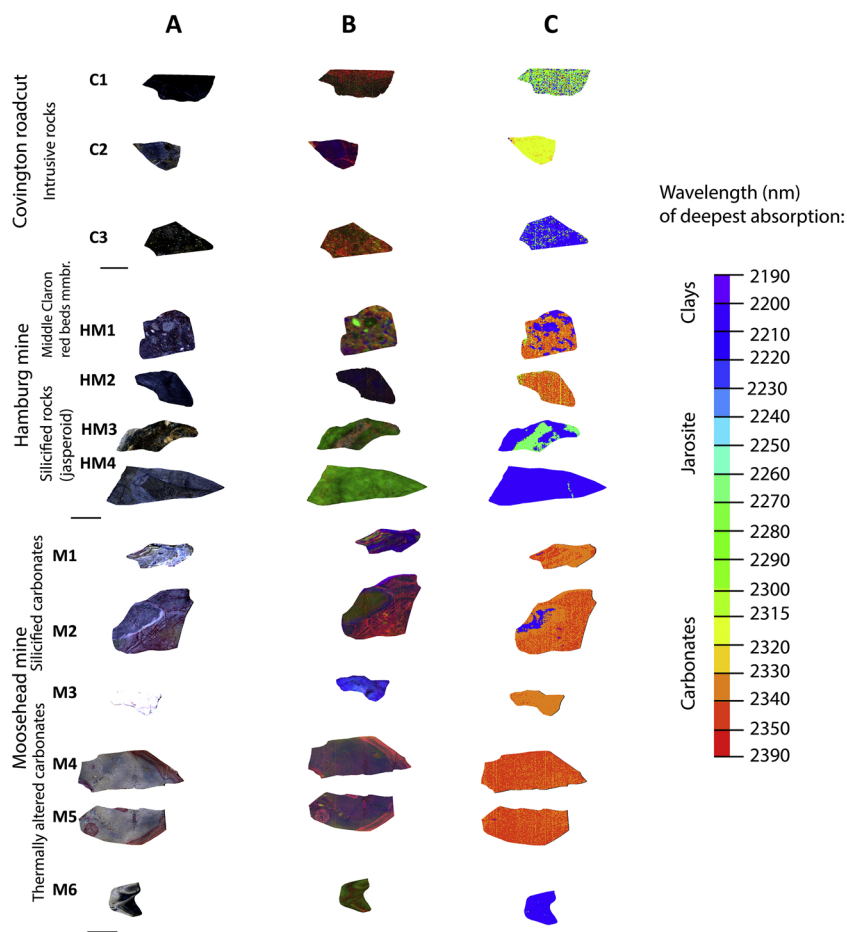


**Fig. 14.** Samples collected from each scan area in A) True color, B) RGB composite showing depths of an iron-oxide absorption (435–610 nm), Al-OH absorption (2121–2260 nm), and Carbonate absorption (2196–2397 nm), C) Spectral map showing the location of the deepest absorption between 2121 and 2390 nm.

more complex due to telescoping, or overprinting of older alteration zones by younger ones (Sillitoe, 2010).

Applications of ground-based HSI to limestone extraction could include identification of intervals with desirable composition. For example, when road-paving aggregate is produced, specific proportions of limestone, asphalt, and basalt would be targeted for optimal consistency. Imaging of the Anacacho Limestone at the quarry near Uvalde, Texas reveals distribution of limestone, bitumen, and volcanic ash beds (Fig. 21). Asphalt is seen in association with fractures, as noted by Wilson et al. (2011), and also parallel to bedding surfaces in some locations (Fig. 21B). This could suggest that asphalt migrated through fractures and was introduced into weak, porous beds.

#### 4. Challenges, future work

HSI is useful for quantifying surface materials, however, recent surface alteration can be a limitation when original mineralogy is the focus of investigation. The effect of lichen encrustation was investigated in the laboratory, and a lichen index was developed (Salehi et al., 2017), then applied at outcrop scale (Salehi, 2018). A similar index for other types of surface weathering would be desirable, if original minerals are the focus of study. If surface moisture of the rock varies, water absorption features at 1400 and 1900 nm could mask

characteristic mineral absorptions, such as smectite clay, carbonate, gypsum, and rare earth oxides such as samarium oxide (Clark, 1999). Moisture can also decrease reflectance throughout the spectrum. If moisture content differs along a rock exposure, direct mineralogic or lithologic comparison to other areas may be limited. This issue is mentioned in (Kurz et al., 2012; Ragona et al., 2004). Conversely, moisture might be a focus of study, such as water content in oil sands (Entezari et al., 2016) or measuring soil moisture (Haijun et al., 2017).

The lack of prominent spectral features in some sulfides makes reliable and consistent prediction of their abundance a challenge. Some ratios were employed, for example, Feng et al. (2006), who used band expressions in TIR wavelengths. Sulfides were classified against ultramafic host rock by Bolin and Moon (2003), who set up the groundwork for a sulfide identification algorithm. The technique used by Bolin and Moon (2003), SAM classification, might not be repeatable in other host rock or mineral assemblages with minerals that have similar spectral characteristics, and furthermore, the authors mention that modifications would be needed to implement this technique within an automated system.

In VNIR and SWIR wavelengths, some silicate minerals such as quartz and feldspars cannot be distinguished with confidence. Diagnostic absorptions of silica are present in TIR wavelengths, with a strong asymmetric stretch located at approximately 9000–10 000 nm

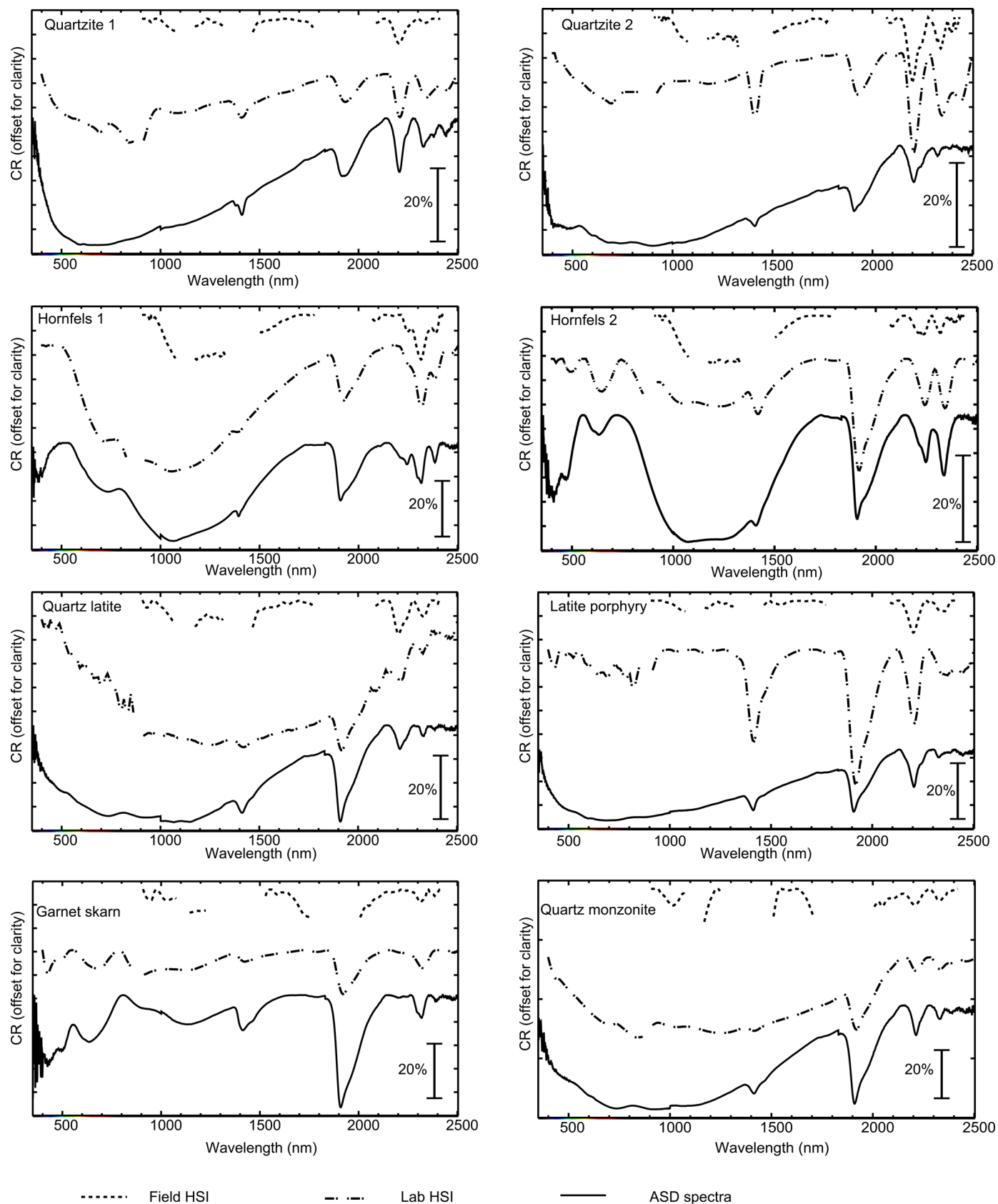


**Fig. 15.** Reflectance spectra derived from point spectroscopy (ASD), laboratory HSI, and field HSI.

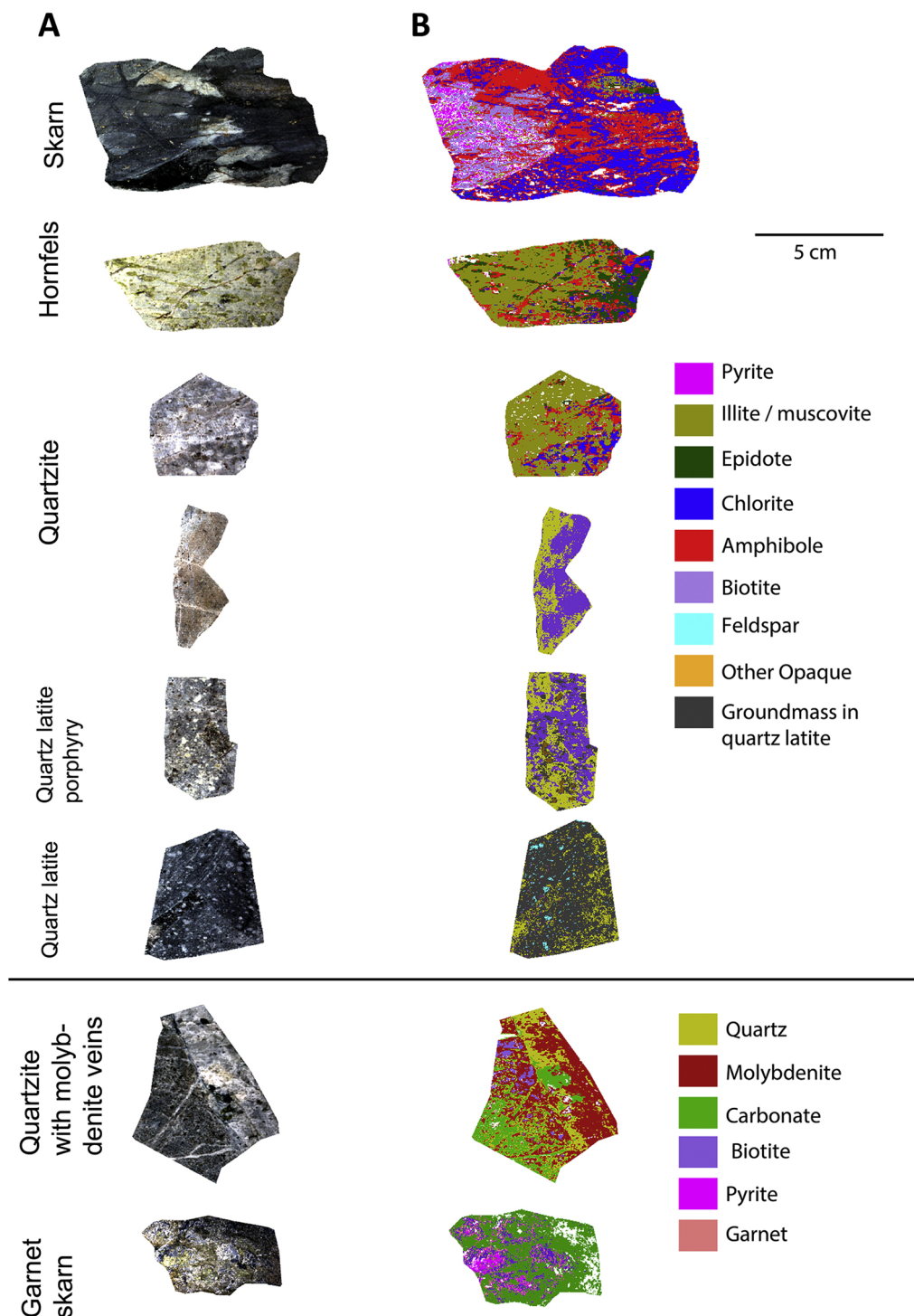
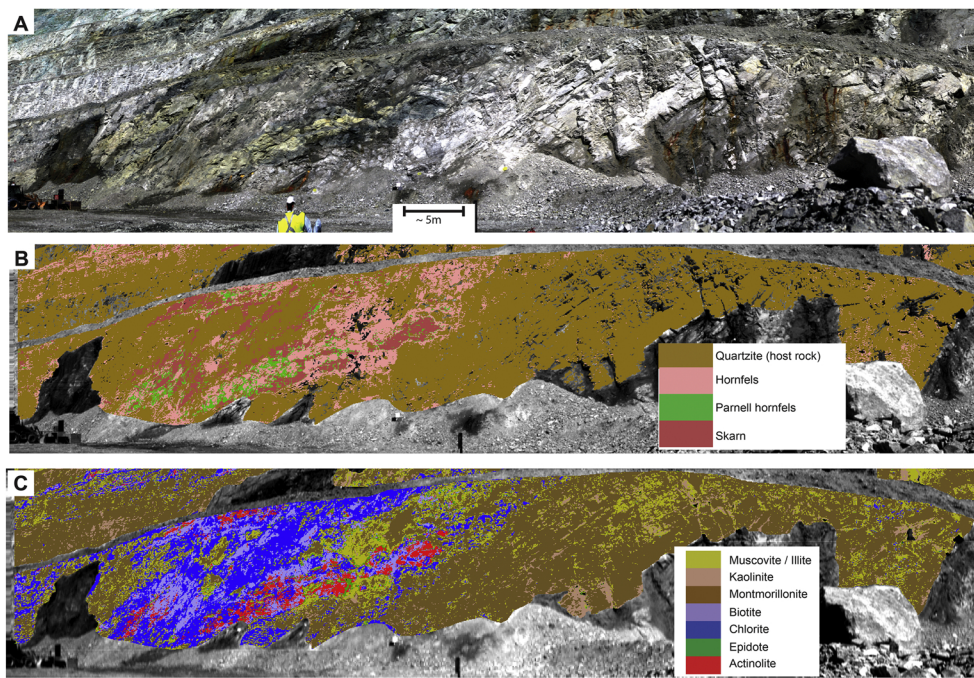


Fig. 16. Scanned hand specimens in A) true color and B) classified using SVM.

(Clark, 1999). This suggests a need for imaging in TIR wavelengths for constraint of silicified alteration zones, such as jasperoids in sediment-hosted gold deposits. Ground-based imaging in the long-wave infrared domain is still in the early stages of development, mostly used in the laboratory setting (Holma et al., 2012a; Holma et al., 2012; Kuosmanen et al., 2015; Tappert et al., 2015), and recently several field studies

have been conducted (Boutanga-Tombet et al., 2018; Kirsch et al., 2018; Yousefi et al., 2018; Zheng et al., 2014). It is likely that HSI in the TIR spectral range will be used more frequently in future years, and its application will become more widespread, also to gas detection and monitoring studies.

While some hyperspectral camera manufacturers offer spectral



**Fig. 17.** An area where propylitic alteration minerals (Clays, biotite, white mica, and epidote) are observed in the data. A) Approximate true color image in VNIR wavelengths B) SFF classification based on lithology, with a grayscale image at the 2334 nm wavelength in the background. Endmembers were collected in the laboratory setting using an ASD spectroradiometer. C) SVM classification based on mineralogy, superimposed on grayscale image in the 2334 nm wavelength. Endmembers were derived from image pixels and compared to USGS spectral libraries.

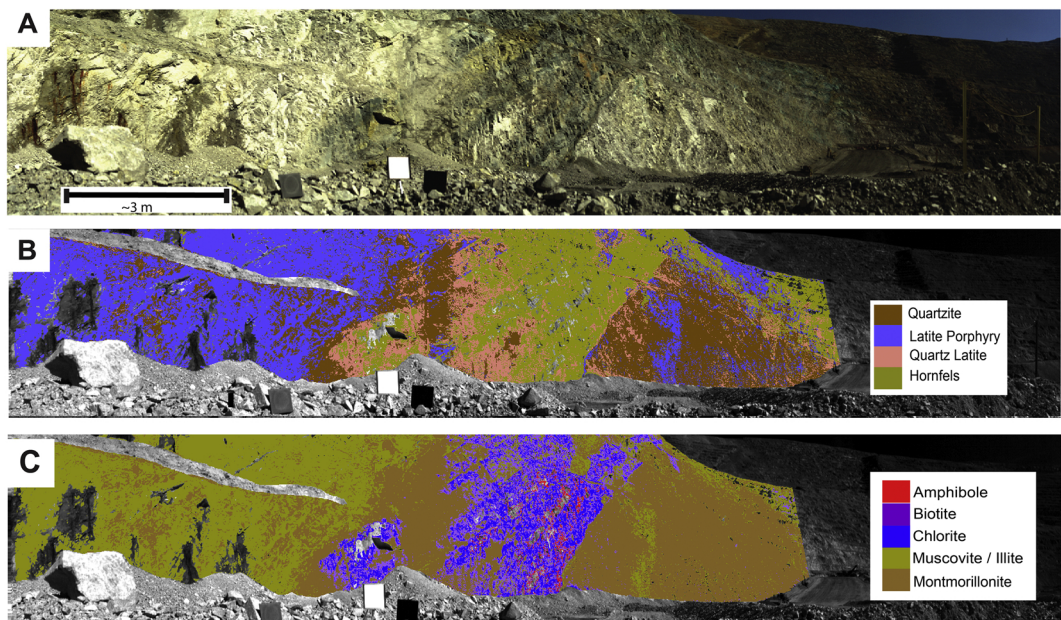


**Fig. 18.** This area contains propylitic or phyllitic alteration minerals (clays, biotite, white mica, and minor amounts of chlorite). A) Approximate true color image in VNIR wavelengths B) SFF classification based on lithology, with a grayscale image at 2334 nm wavelength in the background. Endmembers for classification were collected from the rock face and imaged in the laboratory setting using an ASD spectroradiometer. C) SVM classification based on mineralogy, superimposed on grayscale image in the 2334 nm wavelength.

continuity throughout visible, near infrared, and SWIR wavelengths, some require the use of separate cameras in VNIR and SWIR ranges due to different detector types and sensitivity ranges. Okyay and Khan (2018) addressed this issue by applying corrections to VNIR data for spectral concatenation with SWIR data. In some instances, higher

sensitivity of a VNIR sensor in longer wavelengths makes this correction less necessary, as shown in some studies (Murphy et al., 2012; Murphy et al., 2014b; Murphy et al., 2016).

Integration with topographic data requires separate instruments for data collection, and additional processing time is needed to ensure

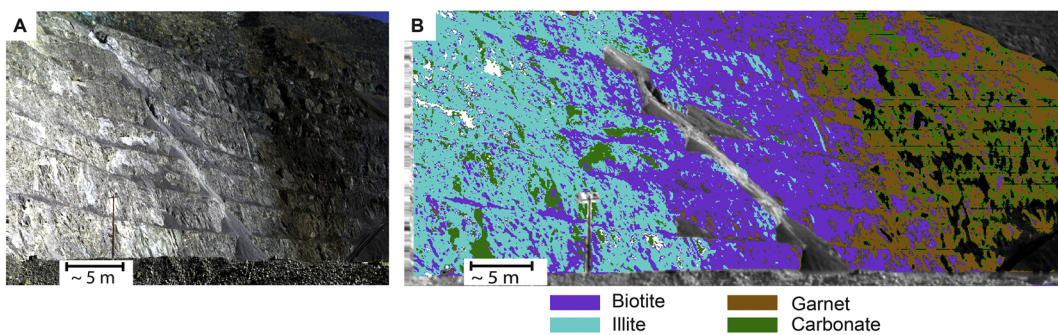


**Fig. 19.** Imagery collected from an area that contains potassic alteration minerals (strong biotite, amphibole, white mica, and some carbonates). Minor amounts of garnet are seen). A) Approximate true color VNIR image, B) SVM classification result.

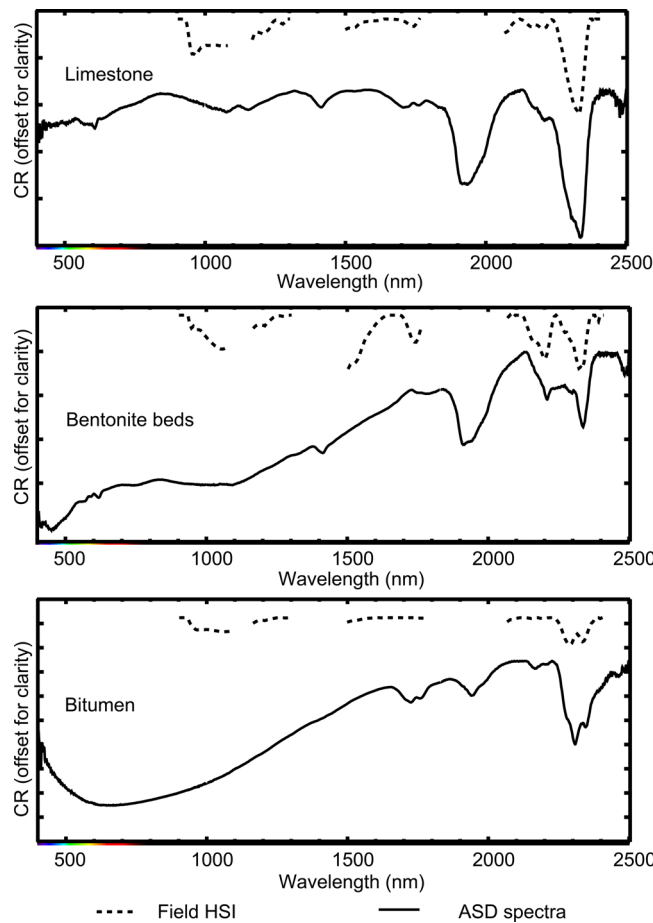


**Fig. 20.** Reflectance spectra of samples and representative endmembers in field data.

accurate registration. Development of a single instrument that will collect both topographic and spectral data is underway: full waveform hyperspectral LiDAR has been used to study vegetation (Hakala et al., 2012), biochemical properties (Lin and Jiang, 2018), and ore classification (Chen et al., 2018). Limitations of currently available hyperspectral LiDAR systems are the use of few bands. For example, Chen et al. (2018) discuss 17 spectral channels from 450 to 1600 nm and a limited range of scanning due to a low pulse energy. Spatial range

limitations are likely the reason why hyperspectral LiDAR studies are typically conducted in the laboratory setting (Malkamäki et al., 2018).

Drone-mounted HSI can bridge the observation gap between ground-based and airborne measurements. Several studies have been conducted, including for monitoring of acid mine drainage (Jackisch et al., 2017; Jackisch et al., 2018), mapping REE deposits (Booyse et al., 2018) and hydrothermal alteration (Kirsch et al., 2018). A pre-processing toolbox was developed by Jakob et al. (2017) for orthorectification, georeferencing, topographic and radiometric correction, and reflectance conversion.

Another technique that is likely to be used commonly is mapping rock microstructure at high resolution. van Ruitenbeek et al. (2019) developed a methodology for differentiating crystal shapes using compactness and convexity of shapes, degree of sorting in sedimentary rocks, grain orientation, layering and banding, and even distinction between sedimentary and volcanic microstructures using a SWIR camera with an OLESMacro lens at 26 μm resolution under artificial illumination.

## 5. Conclusion

This work reviewed recent geoscience applications of ground-based HSI, specifically related to mining. A recent increase in publications suggests the potential of this technology to be applied to discovery of new deposits, and possibly addition of this method to active operations, to automate the workflow. The ability of this technique to study surface mineralogy of vertical rock faces that are physically inaccessible would reduce the physical hazards inherent to geological studies. Some recent publications investigate the potential use of hyperspectral sensors in automated mining operations, deep sea mapping under artificial illumination, and detection of fugitive gas emissions. Three additional case studies are presented that apply close-range VNIR and SWIR HSI to study economic deposits in mines and quarries, including a sediment-hosted gold deposit, a porphyry Cu-Au-Mo mine, and a bituminous limestone quarry. In the sediment-hosted gold deposit, spectral mapping was achieved by spectral feature fitting, support vector machine classification, and mapping of minimum wavelength locations and depths of diagnostic absorption features of iron oxides in VNIR wavelengths, and carbonates and clays in SWIR wavelengths. Wavelength mapping allowed for visualization of mineral mixtures so that details in compositional variation could be observed, such as offset of bedding planes along fractures. In the Cu-Au-Mo deposit, mineral zonation associated with different phases of alteration were mapped at several locations. In the bituminous limestone quarry, patterns of bitumen deposits were

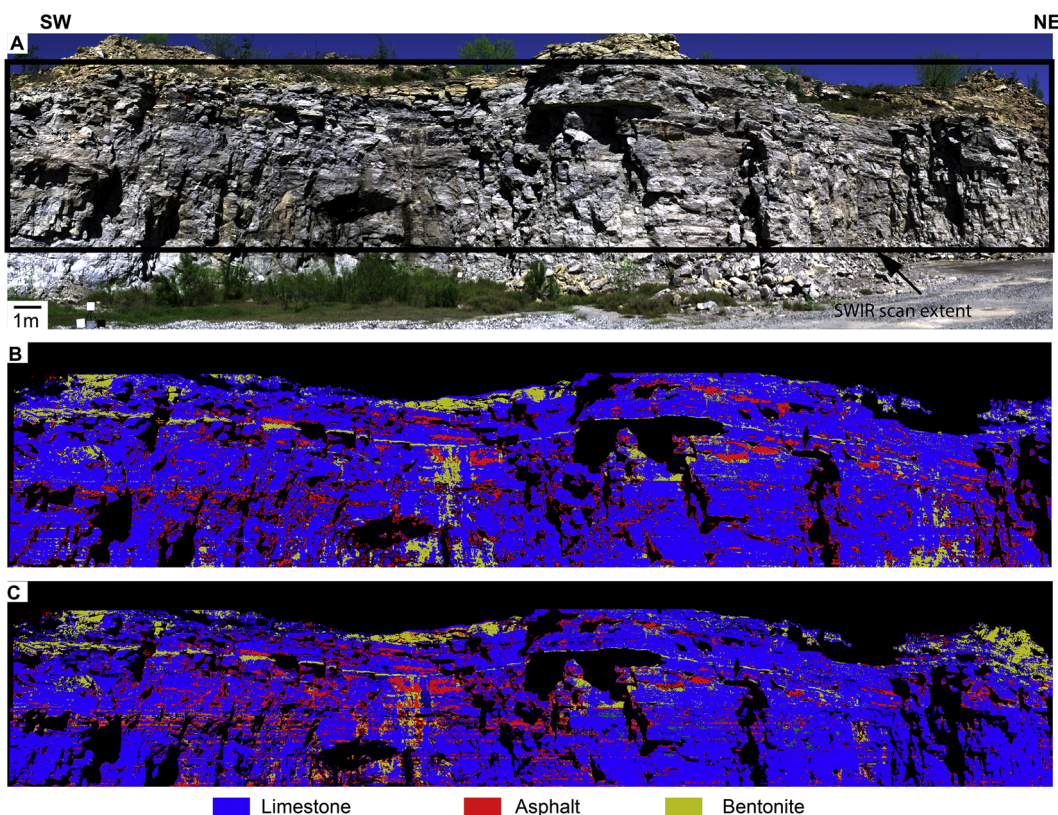


**Fig. 21.** Scan of the Anacacho limestone where bituminous intervals are found: A) True color (VNIR) composite; B) SVM and C) SFF classification derived from SWIR imagery.

observed and raise further questions about their geologic setting. As further contributions are added, it is likely that there will be progress in mitigating the effects of surface alteration, faster and more efficient integration with topographic data, and more widespread use for mineral exploration, automation, and environmental monitoring.

## Acknowledgements

Hyperspectral cameras that were used in this study were purchased through the National Science Foundation Award number 1256202. We are grateful to Rio Tinto Kennecott for allowing field work at the Bingham mine, and for help with the field survey. Peter Shabestari is acknowledged for his helpful guidance in the field, and Pilot Gold (USA) Inc. (a subsidiary of Liberty Gold) are thanked for providing map data for the Goldstrike mining district. Our gratitude goes out to Lei Sun and Macey Crockett for help with field work. We also would like to thank Editor Arturo Gomez-Tuena and two anonymous reviewers for very helpful suggestions to improve this manuscript.

## References

- Achata, E.M., Inguglia, E.S., Esquerre, C.A., Tiwari, B.K., O'Donnell, C.P., 2019. Evaluation of Vis-NIR hyperspectral imaging as a process analytical tool to classify brined pork samples and predict brining salt concentration. *J. Food Eng.* 246, 134–140. <https://doi.org/10.1016/j.jfoodeng.2018.10.022>.
- Adair, D.H., 1986. Structural Setting of the Goldstrike District Washington County, Utah Geological Association Publication, Utah, pp. 129–135.
- Aguilar, P.L., Plaza, A., Martínez Cobo, P., Perez, R., 2000. Endmember Extraction by a Self-Organizing Neural Network on Hyperspectral Images.
- Alonso de Linaje, V., Khan, S., 2017. Mapping of diagenetic processes in sandstones using imaging spectroscopy: a case study of the Utrillas Formation, Burgos, Spain. *Sedimentary Geol.* 353, 114. <https://doi.org/10.1016/j.sedgeo.2017.03.010>.
- Alonso de Linaje, V., Khan, S., Bhattacharya, J., 2018. Study of carbonate concretions using imaging spectroscopy in the Frontier Formation, Wyoming. *Int. J. Appl. Earth Obs. Geoinformation* 66, 82–92. <https://doi.org/10.1016/j.jag.2017.11.010>.
- Anderson, A., Smith, A., 1975. Geological Applications of LANDSAT-1 Imagery to the Great Salt Lake Area.
- Arne, D., House, E., Pontual, S., Huntington, J., 2016. Hyperspectral interpretation of selected drill cores from orogenic gold deposits in central Victoria, Australia. *Aust. J. Earth Sci.* 63 (8), 1003–1025. <https://doi.org/10.1080/08120099.2016.1223171>.
- Asadzadeh, S., de Souza Filho, C.R., 2017. Spectral remote sensing for onshore seepage characterization: A critical overview. *Earth-Sci. Rev.* 168, 48–72. <https://doi.org/10.1016/j.earscirev.2017.03.004>.
- Askari, M.S., O'Rourke, S., Holden, N.M., 2013. A comparison of the prediction accuracy for soil organic carbon measured by point and imaging spectroscopy. *Biosyst. Eng. Res. Rev.* 18, 139–142.
- Atapour, H., Aftabi, A., 2007. The geochemistry of gossans associated with Sarcheshmeh porphyry copper deposit, Rafsanjan, Kerman, Iran: Implications for exploration and the environment. *J. Geochem. Explor.* 93 (1), 47–65. <https://doi.org/10.1016/j.gexplo.2006.07.007>.
- Atkinson, W., Einaudi, M.T., 1978. Skarn formation and mineralization in the contact aureole at Carr Fork, Bingham, Utah. *Econ. Geol.* 73 (7), 1326–1365.
- Axen, G.J., Taylor, W.J., Bartley, J.M., 1993. Space-time patterns and tectonic controls of Tertiary extension and magmatism in the Great Basin of the western United States. *GSA Bulletin* 105 (1), 56–76. [https://doi.org/10.1130/0016-7606\(1993\)105<0056:STPATC>2.3.CO;2](https://doi.org/10.1130/0016-7606(1993)105<0056:STPATC>2.3.CO;2).
- Barker, R.A., Bush, P.W., Baker, E.T., 1994. Geologic history and hydrogeologic setting of the Edwards-Trinity aquifer system, west-central Texas. US Department of the Interior, US Geological Survey.
- Barnes, V.E., Hartmann, B.M., Scranton, D.F., 1992. Geologic map of Texas. In: Bureau of Economic Geology. University of Texas at Austin.
- Baron, D., Palmer, C.D., 1996. Solubility of jarosite at 4–35 °C. *Geochim. Cosmochim. Acta* 60 (2), 185–195. [https://doi.org/10.1016/0016-7037\(95\)00392-4](https://doi.org/10.1016/0016-7037(95)00392-4).
- Beane, R.E., Titley, S.R., 1981. Porphyry copper deposits. Part II. Hydrothermal alteration and mineralization. *Economic Geology* 75th Anniversary 235–269.
- Bedini, E., 2011. Mineral mapping in the Kap Simpson complex, central East Greenland, using HyMap and ASTER remote sensing data. *Adv. Space Res.* 47 (1), 60–73. <https://doi.org/10.1016/j.asr.2010.08.021>.
- Bigham, J.M., Schwertmann, U., Pfab, G., 1996. Influence of pH on mineral speciation in a bioreactor simulating acid mine drainage. *Appl. Geochem.* 11 (6), 845–849. [https://doi.org/10.1016/S0883-2277\(96\)00052-2](https://doi.org/10.1016/S0883-2277(96)00052-2).
- Boesche, N.K., Rogas, C., Mielke, C., Kaufmann, H., 2014. Hyperspectral digital image analysis and geochemical analysis of a rare earth elements mineralized intrusive complex (fen carbonatite complex in Telemark region, Norway). In: Z. B., K. M. and R. R. (Ed.), EARSeL 34th Symposium, (Warsaw, Poland).
- Boesche, N., Rogass, C., Lubitz, C., Brell, M., Herrmann, S., Mielke, C., Tonn, S., Appelt, O., Altenberger, U., Kaufmann, H., 2015. Hyperspectral REE (Rare Earth Element) mapping of outcrops—applications for neodymium detection. *Remote. Sens.* 7 (5), 5160. <https://doi.org/10.3390/rs70505160>.

- Boesche, N.K., Rogass, C., Christian, M., Lubitz, C., Brell, M., Herrmann, S., Körting, F., Papenfuß, A., Tonn, S., Altenberger, U., Guanter, L., 2016. Rare earth element detection from near-field to space - samarium detection using the REEMAP algorithm. *IEEE International Geoscience and Remote Sensing Symposium, Beijing, China* 5414–5417.
- Bolin, B.J., Moon, T.S., 2003. Sulfide detection in drill core from the Stillwater Complex using visible/near-infrared imaging spectroscopy. *Geophysics* 68 (5), 1561–1568. <https://doi.org/10.1190/1.1620630>.
- Booyens, R., Zimmermann, R., Lorenz, S., Glaaguen, R., Nex, P., 2018. Multi-source hyperspectral imaging of carbonatite-hosted REE-Nb-Ta mineralization at Marinkas Quellen, Namibia.
- Boutanga-Tombet, S., Huot, A., Vitins, I., Heuberger, S., Veuve, C., Eisele, A., Newsom, R., Guyot, E., Marcotte, F., Chamberland, M., 2018. Thermal Infrared Hyperspectral Imaging for Mineralogy Mapping of a Mine Face. pp. 1–15 1518.
- Bretz, J.H., Horberg, L., 1949. Caliche in Southeastern New Mexico. *J. Geol.* 57 (5), 491–511.
- Bromba, M.U.A., Ziegler, H., 1981. Application hints for Savitzky-Golay digital smoothing filters. *Anal. Chem.* 53 (11), 1583–1586. <https://doi.org/10.1021/ac00234a011>.
- Brossard, M., Marion, R., Carrére, V., 2016. Deconvolution of SWIR reflectance spectra for automatic mineral identification in hyperspectral imaging. *Remote Sens. Lett.* 7 (6), 581–590. <https://doi.org/10.1080/2150704x.2016.1168946>.
- Brownlow, D.T., 1992. *The Geology of the Anacacho Limestone and the Evaluation of Its Asphalt Resources*. Texas Tech University, Uvalde County, Texas.
- Buckley, S.J., Kurz, T.H., Schneider, D., 2012. The benefits of terrestrial laser scanning and hyperspectral data fusion products. *ISPRS Int. Arch. Photogramm., Remote Sens. Spat. Inf. Sci.* XXXIX-B7, 541–546. <https://doi.org/10.5194/isprarchives-XXXIX-B7-541-2012>.
- Buddenbaum, H., Steffens, M., 2012. The effects of spectral pretreatments on chemometric analyses of soil profiles using laboratory imaging spectroscopy. *Appl. Environ. Soil Sci.* 2012, 1–12. <https://doi.org/10.1155/2012/274903>.
- Buddenbaum, H., Steffens, M., 2012b. Mapping the distribution of chemical properties in soil profiles using laboratory imaging spectroscopy, SVM and PLS regression. *EARSel eProceedings* 11 (1), 25–32.
- Burud, I., Moni, C., Flo, A., Futsaether, C., Steffens, M., Rasse, D.P., 2016. Qualitative and quantitative mapping of biochar in a soil profile using hyperspectral imaging. *Soil Tillage Res.* 155, 523–531. <https://doi.org/10.1016/j.still.2015.06.020>.
- Calderón, F.J., Mikha, M.M., Vigil, M.F., Nielsen, D.C., Benjamin, J.G., Reeves, J.B., 2011. Diffuse-reflectance mid-infrared spectral properties of soils under alternative crop rotations in a semi-arid climate. *Commun. Soil Sc. Plant Anal.* 42 (17), 2143–2159. <https://doi.org/10.1080/00103624.2011.596243>.
- Calin, M.A., Parasca, S.V., Savastri, D., Manea, D., 2013. Hyperspectral imaging in the medical field: present and future. *Appl. Spectrosc. Rev.* 49 (6), 435–447. <https://doi.org/10.1080/05704928.2013.838678>.
- Chamberland, M., Farley, V., Vallières, A., Villemaire, A., Belhumeur, L., Giroux, J., Legault, J.-F., 2005. High-performance field-portable imaging radiometric spectrometer technology for hyperspectral imaging applications. *Chemical and Biological Sensors for Industrial and Environmental Security*. *Int. Soc. Optic. Photon.* 5994, 59940N1–59940N11.
- Chaudhary, S., Ninsawat, S., Nakamura, T., 2018. Non-destructive trace detection of explosives using pushbroom scanning hyperspectral imaging system. *Sensors (Basel)* 19 (1). <https://doi.org/10.3390/s19010097>.
- Chen, Y., Jiang, C., Hyypä, J., Qiu, S., Wang, Z., Tian, M., Li, W., Puttonen, E., Zhou, H., Feng, Z., Bo, Y., Wen, Z., 2018. Feasibility study of ore classification using active hyperspectral LiDAR. *IEEE Geosci. Remote Sens. Lett.* 15 (11), 1785–1789. <https://doi.org/10.1109/LGRS.2018.2854358>.
- Chilingaryan, A., Melkumyan, A., Murphy, R.J., Schneider, S., 2015. Automated multi-class classification of remotely sensed hyperspectral imagery via gaussian processes with a non-stationary covariance function. *Math. Geosci.* 48 (5), 537–558. <https://doi.org/10.1007/s11004-015-9622-x>.
- Clark, R.N., 1999. Spectroscopy of rocks and minerals, and principles of spectroscopy. In: Renz, A.N. (Ed.), *Manual of Remote Sensing*. John Wiley and Sons, Inc, New York, pp. 3–58.
- Clark, R.N., King, T.V., 1987. Automatic Continuum Analysis of Reflectance Spectra.
- Clark, R.N., Gallagher, A.J., Swarz, G.A., 1990a. Material absorption band depth mapping of imaging spectrometer data using a complete band shape least-squares fit with library reference spectra. In: *Proceedings of the Second Airborne Visible/Infrared Imaging Spectrometer (AVIRIS) Workshop*. JPL Publication 90-54. pp. 176–186.
- Clark, R.N., Swarz, G.A., Wise, R., Livo, E., Hoefen, T., Koklay, R.F., Sutley, S.J., 2007. USGS digital spectral library splib06a. USGS (Editor). Digital Data Series 231.
- Clark, R.N., King, T.V.V., Klejwa, M., Swarz, G.A., Vergo, N., 1990. High spectral resolution reflectance spectroscopy of minerals. *J. Geophys. Res.* 95 (B8), 12,653–12,680. <https://doi.org/10.1029/JB095iB08p12653>.
- Clark, D.L., Oviatt, C.G., Dinter, D.A., 2015. Interim Geologic Map of the East and Central Parts of the Tooele 30'x60' Quadrangle, Tooele, Salt Lake, and Davis Counties, Utah, Year2.
- Cloutis, E.A., Hawthorne, F.C., Mertzman, S.A., Krenn, K., Craig, M.A., Marcino, D., Methot, M., Strong, J., Mustard, J.F., Blaney, D.L., Bell, J.F., Vilas, F., 2006. Detection and discrimination of sulfate minerals using reflectance spectroscopy. *Icarus* 184 (1), 121–157. <https://doi.org/10.1016/j.icarus.2006.04.003>.
- Coney, P.J., Smith, R., Eaton, G., 1978. Mesozoic-Cenozoic Cordilleran Plate Tectonics. *Cenozoic Tectonics and Regional Geophysics of the Western Cordillera*. Geological Society of America Memoir, pp. 33–50.
- Contreras Acosta, I., Khodadadzadeh, M., Tusa, L., Ghamisi, P., Glaaguen, R., 2019. A machine learning framework for drill-core mineral mapping using hyperspectral and high-resolution mineralogical data fusion. *IEEE Journal of Selected Topics in Applied Earth Observations and Remote Sensing* 1–14.
- Contreras, C., Khodadadzadeh, M., Tusa, L., Ghamisi, P., Glaaguen, R., 2018. A machine learning technique for drill core hyperspectral data analysis. *2018 9th Workshop on Hyperspectral Image and Signal Processing: Evolution in Remote Sensing (WHISPERS) 1–5*.
- Cracknell, M.J., Parbhakar-Fox, A., Jackson, L., Savinova, E., 2018. Automated acid rock drainage indexing from drill core imagery. *Minerals* 8 (12), 571. <https://doi.org/10.3390/min8120571>.
- Crowley, J.K., Williams, D.E., Hammarstrom, J.M., Piatak, N., Chou, I.M., Mars, J.C., 2003. Spectral reflectance properties (0.4–2.5 μm) of secondary Fe-oxide, Fe-hydroxide, and Fe-sulphate-hydrate minerals associated with sulphide-bearing mine wastes. *Geochemistry* 3, 219–228. <https://doi.org/10.1144/1467-7873/03-001>.
- Dalm, M., Buxton, M.W.N., van Ruitenberg, F.J.A., Voncken, J.H.L., 2014. Application of near-infrared spectroscopy to sensor based sorting of a porphyry copper ore. *Minerals Eng.* 58, 7–16. <https://doi.org/10.1016/j.mine.2013.12.016>.
- Dalm, M., Buxton, M.W.N., van Ruitenberg, F.J.A., 2017. Discriminating ore and waste in a porphyry copper deposit using short-wavelength infrared (SWIR) hyperspectral imagery. *Minerals Eng.* 105, 10–18. <https://doi.org/10.1016/j.mine.2016.12.013>.
- de Donato, P., Barres, O., Sausse, J., Martin, D., 2018. Near real-time ground-to-ground infrared remote-sensing combination and inexpensive visible camera observations applied to tomographic stack emission measurements. *Remote Sensing* 10 (5), 678. <https://doi.org/10.3390/rs10050678>.
- Denk, M., Gläßer, C., Kurz, T.H., Buckley, S.J., Drissen, P., 2015. Mapping of iron and steelwork by-products using close range hyperspectral imaging: a case study in Thuringia, Germany. *Eur. J. Remote Sensing* 48, 489–509. <https://doi.org/10.5721/EuJRS20154828>.
- Dubois, J., Neil Lewis, E., Fry, F.S., Calvey, E.M., 2005. Bacterial identification by near-infrared chemical imaging of food-specific cards. *Food Microbiol.* 22 (6), 577–583. <https://doi.org/10.1016/j.fm.2005.01.001>.
- Duke, E.F., 1994. Near infrared spectra of muscovite, Tschermark substitution, and metamorphic reaction progress: Implications for remote sensing. *Geology* 22, 621–624.
- Dumke, I., Nornes, S.M., Purser, A., Marcon, Y., Ludvigsen, M., Ellefmo, S.L., Johnsen, G., Soreide, F., 2018. First hyperspectral imaging survey of the deep seafloor: high-resolution mapping of manganese nodules. *Remote Sensing Environ.* 209, 19–30. <https://doi.org/10.1016/j.rse.2018.02.024>.
- Edelman, G., van Leeuwen, T.G., Aalders, M.C., 2012. Hyperspectral imaging for the age estimation of blood stains at the crime scene. *Forens. Sci. Int.* 223 (1–3), 72–77. <https://doi.org/10.1016/j.forsciint.2012.08.003>.
- Effner, S.A., 1992. *The Geology, Hydrothermal Alteration, and Minor Element Geochemistry of the Goldstrike Mine*. University of Idaho, Washington County, Utah M.S. Thesis.
- Eisele, A., Chabrilat, S., Hecker, C., Hewson, R., Lau, I.C., Rogass, C., Segl, K., Cudahy, T.J., Udelhoven, T., Hostert, P., Kaufmann, H., 2015. Advantages using the thermal infrared (TIR) to detect and quantify semi-arid soil properties. *Remote Sensing Environ.* 163, 296–311. <https://doi.org/10.1016/j.rse.2015.04.001>.
- Entezari, I., Rivard, B., Lipsett, M.G., Wilson, G.W., 2016. Prediction of water content and normalized evaporation from oil sands soft tailings surface using hyperspectral observations. *Can. Geotech. J.* 53 (10), 1742–1750. <https://doi.org/10.1139/cgj-2015-0416>.
- Eslinger, E.V., Savin, S.M., 1973. Mineralogy and oxygen isotope geochemistry of hydrothermally altered rocks of the Ohaki-Broadlands, New Zealand geothermal area. *Am. J. Sci.* 273, 240–267. <https://doi.org/10.2475/ajs.273.3.240>.
- Ewing, T., 2004. *Volcanoes, Asphalt, Tectonics and Groundwater in the Uvalde area, southwest Texas. South Texas Geological Society Guidebook*, San Antonio.
- Feng, J., Rivard, B., Gallie, E.A., Sanchez, A., 2006. Quantifying total sulfide content of cores and cut-rock surfaces using thermal infrared reflectance. *Geophysics* 71 (3), M1–M9. <https://doi.org/10.1190/1.2195990>.
- Feng, J., Rogge, D., Rivard, B., 2018. Comparison of lithological mapping results from airborne hyperspectral VNIR-SWIR, LWIR and combined data. *Int. J. Appl. Earth Observ. Geoinform.* 64, 340–353. <https://doi.org/10.1016/j.jag.2017.03.003>.
- Ferreira, K.B., Oliveira, A.G.G., Gonçalves, A.S., Gomes, J.A., 2017. Evaluation of Hyperspectral Imaging Visible/Near Infrared Spectroscopy as a forensic tool for automotive paint distinction. *Forens. Chem.* 5, 46–52. <https://doi.org/10.1016/j.fore.2017.06.001>.
- Fox, N., Parbhakar-Fox, A., Moltzen, J., Feig, S., Goemann, K., Huntington, J., 2016. Applications of hyperspectral mineralogy for geoenvironmental characterisation. *Minerals Eng.* 107, 63–77. <https://doi.org/10.1016/j.mine.2016.11.008>.
- Fraser, S.J., Whitbourn, L., Yang, K., Ramanaidou, E., Connor, P., Poropat, G., Soole, P., Mason, P., Coward, D., Phillips, R., 2006. Mineralogical Face-Mapping Using Hyperspectral Scanning for Mine Mapping and Control. *6th International Mining Geology Conference*, Darwin, NT Australia 227–232.
- Gallie, E.A., McArdle, S., Rivard, B., Francis, H., 2002. Estimating sulphide ore grade in broken rock using visible/infrared reflectance spectra. *Int. J. Remote Sensing* 23 (11), 2229–2246. <https://doi.org/10.1080/01431160110075604>.
- Gevaux, L., Adnet, C., Séroul, P., Clerc, R., Tréméau, A., Perrot, J.L., Hébert, M., 2018. Three-dimensional hyperspectral imaging: a new method for human face acquisition. *Electronic Imaging* 2018 (8), 152–152–10. <https://doi.org/10.2352/issn.2470-1173.2018.8.maap-152>.
- Goetz, A.F.H., 2009. Three decades of hyperspectral remote sensing of the Earth: a personal view. *Remote Sensing Environ.* 113, S5–S16. <https://doi.org/10.1016/j.rse.2007.12.014>.
- Graham, G.E., Kokaly, R.F., Kelley, K.D., Hoefen, T.M., Johnson, M.R., Hubbard, B.E., 2018. Application of imaging spectroscopy for mineral exploration in Alaska: a study over porphyry Cu deposits in the Eastern Alaska Range. *Econ. Geol.* 113 (2), 489–510. <https://doi.org/10.5382/econeo.2018.4559>.
- Green, A.A., Berman, M., Switzer, P., Craig, M.D., 1988. A transformation for ordering multispectral data in terms of image quality with implications for noise removal.

- Geosci. Remote Sensing, IEEE Trans. 26 (1), 65–74. <https://doi.org/10.1109/36.3001>.
- Greenan, D.M., 1992. *Geology and Remote Sensing of the Goldstrike District, Washington County, Utah: An Integrated Study*. University of Colorado, Boulder, CO 160 pp.
- Greenberger, R.N., Mustard, J.F., Cloutis, E.A., Mann, P., Wilson, J.H., Flemming, R.L., Robertson, K.M., Salvatore, M.R., Edwards, C.S., 2015a. Hydrothermal alteration and diagenesis of terrestrial lacustrine pillow basalts: Coordination of hyperspectral imaging with laboratory measurements. *Geochimica et Cosmochimica Acta* 171, 174–200. <https://doi.org/10.1016/j.gca.2015.08.024>.
- Greenberger, R.N., Mustard, J.F., Ehlmann, B.L., Blaney, D.L., Cloutis, E.A., Wilson, J.H., Green, R.O., Fraeman, A.A., 2015b. Imaging spectroscopy of geological samples and outcrops: Novel insights from microns to meters. *GSA Today* 25 (12), 4–10. <https://doi.org/10.1130/gsatg252a.1>.
- Greenberger, R.N., Ehlmann, B.L., Jewell, P.W., Birgenheier, L.P., Green, R.O., 2016. Detection of organic-rich oil shales of the Green River Formation, Utah, with ground-based imaging spectroscopy. 8th Workshop on Hyperspectral Image and Signal Processing: Evolution in Remote Sensing (WHISPERS). IEEE, Piscataway, NJ 1–5.
- Gupta, R.P., 2018. Imaging Spectroscopy. pp. 203–219.
- Gustin, M.M., Smith, M.T., 2016. Technical Report on the Goldstrike Project, Washington County, Utah, U.S.A., Pilot Gold, Inc., Reno, NV.
- Haijun, Q., Xiu, J., Liu, Z., Irene Maxime, D., Shaowen, L., 2017. Predicting sandy soil moisture content with hyperspectral imaging. *Int. J. Agric. Biol. Eng.* 10 (6), 175–183. <https://doi.org/10.25165/j.ijabe.20171006.2614>.
- Hakala, T., Suomalainen, J., Kaasalainen, S., Chen, Y., 2012. Full waveform hyperspectral LiDAR for terrestrial laser scanning. *Optics Express* 20 (7), 7119–7127. <https://doi.org/10.1364/OE.20.007119>.
- Hall, G.E.M., Bonham-Carter, G.F., 1988. Review of methods to determine gold, platinum and palladium in production-oriented geochemical laboratories, with application of a statistical procedure to test for bias. *J. Geochem. Explor.* 30 (1), 255–286. [https://doi.org/10.1016/0375-6742\(88\)90064-7](https://doi.org/10.1016/0375-6742(88)90064-7).
- Hartzell, P., Glennie, C., Khan, S., 2017. Terrestrial hyperspectral image shadow restoration through lidar fusion. *Remote Sensing* 9 (5), 421. <https://doi.org/10.3390/rs9050421>.
- Hobley, E., Steffens, M., Bauke, S.L., Kögel-Knabner, I., 2018. Hotspots of soil organic carbon storage revealed by laboratory hyperspectral imaging. *Sci. Rep.* 8 (1), 13900. <https://doi.org/10.1038/s41598-018-31776-w>.
- Holma, H., Hyvärinen, T., Mattila, A.-J., Kormano, I., 2012a. Thermal hyperspectral chemical imaging. In: Druy, M.A., Crocombe, R.A. (Eds.), *Next-Generation Spectroscopic Technologies SPIE*, Baltimore.
- Holma, H., Roos, A., Hyvarinen, T., Mattila, A.-J., Kormano, I., 2012. Thermal hyperspectral imagers and their applications. *SPIE Newsroom* 8374, 83740E1–83740E12. <https://doi.org/10.1117/2.1201207.004290>.
- Horvath, H., 1993. Atmospheric light absorption—A review. *Atmos. Environ.* 27 (3), 293–317. [https://doi.org/10.1016/0960-1686\(93\)90104-7](https://doi.org/10.1016/0960-1686(93)90104-7).
- Hulley, G.C., Duren, R.M., Hopkins, F.M., Hook, S.J., Vance, N., Guillevic, P., Johnson, W.R., Eng, B.T., Mihaly, J.M., Jovanovic, V.M., Chazanoff, S.L., Staniszewski, Z.K., Kuai, L., Worden, J., Frankenberg, C., Rivera, G., Aubrey, A.D., Miller, C.E., Malakar, N.K., Sánchez Tomás, J.M., Holmes, K.T., 2016. High spatial resolution imaging of methane and other trace gases with the airborne Hyperspectral Thermal Emission Spectrometer (HyTES). *Atmosp. Measur. Tech.* 9 (5), 2393–2408. <https://doi.org/10.5194/amt-9-2393-2016>.
- Hunt, G.R., Salisbury, J.W., 1970. Visible and near-infrared spectra of minerals and rocks: I Silicate minerals. *Modern Geol.* 1, 283–300.
- Izawa, M.R.M., Cloutis, E.A., Rhind, T., Mertzman, S.A., Poitras, J., Applin, D.M., Mann, P., 2018. Spectral reflectance (0.35–2.5 μm) properties of garnets: implications for remote sensing detection and characterization. *Icarus* 300, 392–410. <https://doi.org/10.1016/j.icarus.2017.09.005>.
- Jackisch, R., Jakob, S., Zimmermann, R., Gloaguen, R., 2017. Analysis of Temporal Changes of a Mining Site Affected by AMD. UAV Based Hyperspectral Monitoring of the Litov tailing (Sokolov, CZ).
- Jackisch, R., Lorenz, S., Zimmermann, R., Möckel, R., Gloaguen, R., 2018. Drone-Borne Hyperspectral Monitoring of Acid Mine Drainage: An Example from the Sokolov Lignite District. *Remote Sensing* 10 (3), 385. <https://doi.org/10.3390/rs10030385>.
- Jakob, S., Zimmermann, R., Gloaguen, R., 2017. The need for accurate geometric and radiometric corrections of drone-borne hyperspectral data for mineral exploration: MEPHYSTo—A toolbox for pre-processing drone-borne hyperspectral data. *Remote Sensing* 9 (1). <https://doi.org/10.3390/rs9010088>.
- Jensen, M., Laylander, P., 1975. Summary of Space Imagery Studies in Utah and Nevada Using LANDSAT 1, EREP, and Skylab Imagery.
- Job, A.T., Edgar, M.L., McAree, P.R., 2017. Real-Time Shovel-Mounted Coal or Ore Sensing, Iron Ore 2017. AusIMM, Perth, Australia, pp. 397–406.
- Kang, S., Lee, K.-Y., Jeon, E.-I., Yu, S.-J., Shin, I.H., Kwon, O.-S., 2018. Evaluating laboratory-based classification potentials of heavy metal contaminated soils using spectro-radiometer and hyper-spectral imagery. *Spatial Inform. Res.* 26, 213–221. <https://doi.org/10.1007/s41324-018-0172-4>.
- Kastek, M., Piatkowski, T., Dulski, R., Chamberland, M., Lagueux, P., Farley, V., 2012. Method of gas detection applied to infrared hyperspectral sensor. *Photon. Lett. Poland* 4 (4). <https://doi.org/10.4302/plp.2012.4.09>.
- Khan, S., Okyay, U., Ahmad, L., Shah, M., 2018. Characterization of gold mineralization in Northern Pakistan using imaging spectroscopy. *Photogram. Eng. Remote Sensing* 84 (7), 425–434. <https://doi.org/10.14358/PERS.84.7.425>.
- Kirsch, M., Lorenz, S., Zimmermann, R., Tusa, L., Möckel, R., Hödl, P., Booysen, R., Khodadadzadeh, M., Gloaguen, R., 2018. Integration of terrestrial and drone-borne hyperspectral and photogrammetric sensing methods for exploration mapping and mining monitoring. *Remote Sensing* 10 (9), 1366. <https://doi.org/10.3390/rs10091366>.
- Kokaly, R.F., Hoefen, T.M., Graham, G.E., Kelley, K.D., Johnson, M.R., Hubbard, B.E., Goldfarb, R.J., Buchhorn, M., Prakash, A., 2016. Mineral information at micron to kilometer scales: Laboratory, field, and remote sensing imaging spectrometer data from the orange hill porphyry copper deposit, Alaska, USA. *Geoscience and Remote Sensing Symposium (IGARSS)*, 2016 IEEE International. IEEE 5418–5421.
- Kokaly, R., Graham, G.E., Hoefen, T.M., Kelley, K.D., Johnson, M.R., Hubbard, B.E., Buchhorn, M., Prekash, A., 2017. Multiscale hyperspectral imaging of the orange hill porphyry copper deposit, Alaska, USA, with Laboratory-, Field-, and Aircraft-based Imaging Spectrometers. In: Tschirhart, V., Thomas, M.D. (Eds.), *Sixth Decennial International Conference on Mineral Exploration. Spectral Geology and Remote Sensing*. pp. 923–943.
- Kopačková, V., Koucká, L., 2014. QUAN TOOLS: New Tools for Mineral Mapping Using High Spectral Resolution Data, GRSG AGM - 25 Years of Geological Remote Sensing. U.K. Geological Society of London, London.
- Kopačková, V., Koucká, L., 2017. Integration of absorption feature information from visible to longwave infrared spectral ranges for mineral mapping. *Remote Sensing* 9 (10), 1006. <https://doi.org/10.3390/rs9101006>.
- Kopačková, V., Chevreil, S., Bourguignon, A., Rojík, P., 2012. Application of high altitude and ground-based spectroradiometry to mapping hazardous low-pH material derived from the Sokolov open-pit mine. *J. Maps* 8 (3), 220–230. <https://doi.org/10.1080/17445647.2012.705544>.
- Kosanovic, T., Perry, S.E., Lopez, R., 2017. Hyperspectral Imaging Technology Development and Application; Implications for Thin-Bedded Reservoir Characterization. AAPG Annual Convention and Exhibition, Houston, TX.
- Krupnik, D., Khan, S., Okyay, U., Hartzell, P., Zhou, H.-W., 2016. Study of Upper Albian rudist buildups in the Edwards Formation using ground-based hyperspectral imaging and terrestrial laser scanning. *Sediment. Geol.* 345, 154–167. <https://doi.org/10.1016/j.sedgeo.2016.09.008>.
- Kruse, F.A., R, L.B., Tarank, J.V., Peppin, W.A., Weatherbee, O., Calvin, W.M., 2012. Mapping alteration minerals at prospect, outcrop and drill core scales using imaging spectrometry. *Int. J. Remote Sensing* 33 (6), 1780–1798. <https://doi.org/10.1080/01431161.2011.600350>.
- Kuosmanen, V., Arkimaa, H., Tiainen, M., Bärs, R., 2015. Hyperspectral close-range LWIR imaging spectrometry-3 case studies. *Geological Survey Finland, Special Paper* 58, 117–144.
- Kurz, T., Buckley, S., Howell, J., Schneider, D., 2008. Geological outcrop modelling and interpretation using ground based hyperspectral and laser scanning data fusion. *Int. Arch. Photogram.* 37, B5.
- Kurz, T.H., Buckley, S.J., Howell, J.A., Schneider, D., 2009. Close range hyperspectral and LiDAR data integration for geological outcrop analysis. In: *Hyperspectral Image and Signal Processing: Evolution in Remote Sensing*. IEEE. pp. 1–4.
- Kurz, T.H., Buckley, S.J., Howell, J.A., Schneider, D., 2011. Integration of panoramic hyperspectral imaging with terrestrial lidar data. *Photogram. Rec.* 26 (134), 212–228. <https://doi.org/10.1111/j.1477-9730.2011.00632.x>.
- Kurz, T.H., Dewit, J., Buckley, S.J., Thurmond, J.B., Hunt, D.W., Swennen, R., 2012. Hyperspectral image analysis of different carbonate lithologies (limestone, karst and hydrothermal dolomites): the Pozalagua Quarry case study (Cantabria, North-west Spain). *Sedimentology* 59 (2), 623–645. <https://doi.org/10.1111/j.1365-3091.2011.01269.x>.
- Kurz, T.H., Buckley, S.J., Howell, J.A., 2013. Close-range hyperspectral imaging for geological field studies: workflow and methods. *Int. J. Remote Sensing* 34 (5), 1798–1822. <https://doi.org/10.1080/01431161.2012.727039>.
- Kurz, T.H., Buckley, S.J., Becker, J.K., 2017. Hyperspectral imaging: a novel geological mapping technique for subsurface construction sites. *Proceedings of the World Tunnel Congress 2017 – Surface Challenges – Underground Solutions*, Bergen, Norway.
- Laakso, K., Rivard, B., Rogge, D., 2016. Enhanced detection of gossans using hyperspectral data: Example from the Cape Smith Belt of northern Quebec, Canada. *ISPRS J. Photogram. Remote Sensing* 114, 137–150. <https://doi.org/10.1016/j.isprsjprs.2016.02.004>.
- Laakso, K., Middleton, M., Heinig, T., Bärs, R., Lintinen, P., 2018. Assessing the ability to combine hyperspectral imaging (HSI) data with Mineral Liberation Analyzer (MLA) data to characterize phosphate rocks. *Int. J. Appl. Earth Observ. Geoinform.* 69, 1–12. <https://doi.org/10.1016/j.jag.2018.02.018>.
- Laakso, K., Turner, D.J., Rivard, B., Sánchez-Azofeifa, A., 2019. The long-wave infrared (8–12 μm) spectral features of selected rare earth element–bearing carbonate, phosphate and silicate minerals. *Int. J. Appl. Earth Observ. Geoinform.* 76, 77–83. <https://doi.org/10.1016/j.jag.2018.11.005>.
- Lanier, G., John, E., Swensen, A., Reid, J., Bard, C., Caddey, S., Wilson, J., 1978. General geology of the Bingham mine, Bingham canyon, Utah. *Econ. Geol.* 73 (7), 1228–1241. <https://doi.org/10.2113/gsecongeo.73.7.1228>.
- Lee, M.R., Martin, R.W., Trager-Cowan, C., Edwards, P.R., 2005. Imaging of cathodoluminescence zoning in calcite by scanning electron microscopy and hyperspectral mapping. *J. Sediment. Res.* 75 (2), 313–322. <https://doi.org/10.2110/jsr.2005.023>.
- Li, Q., He, X., Wang, Y., Liu, H., Xu, D., Guo, F., 2013. Review of spectral imaging technology in biomedical engineering: achievements and challenges, 18. *SPIE*. pp. 29.
- Li, B., Cobo-Medina, M., Lecourt, J., Harrison, N., Harrison, R.J., Cross, J.V., 2018. Application of hyperspectral imaging for nondestructive measurement of plum quality attributes. *Postharvest Biol. Technol.* 141, 8–15. <https://doi.org/10.1016/j.postharvbio.2018.03.008>.
- Lin, Y., Jiang, M., 2018. From prototype system to practical application of hyperspectral LiDAR: Investigation of the intraday 3D variations of tree biophysics and biochemistry. *SPIE Asia-Pacific Remote Sensing*, 10779. *SPIE*.
- Lorenz, S., Kirsch, M., Zimmermann, R., Tusa, L., Mockel, R., Chamberland, M., Gloaguen, R., 2018a. In: Long-wave hyperspectral imaging for lithological mapping: a case

- study. 20th EGU General Assembly, EGU2018, Vienna, Austria. pp. 10262.
- Lorenz, S., Salehi, S., Kirsch, M., Zimmermann, R., Unger, G., Vest Sørensen, E., Gloaguen, R., 2018b. Radiometric correction and 3D integration of long-range ground-based hyperspectral imagery for mineral exploration of vertical outcrops. *Remote Sensing* 10 (2), 176. <https://doi.org/10.3390/rs10020176>.
- Lorenz, S., Zimmermann, R., Gloaguen, R., 2017. The need for accurate geometric and radiometric corrections of drone-borne hyperspectral data for mineral exploration: MEPhySTo—A toolbox for pre-processing drone-borne hyperspectral data. *Remote Sensing* 9. <https://doi.org/10.3390/rs9010088>.
- Lowell, D.J., Guillet, J.M., 1970. Lateral and vertical alteration-mineralization zoning in porphyry ore deposits. *Econ. Geol.* 65 (4), 373–408. <https://doi.org/10.2113/gsecongeo.65.4.373>.
- Lu, G., Fei, B., 2014. Medical hyperspectral imaging: a review. *J. Biomed. Opt.* 19 (1), 10901. <https://doi.org/10.1117/1.JBO.19.1.010901>.
- Lyder, D., Feng, J., Rivard, B., Gallie, A., Cloutis, E., 2010. Remote bitumen content estimation of Athabasca oil sand from hyperspectral infrared reflectance spectra using Gaussian singlets and derivative of Gaussian wavelets. *Fuel* 89 (3), 760–767. <https://doi.org/10.1016/j.fuel.2009.03.027>.
- Ma, J., Sun, D.W., Pu, H., Cheng, J.H., Wei, Q., 2019. Advanced techniques for hyperspectral imaging in the food industry: principles and recent applications. *Annu. Rev. Food Sci. Technol.* 10, 197–220. <https://doi.org/10.1146/annurev-food-032818-121155>.
- Malkamäki, T., Kaasalainen, S., Ilinca, J., 2018. Improving the Full Waveform Digitizing in an Eight Channel Portable Hyperspectral Lidar, Light, Energy and the Environment 2018 (E2, FTS, HISE, SOLAR, SSL). OSA Technical Digest. Optical Society of America, Singapore HM4C.4.
- Manßl, Y., Hilgers, C., Buddenbaum, H., Stanjek, H., 2017. Visualising mineralogical heterogeneities and texture in a mudstone concretion using hyperspectral imaging. *Zeitschrift der Deutschen Gesellschaft für Geowissenschaften* 168 (3), 403–414. <https://doi.org/10.1127/zdg/2017/0118>.
- Mathieu, M., Roy, R., Launeau, P., Cathelineau, M., Quirt, D., 2017. Alteration mapping on drill cores using a HySpec SWIR-320nm hyperspectral camera: application to the exploration of an unconformity-related uranium deposit (Saskatchewan, Canada). *J. Geochem. Explor.* 172, 71–88. <https://doi.org/10.1016/j.gexplo.2016.09.008>.
- McDougal, R.R., Clark, R.N., Vivo, K.E., Kokaly, R.F., Rockwell, B.W., Vance, J.S., 1999. Preliminary materials mapping in the Oquirrh Mountains region for the Utah EPA Project using AVIRIS data. In: Green, R.O. (Ed.), Summaries of the 8th Annual JPL Airborne Earth Science Workshop. JPL, pp. 291–298.
- McHugh, E.L., Girard, J.M., Denes, L.J., 2001. Simplified hyperspectral imaging for improved geologic mapping of mine slopes. Third International Conference on Intelligent Processing and Manufacturing of Materials, Vancouver, BC.
- McMillan, W.J., Panteleyev, A., 1980. Ore Deposit Models – 1. Porphyry Copper Deposits. *Geoscience Canada* 7 (2).
- Mehmani, Y., Burnham, A.K., Vanden Berg, M.D., Tchelepi, H.A., 2017. Quantification of organic content in shales via near-infrared imaging: Green River Formation. *Fuel* 208, 337–352. <https://doi.org/10.1016/j.fuel.2017.07.027>.
- Mielke, C., Boesche, N., Rogass, C., Kaufmann, H., Gauert, C., de Wit, M., 2014. Spaceborne mine waste mineralogy monitoring in south africa, applications for modern push-broom missions: hyperion/OLI and EnMAP/Sentinel-2. *Remote Sensing* 6 (8), 6790–6816. <https://doi.org/10.3390/rs6086790>.
- Mishra, P., Nordon, A., Mohd Asari, M.S., Lian, G., Redfern, S., 2019. Fusing spectral and textural information in near-infrared hyperspectral imaging to improve green tea classification modelling. *J. Food Eng.* 249, 40–47. <https://doi.org/10.1016/j.jfoodeng.2019.01.009>.
- Monteiro, S.T., Nieto, J., Murphy, R., Ramakrishnan, R., Taylor, Z., 2013. Combining strong features for registration of hyperspectral and LiDAR data from field-based platforms. *Geoscience and Remote Sensing Symposium (IGARSS). IEEE International* 1210–1213.
- Muntean, J.L., Cline, J.S., Simon, A.C., Longo, A.A., 2011. Magmatic-hydrothermal origin of Nevada's Carlin-type gold deposits. *Nat. Geosci.* 4 (2), 122–127. <https://doi.org/10.1038/ngeo1064>.
- Murphy, R.J., Monteiro, S.T., 2013. Mapping the distribution of ferric iron minerals on a vertical mine face using derivative analysis of hyperspectral imagery (430–970nm). *ISPRS J. Photogram. Remote Sensing* 75, 29–39. <https://doi.org/10.1016/j.isprsjprs.2012.09.014>.
- Murphy, R.J., Monteiro, S.T., Schneider, S., 2012. Evaluating classification techniques for mapping vertical geology using field-based hyperspectral sensors. *Geosci. Remote Sensing IEEE Trans.* 50 (8), 3066–3080. <https://doi.org/10.1109/TGRS.2011.2178419>.
- Murphy, R., Schneider, S., Monteiro, S., 2014a. Mapping layers of clay in a vertical geological surface using hyperspectral imagery: variability in parameters of swirl absorption features under different conditions of illumination. *Remote Sensing* 6 (9), 9104–9129. <https://doi.org/10.3390/rs6099104>.
- Murphy, R.J., Schneider, S., Monteiro, S.T., 2014b. Consistency of measurements of wavelength position from hyperspectral imagery: use of the ferric iron crystal field absorption at ~900 nm as an Indicator of Mineralogy. *IEEE Trans. Geosci. Remote Sensing* 52 (5), 2843–2857. <https://doi.org/10.1109/tgrs.2013.2266672>.
- Murphy, R.J., Taylor, Z., Schneider, S., Nieto, J., 2015. Mapping clay minerals in an open-pit mine using hyperspectral and LiDAR data. *Eur. J. Remote Sensing* 511–526. <https://doi.org/10.5721/EuJRS20154829>.
- Murphy, R.J., Van Kranendonk, M.J., Kelloway, S.J., Wainwright, I.E., 2016. Complex patterns in fossilized stromatolites revealed by hyperspectral imaging (400–2496 nm). *Geobiology* 14 (5), 419–439. <https://doi.org/10.1111/gbi.12184>.
- Mustard, J.F., 1992. Chemical analysis of actinolite from reflectance spectra. *Am. Mineral.* 77, 345–358.
- Nageshwaraniyer, S., Kim, K., Son, Y., 2018. A mine-to-mill economic analysis model and spectral imaging-based tracking system for a copper mine. *J. Southern African Inst. Mining Metal.* 118 (1), 7–14. <https://doi.org/10.17159/2411-9717/2018/v118n1a2>.
- Neave, D.A., Black, M., Riley, T.R., Gibson, S.A., Ferrier, G., Wall, F., Broom-Fendley, S., 2016. On the feasibility of imaging carbonatite-hosted rare earth element deposits using remote sensing. *Econ. Geol.* 111 (4), 641–665. <https://doi.org/10.2113/econgeo.111.3.641>.
- Nelson, C.E., 1990. Comparative geochemistry of jasperoids from Carlin-type gold deposits of the western United States. *J. Geochem. Explor.* 36, 171–195. [https://doi.org/10.1016/0375-6742\(90\)90055-F](https://doi.org/10.1016/0375-6742(90)90055-F).
- Okyay, U., Khan, S.D., 2016. Remote detection of fluid-related diagenetic mineralogical variations in the Wingate Sandstone at different spatial and spectral resolutions. *Int. J. Appl. Earth Observ. Geoinform.* 44, 70–87. <https://doi.org/10.1016/j.jag.2015.08.001>.
- Okyay, U., Khan, S.D., 2018. Spatial co-registration and spectral concatenation of panoramic ground-based hyperspectral images. *Photogramm. Eng. Remote Sensing* 84 (12), 781–790. <https://doi.org/10.14358/pers.84.12.781>.
- Okyay, Ü., Khan, D.S., Lakshmi Kantha, R.M., Sarmiento, S., 2016. Ground-based hyperspectral image analysis of the Lower Mississippian (Osagean) Reeds Spring Formation Rocks in Southwestern Missouri. *Remote Sensing* 8 (12). <https://doi.org/10.3390/rs8121018>.
- O'Rourke, S.M., Holden, N.M., 2012. Determination of soil organic matter and carbon fractions in forest top soils using spectral data acquired from visible–near infrared hyperspectral images. *Soil Science Society of America Journal* 76 (2). <https://doi.org/10.2136/sssaj2011.0053>.
- Pande-Chhetri, R., Abd-Elrahman, A., 2013. Filtering high-resolution hyperspectral imagery in a maximum noise fraction transform domain using wavelet-based despeckling. *Int. J. Remote Sensing* 34 (6), 2216–2235. <https://doi.org/10.1080/01431161.2012.742592>.
- Payne, G., Wallace, C., Reedy, B., Lennard, C., Schuler, R., Exline, D., Roux, C., 2005. Visible and near-infrared chemical imaging methods for the analysis of selected forensic samples. *Talanta* 67 (2), 334–344. <https://doi.org/10.1016/j.talanta.2005.03.042>.
- Price, J.G., 2013. The challenges of mineral resources for society. *Geol. Soc. Am. Special Papers* 501, 1–19.
- Qiu, J.-T., Zhang, C., Xu, Q.-J., Yao, J.-L., 2017. Mapping of carnallite along with semi-quantitative estimation of potassium content of drill cores using hyperspectral imagery. *Remote Sensing Lett.* 8 (9), 859–868. <https://doi.org/10.1080/2150704x.2017.1333651>.
- Rabie, M., Franck, C.M., 2018. Assessment of eco-friendly gases for electrical insulation to replace the most potent industrial greenhouse gas SF6. *Environ. Sci. Technol.* 52 (2), 369–380. <https://doi.org/10.1021/acs.est.7b03465>.
- Ragona, D., Minster, B., Rockwell, T., Fialko, Y., Bloom, R., Hemlinger, M., 2004. Towards the Development of Hyperspectral Images of Trench Walls. *Automatic Data acquisition, Robotronch.*
- Ramanaidou, E., Wells, M., Lau, I., Laukamp, C., 2015. Characterization of Iron Ore by Visible and Infrared Reflectance and, Raman Spectroscopies. pp. 191–228.
- Rivard, B., Lyder, D., Feng, J., Gallie, A., Cloutis, E., Dougan, P., Gonzalez, S., Cox, D., Lipsett, M.G., 2010. Bitumen content estimation of Athabasca oil sand from broad band infrared reflectance spectra. *Can. J. Chem. Eng.* 88, 830–838. <https://doi.org/10.1002/cjce.20343>.
- Rivard, B., Harris, N.B., Feng, J., Dong, T., 2018. Inferring total organic carbon and major element geochemical and mineralogical characteristics of shale core from hyperspectral imagery. *AAPG Bull.* 102 (10), 2101–2121. <https://doi.org/10.1306/03291817217>.
- Rockwell, B.W., McDougal, R.R., Gent, C.A., 2005. *Remote Sensing for Environmental Site Screening and Watershed Evaluation in Utah Mine Lands—East Tintic Mountains, Oquirrh Mountains, and Tushar Mountains, USGS, Denver, CO.*
- Rogass, C., Koerting, F.M., Mielke, C., Brell, M., Boesche, N.K., Bade, M., Hohmann, C., 2017. Translational Imaging spectroscopy for proximal sensing. *Sensors (Basel)* 17 (8). <https://doi.org/10.3390/s17081857>.
- Rosa, D., Dewolfe, M., Guarneri, P., Kolb, J., Laflamme, C., Partin, C., Salehi, S., Sørensen, E., Thaastrup, S., Thrane, K., Zimmermann, R., 2017. Architecture and Mineral Potential of the Paleoproterozoic Karrat Group, West Greenland Results of the 2016 Season.
- Rowe, D., Gray, J.N., Simmons, G., 2018. Independent Technical Report and Resource Estimate for the Goldstrike Project, Washington County, Utah USA. *Goldstrike NI 43-101, SRK Consulting.*
- Rowley, P., Anderson, R., Hacker, D., Boswell, J., Maxwell, D., Cox, D., Willden, R., Adair, D., 2010. Interim Geologic Map of the Goldstrike Quadrangle and East Part of the Docs Pass Quadrangle. *Utah Geological Survey Open-File Report, Washington County, Utah*, pp. 510.
- Sabbah, S., Harig, R., Rusch, P., Eichmann, J., Keens, A., Gerhard, J.-H., 2012. *Remote Sensing of Gases by Hyperspectral Imaging: System Performance and Measurements, 51. SPIE. 1–10, 10.*
- Salehi, S., 2018. Hyperspectral analysis of lithologies in the Arctic in areas with abundant lichen cover. *Geol. Surv. Denmark Greenland Bull.* 41, 51–55.
- Salehi, S., Rogge, D., Rivard, B., Heincke, B.H., Fensholt, R., 2017. Modeling and assessment of wavelength displacements of characteristic absorption features of common rock forming minerals encrusted by lichens. *Remote Sensing Environ.* 199, 78–92. <https://doi.org/10.1016/j.rse.2017.06.044>.
- Salehi, S., Lorenz, S., Vest Sørensen, E., Zimmermann, R., Fensholt, R., Henning Heincke, B., Kirsch, M., Gloaguen, R., 2018. Integration of vessel-based hyperspectral scanning and 3D-photogrammetry for mobile mapping of steep Coastal Cliffs in the Arctic. *Remote Sensing* 10 (2). <https://doi.org/10.3390/rs10020175>.
- Savitzky, A., Golay, M.J.E., 1964. Smoothing and differentiation of data by simplified least squares procedures. *Anal. Chem.* 36 (8), 1627–1639. <https://doi.org/10.1021>

- ac60214a047.
- Scafutto, R.D.P.M., Filho, S., Rivard, B., 2016. Characterization of mineral substrates impregnated with crude oils using proximal infrared hyperspectral imaging. *Remote Sensing Environ.* 179, 116–130. <https://doi.org/10.1016/j.rse.2016.03.033>.
- Scafutto, R.D.P.M., de Souza Filho, C.R., de Oliveira, W.J., 2017. Hyperspectral remote sensing detection of petroleum hydrocarbons in mixtures with mineral substrates: implications for onshore exploration and monitoring. *ISPRS J. Photogram. Remote Sensing* 128, 146–157. <https://doi.org/10.1016/j.isprsjprs.2017.03.009>.
- Schaefer, S., Hostert, P., Damm, A., 2006. Correcting brightness gradients in hyperspectral data from urban areas. *Remote Sensing Environ.* 101 (1), 25–37. <https://doi.org/10.1016/j.rse.2005.12.003>.
- Schneider, S., Melkumyan, A., Murphy, R.J., Nettleton, E., 2011a. Classification of hyperspectral imagery using GPs and the OAD covariance function with automated endmember extraction. 2011 IEEE 23rd International Conference on Tools with Artificial Intelligence 579–584.
- Schneider, S., Murphy, R.J., Melkumyan, A., Nettleton, E., 2011b. Autonomous mapping of mine face geology using hyperspectral data. 35th APCOM Symposium 24–30.
- Schneider, S., Melkumyan, A., Murphy, R.J., Nettleton, E., 2012. A geological perception system for autonomous mining. 2012 IEEE International Conference on Robotics and Automation 2986–2991.
- Schodlok, M.C., Whitbourn, L., Huntington, J., Mason, P., Green, A., Berman, M., Coward, D., Connor, P., Wright, W., Jolivet, M., Martinez, R., 2016. HyLogger-3, a visible to shortwave and thermal infrared reflectance spectrometer system for drill core logging: functional description. *Aust. J. Earth Sci.* 63 (8), 929–940. <https://doi.org/10.1080/08120099.2016.1231133>.
- Seedorff, E., Dilles, J.H., Proffett, J.J.M., Einaudi, M.T., Zurcher, L., Stavast, W.J.A., Johnson, D.A., Barton, M.D., 2005. In: Hedenquist, J.W., Thompson, J.F.H., Goldfarb, R.J., Richards, J.P. (Eds.), *Porphyry Deposits: Characteristics and Origin of Hypogene Features. One Hundredth Anniversary Volume. Society of Economic Geologists*. <https://doi.org/10.5382/AV100.10>.
- Sheibley, D.W., Fowler, M.H., 1966. *Infrared Spectra of Various Metal Oxides in the Region of 2 to 26 microns*. National Aeronautics and Space Administration, Lewis Research Center Cleveland, Ohio, Washington, D.C.
- Shi, C., Qian, J., Zhu, W., Liu, H., Han, S., Yang, X., 2019. Nondestructive determination of freshness indicators for tilapia fillets stored at various temperatures by hyperspectral imaging coupled with RBF neural networks. *Food Chem.* 275, 497–503. <https://doi.org/10.1016/j.foodchem.2018.09.092>.
- Sillitoe, R.H., 2010. Porphyry copper systems. *Econ. Geol.* 105 (1), 3–41. <https://doi.org/10.2113/gsecongeo.105.1.3>.
- Silversides, K.L., Murphy, R.J., 2016. Identification of marker shale horizons in banded iron formation: linking measurements of downhole natural gamma-ray with measurements from reflectance spectrometry of rock cores. *Near Surface Geophys.* 15 (2), 141–153. <https://doi.org/10.3997/1873-0604.2016046>.
- Sima, A.A., Buckley, S.J., Kurz, T.H., Schneider, D., 2014. Semi-automated registration of close-range hyperspectral scans using oriented digital camera imagery and A 3d model. *Photogram. Rec.* 29 (145), 10–29. <https://doi.org/10.1111/phor.12049>.
- Singer, R.B., 1981. Near-infrared spectral reflectance of mineral mixtures: systematic combinations of pyroxenes, olivine, and iron oxides. *J. Geophys. Res.* 86 (B9), 7967–7982. <https://doi.org/10.1029/JB086iB09p07967>.
- Sivathanu, Y., 2005. In: U.S. Department of Energy National Energy Technology Laboratory (Ed.), *Technology Status Report on Natural Gas Leak Detection in Pipelines*.
- Slezak, P., Spandler, C., Blake, K., 2018. Ghosts of apatite past: using hyperspectral cathodoluminescence and micro-geochemical data to reveal multi-generational apatite in the Gifford Creek Carbonate Complex, Australia. *Can. Mineral.* 56 (5), 773–797. <https://doi.org/10.3749/canmin.1800021>.
- Smekens, J.-F., Gouhier, M., 2018. Observation of SO 2 degassing at Stromboli volcano using a hyperspectral thermal infrared imager. *J. Volcanol. Geothermal Res.* 356, 75–89. <https://doi.org/10.1016/j.jvolgeores.2018.02.018>.
- Smith, G.M., Milton, E.J., 1999. The use of the empirical line method to calibrate remotely sensed data to reflectance. *Int. J. Remote Sensing* 20 (13), 2653–2662. <https://doi.org/10.1080/014311699211994>.
- Snyder, C.J., Khan, S.D., Bhattacharya, J.P., Glennie, C., Seepersad, D., 2016. Thin-bedded reservoir analogs in an ancient delta using terrestrial laser scanner and high-resolution ground-based hyperspectral cameras. *Sediment. Geol.* 342, 154–164. <https://doi.org/10.1016/j.sedgeo.2016.07.004>.
- Sorenson, P.T., Quideau, S.A., Rivard, B., 2018. High resolution measurement of soil organic carbon and total nitrogen with laboratory imaging spectroscopy. *Geoderma* 315, 170–177. <https://doi.org/10.1016/j.geoderma.2017.11.032>.
- Speed, R.C., Sleep, N.H., 1982. Antler orogeny and foreland basin: a model. *GSA Bull.* 93 (9), 815–828. [https://doi.org/10.1130/0016-7606\(1982\)93<815:AOAFBA>2.0.CO;2](https://doi.org/10.1130/0016-7606(1982)93<815:AOAFBA>2.0.CO;2).
- Spencer, A.B., 1969. Alkalic Igneous Rocks of the Balcones Province, Texas. *J. Petrol.* 10 (2), 272–306. <https://doi.org/10.1093/petrology/10.2.272>.
- Speta, M., Rivard, B., Feng, J., Lipsett, M., Gingras, M., 2013. Hyperspectral imaging for the characterization of athabasca oil sands drill core. *Geosci. Remote Sensing Symposium (IGARSS). IEEE 2184–2187*. <https://doi.org/10.1109/IGARSS.2013.6723248>.
- Speta, M., Rivard, B., Feng, J., Lipsett, M., Gingras, M., 2015. Hyperspectral imaging for the determination of bitumen content in Athabasca oil sands core samples. *AAPG Bull.* 99 (7), 1245–1259. <https://doi.org/10.1306/03021514121>.
- Steffens, M., Kohlpaintner, M., Buddenbaum, H., 2014. Fine spatial resolution mapping of soil organic matter quality in a Histosol profile. *Eur. J. Soil Sci.* 65 (6), 827–839. <https://doi.org/10.1111/ejss.12182>.
- Sture, O., Ludvigsen, M., Aas, L.M.S., 2017. Autonomous underwater vehicles as a platform for underwater hyperspectral imaging. *OCEANS 2017-Aberdeen. IEEE* 1–8.
- <https://doi.org/10.1109/OCEANSE.2017.8084995>.
- Sun, W., Zhang, X., Sun, X., Sun, Y., Cen, Y., 2018a. Predicting nickel concentration in soil using reflectance spectroscopy associated with organic matter and clay minerals. *Geoderma* 327, 25–35. <https://doi.org/10.1016/j.geoderma.2018.04.019>.
- Sun, L., Khan, S., Godet, A., 2018b. Integrated ground-based hyperspectral imaging and geochemical study of the Eagle Ford Group in West Texas. *Sediment. Geol.* 363, 34–47. <https://doi.org/10.1016/j.sedgeo.2017.10.012>.
- Sun, Y., Zhao, Y., Qin, K., Nie, Jiangtao, Li, H., 2015. Geological application of HySpec ground hyperspectral remote sensing in gold and uranium ore deposits. In: *Asia-Pacific Energy Equipment Engineering Research Conference (AP3ER 2015)*. Atlantis Press. pp. 392–395.
- Sun, L., Khan, S.D., Sarmiento, S., Lakshminikantha, M.R., Zhou, H., 2017. Ground-based hyperspectral imaging and terrestrial laser scanning for fracture characterization in the Mississippian Boone Formation. *Int. J. Appl. Earth Observ. Geoinform.* 63, 222–233. <https://doi.org/10.1016/j.jag.2017.08.008>.
- Sun, L., Khan, S., Shabestari, P., 2019. Integrated hyperspectral and geochemical study of sediment-hosted disseminated gold at the Goldstrike District, Utah. *Remote Sensing* 11 (17). <https://doi.org/10.3390/rs11171987>.
- Swanson, R., 2005. A Real-Time Coal Content/Ore Grade (C<sup>2</sup>OC) Sensor. Resonon, Inc.(US).
- Swazey, G.A., Smith, K.S., Clark, R.N., Sutley, S.J., Pearson, R.M., Vance, J.S., Hageman, P.L., Briggs, P.H., Meier, A.L., Singleton, M.J., 2000. Using imaging spectroscopy to map acidic mine waste. *Environ. Sci. Technol.* 34 (1), 47–54. <https://doi.org/10.1021/es990046w>.
- Tahmasbian, I., Xu, Z., Boyd, S., Zhou, J., Esmaeilani, R., Che, R., Hosseini Bai, S., 2018. Laboratory-based hyperspectral image analysis for predicting soil carbon, nitrogen and their isotopic compositions. *Geoderma* 330, 254–263. <https://doi.org/10.1016/j.geoderma.2018.06.008>.
- Tappert, M.C., Rivard, B., Fulop, A., Rogge, D., Feng, J., Tappert, R., Stalder, R., 2015. Characterizing Kimberlite Dilution by Crustal Rocks at the Snap Lake Diamond Mine (Northwest Territories, Canada) using SWIR (1.90–2.36μm) and LWIR (8.1–11.1μm) Hyperspectral Imagery Collected from Drill Core. *Econ. Geol.* 110 (6), 1375–1387. <https://doi.org/10.2113/econgeo.110.6.1375>.
- Taylor, R., 2011. *Gossans and Leached Cappings: Field Assessment*. Springer Science & Business Media.
- Turner, D., Rivard, B., Groat, L., 2014. Rare earth element ore grade estimation of mineralized drill core from hyperspectral imaging spectroscopy. 2014 IEEE Geoscience and Remote Sensing Symposium 4612–4615.
- Tusa, L., Andreani, L., Khodadadzadeh, M., Contreras, C., Ivascanu, P., Gloaguen, R., Guttmmer, J., 2019. Mineral mapping and vein detection in hyperspectral drill-core scans: application to porphyry-type mineralization. *Minerals* 9 (2), 122. <https://doi.org/10.3390/min9020122>.
- Uezato, T., Murphy, R.J., Melkumyan, A., Chlingaryan, A., Schneider, S., 2014. Multiple endmember spectral unmixing within a multi-task framework. *Geosci. Remote Sensing Symp. (IGARSS) 3454–3457*. <https://doi.org/10.1109/IGARSS.2014.6947225>.
- Valente, T.M., Gomes, C.L., 2009. Occurrence, properties and pollution potential of environmental minerals in acid mine drainage. *Sci. Total Environ.* 407 (3), 1135–1152. <https://doi.org/10.1016/j.scitotenv.2008.09.050>.
- van der Meer, F., Kopačková, V., Koucká, L., van der Werff, H.M.A., van Ruitenbeek, F.J.A., Bakker, W.H., 2018. Wavelength feature mapping as a proxy to mineral chemistry for investigating geologic systems: an example from the Rodalquilar epithermal system. *Int. J. Appl. Earth Observ. Geoinform.* 64, 237–248. <https://doi.org/10.1016/j.jag.2017.09.008>.
- van Ruitenbeek, F.J., Cudahy, T., Hale, M., Van der Meer, F.D., 2005. Tracing fluid pathways in fossil hydrothermal systems with near-infrared spectroscopy. *Geology* 33 (7), 597–600. <https://doi.org/10.1130/G21375.1>.
- van Ruitenbeek, F.J.A., van der Werff, H.M.A., Bakker, W.H., van der Meer, F.D., Hein, K.A.A., 2019. Measuring rock microstructure in hyperspectral mineral maps. *Remote Sensing Environ.* 220, 94–109. <https://doi.org/10.1016/j.rse.2018.10.030>.
- Velde, B., 1965. Experimental determination of muscovite polymorph stabilities. *Am. Mineral.* 50, 436–449.
- Vidal, O., Baldeyrou, A., Dubac, B., DeAndrade, V., Jullien, M., Lanson, B., 2007. Thermodynamics of phyllosilicates and low temperature thermometry. *Seminarios de la SEM* 3, 79–84.
- Waechter, N.B., Lozo, F.E.J., Barnes, V.E., 1977. *Geologic atlas of Texas Del Rio sheet*. Bureau of Economic Geology, University of Texas at Austin.
- Wang, R., Cudahy, T., Laukamp, C., Walshe, J.L., Bath, A., Mei, Y., Young, C., Roache, T.J., Jenkins, A., Roberts, M., Barker, A., Laird, J., 2017b. White mica as a hyperspectral tool in exploration for the Sunrise Dam and Kanowna Belle Gold Deposits, Western Australia. *Econ. Geol.* 112 (5), 1153–1176.
- Wang, C., Zhang, T., Pan, X., 2017. Potential of visible and near-infrared reflectance spectroscopy for the determination of rare earth elements in soil. *Geoderma* 306, 120–126. <https://doi.org/10.1016/j.geoderma.2017.07.016>.
- White, W.B., 1967. Diffuse-reflectance spectra of rare-earth oxides. *Appl. Spectros.* 21 (3), 167–171.
- Willden, R., 2006. *Goldstrike Mining District, Washington County, Utah*. In: Glyn, R.W., Park, G.M. (Eds.), *Mining Districts of Utah: Utah Geological Association Publication 32*, pp. 458–476.
- Wilson, C.E., Aydin, A., Durlofsky, L.J., Boucher, A., Brownlow, D.T., 2011. Use of outcrop observations, geostatistical analysis, and flow simulation to investigate structural controls on secondary hydrocarbon migration in the Anacacho Limestone, Uvalde, Texas. *AAPG Bull.* 95 (7), 1181–1206. <https://doi.org/10.1306/11191010069>.
- Windrim, L., Melkumyan, A., Murphy, R.J., Chlingaryan, A., Ramakrishnan, R., 2018. Pretraining for hyperspectral convolutional neural network classification. *IEEE Trans.*

- Geosci. Remote Sensing 2798–2810. <https://doi.org/10.1109/TGRS.2017.2783886>.
- Wu, T.-F., Lin, C.-J., Weng, R.C., 2004. Probability estimates for multi-class classification by pairwise coupling. *J. Mach. Learn. Res.* 5, 975–1005.
- Yang, K., Huntington, J.F., Gemmell, J.B., Scott, K.M., 2011. Variations in composition and abundance of white mica in the hydrothermal alteration system at Hellyer, Tasmania, as revealed by infrared reflectance spectroscopy. *J. Geochem. Explor.* 108 (2), 143–156. <https://doi.org/10.1016/j.gexplo.2011.01.001>.
- Yousefi, B., Sojasi, S., Ibarra Castanedo, C., Mal dague, X.P.V., Beaudoin, G., Chamberland, M., 2018. Continuum removal for ground-based LWIR hyperspectral infrared imagery applying non-negative matrix factorization. *Appl. Optics* 57 (21), 6219–6228.
- Zaini, N., van der Meer, F., van der Werff, H., 2012. Effect of grain size and mineral mixing on carbonate absorption features in the SWIR and TIR wavelength regions. *Remote Sensing* 4 (4), 987. <https://doi.org/10.3390/rs4040987>.
- Zaini, N., van der Meer, F., van der Werff, H., 2014. Determination of carbonate rock chemistry using laboratory-based hyperspectral imagery. *Remote Sensing* 6 (5), 4149. <https://doi.org/10.3390/rs6054149>.
- Zhang, M., Li, W., Du, Q., 2018. Diverse region-based CNN for hyperspectral image classification. *IEEE Trans. Image Process* 27 (6), 2623–2634. <https://doi.org/10.1109/TIP.2018.2809606>.
- Zheng, W.-J., Lei, Z.-G., Yu, C.-C., Wang, H.-Y., Fu, Y.-P., Liao, N.-F., Su, J.-H., 2014. First results of ground-based LWIR hyperspectral imaging remote gas detection. International Symposium on Optoelectronic Technology and Application. SPIE, Beijing, China.